GE

Form Approved
OMB No. 0704-0188

1. AGENCY USE ONLY (Leave blank)	2. REPORT DATE	3. REPORT TYPE AND DATES COVERED
	31 Jan 94	Final 1 May 1992 - 31 Aug 1993

4. TITLE AND SUBTITLE

Error reduction in images with the use of additional information (U)

5. FUNDING NUMBERS

35576
61102F
2304/BS

6. AUTHOR(S)

Charles L. Matson

7. PERFORMING ORGANIZATION NAME(S) AND ADDRESS(ES)

Seattle Pacific University
3307 3rd Avenue West
Seattle WA 98119

8. PERFORMING ORGANIZATION REPORT NUMBER

AFOSR-TR- 94 0256

N/A

9. SPONSORING/MONITORING AGENCY NAME(S) AND ADDRESS(ES)

AFOSR/NM
110 Duncan Ave Suite B115
Bolling AFB DC 20332-0001

10. SPONSORING/MONITORING AGENCY REPORT NUMBER

F49620-92-J-0228

11. SUPPLEMENTARY NOTES

12a. DISTRIBUTION/AVAILABILITY STATEMENT

Approved for public release;
Distribution unlimited

12b. DISTRIBUTION CODE

UL

13. ABSTRACT *(Maximum 200 words)*

The use of additional information to achieve error reduction in images is discussed in this report. Theoretical results are derived for images corrupted with Fourier domain wide-sense stationary noise. Three types of additional information are explored: support, positivity, and high-quality prior image data. The basic mechanism for reducing noise in images with these types of additional information is shown to be enforced correlations in the Fourier data. The amount of noise reduction achieved is shown to be a function of the relative correlation of the noises and the enforced correlations. For significant noise reduction to be achieved, the noises must be significantly uncorrelated relative to the enforced correlations and the sizes of the noise variances must also be significantly uncorrelated. These results are applied to computer-simulated and field data from telescopes with adaptive optics.

14. SUBJECT TERMS

support, positivity, deconvolution, convex projections

15. NUMBER OF PAGES

83

16. PRICE CODE

17. SECURITY CLASSIFICATION OF REPORT	18. SECURITY CLASSIFICATION OF THIS PAGE	19. SECURITY CLASSIFICATION OF ABSTRACT	20. LIMITATION OF ABSTRACT
unclassified	unclassified	unclassified	SAR

ERROR REDUCTION IN IMAGES WITH THE USE OF ADDITIONAL INFORMATION

FINAL TECHNICAL REPORT

AFOSR GRANT F49620-92-J-0228P00002

Charles L. Matson

Department of Electrical Engineering

Seattle Pacific University

Seattle, WA 98119

31 Jan 1994

1. Introduction

This report describes the work accomplished under the AFOSR grant F49620-92-J-0228P00002. The research being accomplished under this grant is the investigation of the usefulness of additional information for reducing noise in images. The use of information in addition to measured Fourier data to improve the resolution in reconstructed signals has received a considerable amount of attention over the last five decades[1-3]. The kinds of additional information typically used can be categorized in two ways: flexible constraints and rigid constraints. Flexible constraints are usually used to reject solutions to the deconvolution problem (i.e., regularize the deconvolution problem[4]) which are unacceptable because they include nonnegligible high frequency structure which results from noise rather than from signal. Because it is impossible to accurately reconstruct a space-limited signal which is noisy from any finite portion of its Fourier spectrum due to the infinite extent of its Fourier transform, these constraints are flexible since any reconstruction will be inaccurate (either from noise in the Fourier data or from sidelobes due to the truncation of the signal's Fourier spectrum). This flexibility allows one to trade off the structure and amplitude of noise in the reconstructed signal with the recovered resolution in the signal. Rigid constraints, on the other hand, reflect information about the signal which any reconstruction is required to possess. Thus, rigid constraints define an accurately known subset of the solution space that reconstructed signals must reside in, and flexible constraints define unacceptable regions with fuzzy boundaries within this subset.

Usually, flexible constraints are some form of smoothness constraint imposed on the reconstructed signal. These types of constraints are included in a cost function definition weighted by a Lagrange multiplier which is chosen to provide an optimum tradeoff between noise and resolution in the reconstructed signal relative to a chosen definition of optimality. It is important to note that improving resolution in this context means decreasing the point spread function width, not increasing the bandwidth of accurately known Fourier data. Using flexible constraints to decrease the point spread function width does, in fact, increase the bandwidth of the Fourier data, but without including rigid constraints (either explicitly or implicitly), the new Fourier data will be virtually all noise and will result in increased noise levels in the reconstructed signal. Empirical evidence suggests that point spread function widths can be decreased by a factor of two or more as compared to the point spread function widths corresponding to inverse Fourier transforming truncated Fourier data without imposing regularization constraints. This useful decrease in point spread function width can be attributed to the human visual system's ability to reject the random noise which accompanies decreased point spread function widths. The usefulness of flexible constraints to improve image quality was not pursued under this grant.

The other category of additional information, rigid constraints, includes information about the signal such as its region of support and the fact that the signal is positive[5,6], if appropriate. Many results can be found in the literature which show resolution improvements of a factor of two or more when support and positivity (or, equivalently, positivity) constraints are applied. However, these improvements are usually determined by reduced point spread function widths and not upon the accurate extension of measured Fourier data beyond the maximum measured bandwidth. Thus, these improvements more accurately reflect the tradeoff between noise and robustness using flexible constraints rather than actual Fourier data extrapolation. It has been shown[7] that accurate superresolution as measured by the accurate extension of measured Fourier data is negligible for objects which are at all resolved. As a result, superresolution is not part of the research focus of this project.

Another way rigid constraints can be used to improve image quality is by using them in order to reduce the noise in the measured Fourier data which results in noise reduction inside the image support in the image domain. This is a different issue than the one dealt with by using flexible constraints. With flexible constraints, the data in the Fourier domain is filtered to reduce noise in the image domain, but the signal-to-noise ratio (SNR) of the Fourier data remains unchanged at every frequency. As a result, less noise appears in the image domain, but the resolution in the image domain decreases as a result, which is the previously mentioned tradeoff between resolution and noise. With rigid constraints, on the other hand, it is possible to increase the SNR of both the Fourier domain data and the image domain data with no decrease in resolution in the image. It is this aspect of additional information that is being pursued under this grant.

The primary focus of this research effort is the derivation of theoretical expressions which predict the amount of noise reduction in the image domain as a result of using prior knowledge in addition to the measured data. The theoretical emphasis was chosen because most of the theoretical work already accomplished with regard to additional information is in support either of achieving superresolution or to determine convergence of algorithms. However, virtually no work has been accomplished in the area of theoretical predictions of SNR changes in the image domain or Fourier domain as a result of additional information. Nor has any work, to the

author's knowledge, been published which has identified the essential mechanisms by which prior knowledge causes noise reduction in images.

Because the work is theoretical, the decision of how to model the noise corrupting the image is critical. The more general the noise model, the more types of data to which the theory applies, but the greater difficulty in obtaining useful insight from the theory. The simpler the noise model is assumed to be, the more easily the theory is interpreted. The compromise chosen in this research is to model the noise in the image domain at each location x as delta-correlated noise with the possible exception of non-zero correlation with the noise at location -x. This results in Fourier domain noise which is wide-sense stationary except close to dc. This noise model accurately models both charge-coupled device (CCD) read noise and Poisson noise, which are two widely encountered noises in imagery, especially from images of space objects collected by ground-based telescopes. This noise model does exclude any noise in images which have had any sort of blurring function deconvolved out of them. The act of deconvolution can be viewed as a special type of convolution, and convolution results in correlated image domain noise. Unfortunately, the theory is quite complicated for correlated noise, and that can hinder the usefulness of the theory as a guide for how to optimally include additional information. As a result, the approach taken in this research effort is to use the results from uncorrelated noise models to guide the results for correlated noise. Quantitative results are obtained for Fourier-domain wide-sense stationary noise, and qualitative results are obtained for more general noise statistics.

The rest of this report summarizes the work accomplished under this grant. Section 2 contains the work achieved in regards to using support as a constraint, section 3 contains the work achieved with positivity as a constraint, section 4 contains the work accomplished using prior high-quality image data as a constraint, section 5 discusses the application of the theory to images collected on telescopes using adaptive optics to remove atmospheric blurring, section 6 summarizes the publications resulting from this research, and section 7 contains conclusions. Appendices A-E contain copies of papers either to be published as part of the work under this grant or to be submitted. The paper in appendix A is the result of work accomplished under an AFOSR lab task at the Phillips Laboratory just prior to the work accomplished under this grant. The research into using additional information for error reduction started with this work and thus it is included for completeness.

2. Support as a constraint

The research on using support as a constraint is complete. Appendix B contains a paper that appeared in the January 1994 issue of the Journal of the Optical Society A which contains the results from the work. The results will be summarized in this section.

The noise model used for these results is generalized delta-correlated noise as described in section 1, with one simplification. In the Fourier domain, the Fourier transform of the noise n(x), (N_r,N_i), has the following properties:

$$\langle N_r(u_1)N_r(u_2)\rangle = R_r(u_1-u_2)+R_r(u_1+u_2)$$
$$\langle N_i(u_1)N_i(u_2)\rangle = R_i(u_1-u_2)-R_i(u_1+u_2)$$
$$\langle N_i(u_1)N_r(u_2)\rangle = R_{ir}(u_1-u_2)+R_{ir}(u_1+u_2)$$

For simplicity and clarity, the terms which are a function of u_1+u_2 are neglected because their contribution is primarily around dc. This results in noise in the Fourier domain which is wide-sense stationary. In addition, the cross-correlation between the real and the imaginary terms are also neglected purely for simplicity and clarity.

Now assume that the variance of the real part of the measured Fourier data is less than or equal to the variance of the imaginary part. Because the results are completely symmetric for the case where the variance of the imaginary is less than or equal to the variance of the real part, no loss of generality occurs. In the paper, theoretical results are derived which predict the change in image domain noise variances when the following algorithm is employed: (1) inverse Fourier transform the measured Fourier data, (2) apply support constraints, (3) Fourier transform, (4) replace the real part of the support-constrained Fourier estimate with the measured data, but keep the imaginary components unchanged, (5) go back to step 1 and repeat until the noise is minimized inside the support constraint. The primary reason this algorithm was chosen is that it allows an iteration by iteration analysis of the variances in the support-constrained image and Fourier data. A summary of the theoretical results, confirmed by computer simulation, is as follows:

(a) As long as the real part of the measured Fourier data is not completely noise-free, minimum noise is achieved inside the support constraint in the image domain after only a finite number of iterations. Beyond this, the noise increases.

(b) The noise in the symmetric part of the support constraint is unaffected by the application of support constraints. Only the noise in the asymmetric part is affected. Thus asymmetric support constraints are the only type which can achieve noise reduction inside the support constraint.

(c) If $R_r=R_i$, no noise reduction is possible inside the support constraint. This case is particularly important because this is true for both CCD read noise and Poisson noise.

(d) R_r must be less than 60% of R_i for noise reduction to be possible inside the support constraint. This result is independent of the noise-free object.

The proposed algorithm was compared with a standard convex projections algorithm, where the Fourier domain convex set was defined as the region in the Fourier domain where the support-constrained Fourier data stayed within $\pm 1\sigma$ of the measured data. The results were as follows:

(a) The convex projections algorithm always resulted in increased noise inside the symmetric part of the support constraint, while the proposed algorithm did not affect the noise in this region.

(b) In the asymmetric part of the support, the proposed algorithm had comparable or better performance than the convex projections algorithm if both algorithms were stopped at the point of minimum noise.

(c) The point of minimum noise when using the convex projections algorithm was at the same point as for the proposed algorithm. Beyond this, the noise inside the support constraint increased. It appears that there is a fundamental property being demonstrated here. The convex projections approach assumes that the correct convex sets can be generated. Then the best image reconstruction must reside in the intersection of these convex sets. However, it appears that with noisy data the convex set generated to constrain the region that the support-constrained Fourier data can reside in does not intersect the convex set generated by the support constraint, in general. It should be possible to generate a convex set from the measured Fourier data large enough to have an intersection with the support constraint convex set, but there will be little or no image domain noise improvement in this case because the Fourier domain convex set is so large. In spending more time looking into the literature, it turns out that the vast majority of convex projection papers assume noise-free data, or at least that the convex sets can be generated accurately. It is especially misleading because the convex projections algorithm <u>does</u> converge when noisy data is used to generate the Fourier domain convex set - just not to the point of minimum noise! To test things, I reran the convex projections algorithm with the Fourier domain convex set generated with both the correct mean and variance. I started the algorithm with the measured Fourier data, and then the convergence point of the algorithm was the point of minimum noise. Thus it appears that algorithm performance is not a problem, but rather noisy data inherently makes it impossible to generate consistent Fourier domain convex sets which, when of reasonable size, intersect the convex set generated from the support constraint.

<u>3. Positivity as a constraint</u>

The theoretical results which predict the usefulness of positivity as a constraint have been completed, and verification of these results via computer simulation has been accomplished. The same noise model as in Section 2 was used, with some modification as discussed below. The theoretical results assume that the algorithm of section 2 is used, where the support constraint is replaced by the positivity constraint (that is, all negative values in the image are zeroed out at each iteration). A list of the results obtained is as follows:

(a) Positivity behaves as a signal-dependent support constraint. Because of this, more assumptions are needed in regard to the noise properties in order for reasonably uncomplicated theoretical results to be derived. Thus, the noise is as discussed in the introduction with the addition of the requirement that the noise $n(x)$ be gaussian for every x. This allows the joint probability density functions to be generated that are necessary to theoretically predict the behavior of the noise from iteration to iteration.

(b) As for support, noise reduction in the image domain is only possible in the asymmetric part of the positivity-induced support constraint. No noise reduction occurs in the symmetric part of the positivity-induced support constraint.

(c) The main difference between the results using positivity versus using support as a constraint is that the positivity-induced support constraint changes size on each iteration, in general.

(d) Although the results are not completely symmetric, similar noise reduction is possible for either the real part of the measured Fourier data more noisy than the imaginary, or vice versa.

(e) The ability to reduce noise inside the object support via the positivity constraint is a function not only of the noise properties but also of the magnitude of the noise-free object. This again is a reflection of the fact that the constraint is signal-dependent, while support is not.

(f) The noise outside the support constraint is reduced but not eliminated.

(g) The image data SNR must be approximately 1 or less for both positivity and support, used together as constraints, to produce a noticeable difference from just using support as a constraint.

A draft of a paper which contains the details of the positivity results is in Appendix C.

4. Prior high-quality image data as a constraint

Recently, it has been proposed[8] that perfect knowledge of part of an image could be used to decrease noise in the measured image outside of this region of perfect knowledge. This partial perfect knowledge could be obtained by either prior high-quality image data or by computer modeling of the object. This constraint was investigated during the grant and these results were generalized to allow the prior knowledge to be noisy as long as the noise is much less than the noise in the measured data. It was shown that prior high-quality partial knowledge behaves effectively as a support constraint. As a result, all the conclusions from the support part of this research apply in determining the effectiveness of using prior high-quality image data as a constraint. In particular, for wide-sense stationary Fourier domain noise, the differences in the variances of the real and imaginary parts of the measured data must differ by more than 60% for noise reduction to occur, and the noise reduction occurs only in the asymmetric part of the support constraint.

A draft of the paper which contains the details of these results is in Appendix D.

5. Support constraints applied to imagery collected using adaptive optics

Work has been completed in applying these theoretical results to telescope imagery which have used adaptive optics (AO) to help compensate for the atmosphere[9-12]. The noise statistics have been derived for both the low and high light levels. In the low light level regime, the noise is due to photon noise and CCD read noise. As mentioned in section 2, no noise reduction is expected using support as a constraint in this case since these two types of noises result in effectively wide-sense stationary Fourier domain noise with the variances of the real and imaginary parts of the noise equal. In the high light level regime, the noise is due to imperfect atmospheric compensation, assuming that the CCD read noise is negligible in this case. The noises in this case are not wide-sense stationary, so the previously derived theory cannot be quantitatively applied. However, it can be used to make qualitative judgments on the effectiveness of support constraints for noise reduction. The mechanism by which support results in noise reduction inside the support constraint is through increasing some of the variances of the iterated Fourier data beyond that of the measured Fourier data. For wide-sense stationary noise, this only results in noise reduction in the asymmetric part of the image because variance increases occur only because of the coupling of the real and the imaginary parts of the Fourier data by the asymmetric part of the support constraint. No variance increases occurred because of correlating measured real data with itself or measured imaginary data with itself. However, for non-stationary noise, variance increases are possible by both correlating real (imaginary) data with real (imaginary) data as well as coupling real and imaginary data together. In this case, it is necessary to determine not only the "size differences" of the variances of the data, but also the correlation of the noises.

A standard approach to improving image quality is to deconvolve out the blurring function caused by the telescope/AO and reblur the image with a point spread function which has more resolution associated with it. In this case, even in the low-light regime the noises become non-stationary, so exact theoretical predictions of error reduction become very difficult. However, qualitative results can be predicted from the wide-sense stationary case. As for the high-light level case, the key is the correlation of the sizes of the variances of the data and the correlation of the noises.

In Appendix E, the details of the analysis for AO data is presented. It is shown that, for reasonably resolved images, the noises corrupting the Fourier data are highly-correlated in the high-light level case, and thus little or no noise reduction is possible. In the high-light level case, the variances of the real and imaginary parts of the Fourier domain noise vary quite significantly, so more noise reduction occurs than for low-light level images.

However, because the noises are so highly correlated, variance reductions in the support of the image still only averaged 10%. In the low-light level case, the variances of the real and imaginary parts of the Fourier domain noise are virtually identical, so very little noise reduction is expected to occur even though the noises can be highly uncorrelated.

An important result of this work is that involving the structure of the noise in the reconstructed images. It was shown that, if the iterated Fourier data near the edge of the measured data region is not strongly constrained to match the measured data, the correlation effect of support constraints correlates in the zeros outside the measured data region and significantly distorts the iterated data. This distortion does not just result in noise increases in the image domain, it can result in obvious artifacts in the reconstructed images. As shown with computer simulations and with field data, when support constraints were enforced using a cost function approach instead of a convex projections approach, these image domain artifacts showed up as decreased energy in the dim parts of objects and a concentration of energy into small regions. This is especially important because it is exactly this sort of behavior which leads people to claim that superresolution is occurring! For star fields, one expects bright points on dark backgrounds, and this is exactly how this artifact can manifest itself. However, computer simulations were run using extended objects, and thus this energy concentration effect is obviously demonstrated to be algorithmic artifacts rather than improved resolution. It appears likely that this sort of artifact can show up more consistently when excessive amounts of superresolution are attempted.

This work is being accomplished in collaboration with Captain Mike Roggemann, who is an assistant professor of physics at the Air Force Institute of Technology, Wright-Patterson AFB, OH 45433. In addition, this work (along with all the work being accomplished with this grant) is being accomplished with the end purpose of it being applied to data collection methods being developed by people in the Advanced Imaging Division, Phillips Laboratory, Kirtland AFB, NM. The point of contact there is Richard Carreras, PL/LIMI, Kirtland AFB, NM 87117-6008.

6. Chronological list of publications and conference papers

C.L. Matson and M.C. Roggemann, "Noise reduction in adaptive optics imagery with the use of support constraints," to be submitted to Applied Optics and to be presented at the SPIE conference on advanced telescopes, March 1994

C.L. Matson, "Error reduction in images using high-quality prior knowledge," to be submitted to Opt.Eng. and to be submitted to SPIE conference on image processing, July 1994

C.L. Matson, "Positivity and its role in error reduction in images," to be submitted to J.Opt.Soc.Am.A. and to be submitted to a conference on inverse problems

C.L. Matson, "Variance reduction in Fourier spectra with the use of support constraints," to appear in the J.Opt.Soc.Am.A, January 1994

C.L. Matson, "Fourier spectrum extrapolation and enhancement using support constraint," to appear in the IEEE Trans. Signal Proc., January 1994

C.L. Matson, "Variance reduction in Fourier spectra and their corresponding images via support constraints," Proc. SPIE, vol.2029, July 1993

C.L. Matson, "Fourier spectrum extrapolation and enhancement using support constraint," Proc. SPIE, vol.1767, July 1992

7. Conclusions

The results of the research under this grant have been theoretical predictions of the usefulness of three types of prior information (support, positivity, and high-quality prior image data) for noise reduction inside the support of an object. Because previous work showed that superresolution has a negligible effect on image quality for images which are at all resolved[7], the focus of this work has been on noise reduction in the measured Fourier data. It has been shown that the fundamental way these types of prior knowledge work to reduce noise in images is by correlating adjacent Fourier spectra elements. As a result, the noise corrupting the measured Fourier data has to satisfy two qualitative properties for significant noise reduction to occur: (1) the correlation width of the noises must be much less than the correlation imposed by the prior knowledge, and (2) the sizes of the noise variances inside the imposed correlation region must be quite dissimilar. For symmetric support constraints, the correlations only occur between adjacent real or adjacent imaginary components of the Fourier spectrum. For asymmetric support constraints, correlations are also induced between the real and imaginary parts of a Fourier spectrum element, as well.

Quantitative theory was derived for wide-sense stationary Fourier domain noises using an algorithm which allowed a linear analysis to be accomplished. In this case, the magnitude of the real and imaginary variances are independent of frequency, so the only mechanism for noise reduction is the dissimilarity of the magnitude of the real and imaginary variances. As a result, noise reduction only occurs in the asymmetric part of the enforced support constraint produced by using positivity, true support, or prior high-quality image data as constraints.

This theory was used as a quali ative guide for non-stationary Fourier domain noises for images collected on telescopes with adaptive optics for removing atmospheric distortion. Support was used as a constraint. In the low-light level case, with the telescope blur function deconvolved out of the images, it was predicted qualitatively and shown via computer simulations and field data that essentially no noise reduction occurs because of correlation of the sizes of the noise variances in the Fourier domain, even though the noises can be quite uncorrelated. In the high-light level case, the magnitudes of the real and imaginary noise variances were shown to be quite dissimila:, on average, but the noises were so highly correlated relative to the correlation width imposed by support constraints that again little noise reduction occurred, although more occurred than in the low-light level case.

Many other types of prior knowledge can be used in addition to the ones looked at in this research[3]. However, support and positivity are the most widely used and undoubtedly the most widely recognized as the most general and powerful constraints. Because of the work accomplished under this grant, it is expected that essentially all prior knowledge will function to produce correlations between Fourier spectrum elements as the mechanism for noise reduction in images. As a result, the results presented above should generalize in a straightforward way to other types of prior knowledge.

The most important result to come out of this work is that it is the Fourier domain noise properties which dictate the effectiveness of prior knowledge to improve the quality of images. As a result, in a qualitative sense, one should be able to predict a priori whether or not prior knowledge will result in significant noise reduction in images merely by determining the noise properties. This can be accomplished easily via computer simulations, especially if the noises are too complicated for their properties to be derived analytically, as for adaptive optics noises.

References:

1. G. Demoment, "Image reconstruction and restoration: overview of common estimation structures and problems," IEEE Trans.Acoust., Speech, Signal Processing, vol.37, pp.2024-2036 (1989)
2. M.I. Sezan and A.M. Tekalp, "Survey of recent developments in digital image restoration," Opt.Eng., vol.29, pp.393-404 (1990)
3. H. Stark, editor, Image Recovery: Theory and Application, Academic Press, Orlando, FL (1987)
4. I.J.D. Craig and J.C. Brown, Inverse Problems in Astronomy, Adam Hilger Ltd, Bristol (1986)
5. C.K. Rushforth and R.L. Frost, "Comparison of some algorithms for reconstructing space-limited images," J.Opt.Soc.Am, vol.70, pp.1539-1544 (1980)
6. R.W. Schafer, et.al., "Constrained iterative restoration algorithms," Proc.IEEE, vol.69, pp.432-450 (1981)
7. C.L. Matson, "Fourier spectrum extrapolation and enhancement using support constraints," to appear in the IEEE Trans.Signal Processing, January 1994
8. R.A. Carreras, "Image restoration using nonlinear optimization techniques with a knowledge-based constraint," Proc.SPIE, vol.2029, pp.209-226 (1993)
9. M.C. Roggemann, "Optical performance of fully and partially compensated adaptive optics systems using least-squares and minimum variance phase reconstructors," Computers Elect. Engng, vol.18, pp. 451-466 (1992)
10. M.C. Roggemann, "Limited degree-of-freedom adaptive optics and image reconstruction," Applied Optics, vol.30, pp.4227-4233 (1991)
11. M.C. Roggemann and C.L. Matson, "Power spectrum and Fourier phase spectrum estimation by using fully and partially compensating adaptive optics and bispectrum postprocessing," J.Opt.Soc.Am.A, vol.9, pp.1525-1535 (1992)
12. M.C. Roggemann, D.W. Tyler, and M.F. Bilmont, "Linear reconstruction of compensated images: theory and experimental results," Applied Optics, vol.31, pp.7429-7441 (1992)

APPENDIX A

Fourier spectrum extrapolation and enhancement using support constraints

Charles L. Matson

Department of Electrical Engineering
Seattle Pacific University
Seattle, WA 98119
(206) 281-3643

Abstract

The use of support constraints for improving the quality of Fourier spectra estimates is discussed in this paper. It is shown that superresolution is an additive phenomena which is a function of the correlation scale induced by the support constraint and is independent of the bandwidth of the measured Fourier spectrum. It is also shown for power spectra that support constraints, due to the enforced correlation of power spectra, reduce the variance of measured power spectra. These theoretical results are validated via computer simulation in the area of speckle interferometry, with very good agreement shown between theory and simulation.

1. Introduction

The use of information in addition to measured Fourier data to improve the resolution in reconstructed signals has received a considerable amount of attention over the last five decades[1,2,3]. The kinds of additional information typically used can be categorized in two ways: flexible constraints and rigid constraints. Flexible constraints are usually used to reject solutions to the deconvolution problem (i.e., regularize the deconvolution problem[4]) which are unacceptable because they include nonnegligible high frequency structure which results from noise rather than from signal. Because it is impossible to accurately reconstruct a space-limited signal which is noisy from any finite portion of its Fourier spectrum due to the infinite extent of its Fourier transform, these constraints are flexible since any reconstruction will be inaccurate (either from noise in the Fourier data or from sidelobes due to the truncation of the signal's Fourier spectrum). This flexibility allows one to trade off the structure and amplitude of noise in the reconstructed signal with the recovered resolution in the signal. Rigid constraints, on the other hand, reflect information about the signal which any reconstruction is required to possess. Thus, rigid constraints define an accurately known subset of the solution space that reconstructed signals must reside in, and flexible constraints define unacceptable regions with fuzzy boundaries within this subset.

Usually, flexible constraints are some form of smoothness constraint imposed on the reconstructed signal. These types of constraints are included in a cost function definition weighted by a Lagrange multiplier which is chosen to provide an optimum tradeoff between noise and resolution in the reconstructed signal relative to a chosen definition of optimality. It is important to note that improving resolution in this context means decreasing the point spread function width, not increasing the bandwidth of accurately known Fourier data. Using flexible constraints to decrease the point spread function width does, in fact, increase the bandwidth of the Fourier data, but without including rigid constraints (either explicitly or implicitly), the new Fourier data will be virtually all noise and will result in increased noise levels in the reconstructed signal. Empirical evidence suggests that point spread function widths can be decreased by a factor of two or more as compared to the point spread function widths corresponding to inverse Fourier transforming truncated Fourier data without imposing regularization constraints. This useful decrease in point spread function width can be attributed to the human visual system's ability to reject the random noise which accompanies decreased point spread function widths.

The other category of additional information, rigid constraints, includes information about the signal such as its region of support and the fact that the signal is nonnegative[5,6], if appropriate. Many results can be found in the literature which show resolution improvements of a factor of two or more when support and nonnegativity constraints are applied. However, these improvements are usually determined by reduced point spread function widths and not upon the accurate extension of measured Fourier data beyond the maximum measured bandwidth. Thus, these improvements more accurately reflect the tradeoff between noise and robustness using flexible constraints rather than actual Fourier data extrapolation. Furthermore, algorithm results from which these claims are derived usually come from testing the algorithms with finite sums of point sources. As will be shown, superresolution can be achieved quite easily using support constraints with point sources because of the small space-bandwidth product that results from typical point source support constraints. Another result that will be shown is that superresolution using support constraints is additive; that is, a finite (small) amount of Fourier spectrum superresolution can be accomplished using support constraints, and this superresolution is independent of the bandwidth of the measured Fourier data if the support constraint is based upon the size of the object. Thus, achievable superresolution as measured by accurate extension of measured Fourier spectra is merely a small fraction of the bandwidth of measured Fourier spectra for images which are at all resolved, rather than being a multiplicative phenomena which is a function of the measurement bandwidth.

Another way that support constraints can be used to improve measured Fourier spectra is by decreasing the variance of the measurements through enforcing correlations among the Fourier data. Typically, Fourier spectra are measured pointwise without including correlation among the Fourier spectra datapoints. Applying support constraints is equivalent to enforcing Fourier domain correlations which causes interpixel averaging, and this averaging reduces the variance of the measurements. In this paper, mathematical expressions are derived which predict the degree of variance reduction as a function of the relative correlation of the noise and the support constraint correlation for power spectrum estimation. To demonstrate the validity of the expressions, computer simulation results are presented for the case of estimating the power spectra of two dimensional objects through atmospheric turbulence, and achieved variance reductions are compared to theoretical predictions. The organization of the paper is as follows: section 2 contains mathematical results which predict the achievable superresolution using support constraints, section 3 contains mathematical results predicting the variance reduction

in measured power spectrum data using support constraints, section 4 has results from the computer simulation, and conclusions can be found in section 5.

2. Superresolution

Consider the following one-dimensional model relating the true object intensity distribution o(x) and the measured image intensity distribution i(x):

$$i(x) = 2f_o \int_{-\alpha/2}^{\alpha/2} o(\xi)\,\mathrm{sinc}\{2f_o(x-\xi)\}d\xi \tag{1}$$

This model corresponds to perfect knowledge of the true object Fourier spectrum inside the frequency range $[-f_o,f_o]$ and zeroing it out everywhere else. The image is then obtained by inverse Fourier transforming this truncated spectrum and zeroing out the resulting image intensity distribution outside the known support region $[-\alpha/2,\alpha/2]$. Although this model ignores noise, the effects of noise will be discussed shortly.

The true object intensity distribution o(x) can be recovered exactly from Eq.(1) for noise free data since the operation shown in Eq.(1) is invertible (although the inverse in not continuous). A convenient conceptual approach to accomplishing the inversion is by decomposing both i(x) and o(x) into infinite sums of prolate spheroidal wave functions[7]. Let $\psi_{\alpha n}(x)$ be the n^{th} prolate spheroidal wave function (defined on $[-\alpha/2,\alpha/2]$) corresponding to the space-bandwidth product $2\alpha f_o$ and let $\psi_n(x)$ be the extension of $\psi_{\alpha n}(x)$ to the interval $(-\infty,\infty)$. Then, because i(x) is bandlimited, it can be expressed as

$$i(x) = \sum_{n=0}^{\infty} c_n \psi_n(x) \tag{2}$$

where each coefficient c_n is the projection of i(x) onto $\psi_n(x)$ and is given by

$$c_n = \int_{-\infty}^{\infty} i(\xi)\psi_n(\xi)d\xi \tag{3}$$

In the same way, because o(x) has finite support, it can be expressed as

$$o(x) = \sum_{n=0}^{\infty} d_n \psi_{\alpha n}(x) \tag{4}$$

and the expansion coefficients d_n are given by

$$d_n = \frac{1}{\lambda_n} \int_{-\alpha/2}^{\alpha/2} o(\xi)\psi_{\alpha n}(\xi)d\xi \tag{5}$$

where the λ_n are the eigenvalues of the operator given by Eq.(1), and thus $1/\lambda_n$ are the eigenvalues of the inverse operator. Using these decompositions, it can be shown that[5] o(x) is given by

$$o(x) = \sum_{n=0}^{\infty} \frac{c_n}{\lambda_n} \psi_{\alpha n}(x) \tag{6}$$

The inverse of the operator described by Eq.(1) exists because all of its eigenvalues are greater than zero, but the inverse is not continuous because the limit point of the eigenvalues is zero. As a result, if any noise exists at all, the infinite limit in Eq.(6) must be replaced by some finite number N, where N is determined by the signal-to-noise ratio (SNR) of the measured data. Therefore, o(x) can be approximated by[5]

$$o(x) \approx \sum_{n=0}^{N} \frac{c_n}{\lambda_n} \psi_{\alpha n}(x) \tag{7}$$

Although Eq.(7) avoids noise amplification by truncating the series shown in Eq.(6), other approaches can be taken[5] which attenuate the effect of the decreasing eigenvalues instead of truncating the series.

The key to understanding achievable superresolution is understanding the dependence of the magnitude of the eigenvalues λ_n upon f_0 and α. It has been shown[8] that the eigenvalues are bounded above by one for all n and are greater than approximately 0.1 for $n \leq 2\alpha f_0$. Beyond this value of n, the eigenvalues fall off quickly at a fairly constant rate such that λ_n/λ_{n+1} is approximately equal to ten. Therefore, assuming a moderate SNR, the maximum size that N in Eq.(7) can be without magnifying the noise excessively is $2\alpha f_0$. It has been shown[9,10] that the n^{th} prolate spheroidal wave function results in an image domain resolution comparable to a sine function of frequency $(n+1)/2\alpha$ in terms of the average distance between zero crossings. As a result, the spatial frequency f_m that corresponds to $N=2\alpha f_0$ is given by

$$\begin{aligned} f_m &= (2\alpha f_o + 1)/2\alpha \\ &= f_o + 1/2\alpha \end{aligned} \tag{8}$$

Recall that f_0 is the maximum spatial frequency at which measured Fourier data exists. Therefore, the use of support constraints results in superresolution of this measured data by an additive amount of $1/2\alpha$. The additional amount is 25% of the main lobe of the sinc function which is the Fourier transform of the support constraint, and the superresolution term is independent of f_0. Thus, superresolution via support constraint enhancement is additive and is negligible for images which are at all resolved as will be shown. This result is reasonably independent of the SNR of the measured data. Because the eigenvalues drop off so rapidly, a factor of ten increase in SNR is required to increase N by one. Even if it is possible to increase the SNR by several orders of magnitude, the result is still an additive superresolution increase, not a multiplicative one.

Consider now using support constraints on a point source. Because the support of a point source is zero, by definition, support constraints are usually derived from the point spread function corresponding to the bandwidth of the measured Fourier data. In particular, a reasonable support constraint is obtained by setting the support width equal to the width of the main lobe of the point spread function. For the case of using a filter which is one inside $[-f_o, f_o]$ and zero elsewhere, the point spread function main lobe width is given by $1/f_0$, and thus $\alpha = 1/f_0$. Substituting this expression into Eq.(8) results in

$$\begin{aligned} f_m &= f_o + 1/(2/f_o) \\ &= f_o + f_o/2 \end{aligned} \tag{9}$$

Now the achievable superresolution is a function of the bandwidth of the measured Fourier data because the support constraints were based upon the bandwidth of the Fourier data, and results in a 50% increase in bandwidth regardless of f_0. Since most algorithms include regularization along with support constraints, the resolution as measured by point spread function width can improve by a factor of two or more beyond this 50% improvement as well. Thus, it can be seen that support constraints applied to point source images along with regularization constraints can decrease point spread function widths in recovered imagery by a factor of two or more. However, this apparent improvement must be kept in perspective. By choosing $\alpha = 1/f_0$, the space bandwidth product equals two independent of f_0, and thus N in Eq.(7) is always equal to two. Therefore, the only reason the increase in resolution appears large because it is being compared to such a small amount of measured spatial frequency information in terms of the space bandwidth product.

The point source case can be extended to analyze the effect support constraints have upon resolved objects. Let the resolved object be X point sources separated from each other by the Rayleigh resolution distance. This is equivalent to saying that there are X resolution cells in the image. Then $\alpha=(X+1)/(2f_o)$, where the support region is defined as the distance between the first zeros of the point spread function on either end of the resolved object. Substituting this into Eq.(8) gives

$$\begin{aligned} f_m &= f_o + \frac{1}{2[(X+1)/2f_o]} \\ &= f_o + \frac{f_o}{X+1} \end{aligned} \tag{10}$$

It can be seen that the superresolution term decreases as the support increases. For example, if there were 9 resolution cells in the image, the amount of superresolution would be 10%. If there were 99 resolution cells in the image, the amount of superresolution would be only 1%. This shows that superresolution is negligible for objects which are at all resolved.

An extensive analytic and computer simulation study was recently accomplished[11] to explore the usefulness of support constraints to both fill in holes in a modulation transfer function (MTF) as well as to extrapolate Fourier data beyond the maximum measured Fourier data. Least squares and minimum variance estimators were evaluated as well as a CLEAN algorithm in conjunction with support constraints. The object to be imaged in the study was assumed to be windowed white noise with variance σ_x^2, and white noise was added to imaged object with variance σ_n^2. The data were assumed to have a SNR of over 300, where the SNR was defined as σ_x^2/σ_n^2, which is sufficiently high to allow $N=2\alpha f_o+1$ in Eq.(7) instead of the previously assumed $N=2\alpha f_o$. As a result, the superresolution term in Eq.(8) becomes $1/\alpha$ instead of $1/2\alpha$. In the study, a wide variety of support constraints were used, and the error at each spatial frequency between the true object spectrum and the recovered object spectrum was calculated for each support constraint. The results confirmed that the ability to derive Fourier information in regions where no data is available depends upon $1/\alpha$. In particular, it can be shown from the results in the study that the reduction in quality of the extrapolated Fourier data is well parameterized by $1/\alpha$, both in the holes of the MTF as well as beyond the cutoff spatial frequency of the MTF.

3. Variance Reduction

Although support constraints do not allow useful superresolution to occur for well resolved objects, they can be useful in reducing the variance of measured Fourier data. In this section, theoretical results will be derived which predict the variance reduction in measured Fourier data resulting from applying support constraints. For simplicity, the theory will be developed for power spectrum estimation.

Let i(x) and I(u) be Fourier transform pairs, where x and u are n-dimensional spatial and spatial frequency vectors, respectively, and i(x) is real. Also, let the autocorrelation support constraint be given by w(x). Then, by definition, it follows that

$$i(x)*i(x) = w(x)[i(x)*i(x)] \tag{11}$$

where * denotes autocorrelation. Fourier transforming both sides of Eq.(11) results in

$$|I(u)|^2 = \int_{-\infty}^{\infty} W(\xi)|I(u-\xi)|^2 d\xi \tag{12}$$

where W(u) is the Fourier transform of w(x). It can be seen from Eq.(12) that the power spectrum of i(x) at any spatial frequency point u is related to the power spectrum at every other spatial frequency point via the convolution operation. In essence, Eq.(12) shows that applying support constraints results in weighted interpixel averaging with the weights given by the Fourier transform of the window function. Let $|I_e(u)|^2$ be the pointwise estimated

power spectrum, and let $|I_S(u)|^2$ be the improved power spectrum estimate which results from applying support constraints to $|I_e(u)|^2$. Then, at each spatial frequency u, it follows from Eq.(12) that

$$|I_s(u)|^2 = \int_{-\infty}^{\infty} W(\xi)|I_e(u-\xi)|^2 d\xi \tag{13}$$

The variance of $|I_S(u)|^2$, $\mathrm{var}(|I_S(u)|^2)$, is given by

$$\mathrm{var}(|I_s(u)|^2) = <(|I_s(u)|^2)^2> - <|I_s(u)|^2>^2$$

$$= <\int_{-\infty}^{\infty} W(\xi)|I_e(u-\xi)|^2 d\xi \int_{-\infty}^{\infty} W(\zeta)|I_e(u-\zeta)|^2 d\zeta> - <\int_{-\infty}^{\infty} W(\xi)|I_e(u-\xi)|^2 d\xi><\int_{-\infty}^{\infty} W(\zeta)|I_e(u-\zeta)|^2 d\zeta>$$

$$= \int_{-\infty}^{\infty}\int W(\xi)W(\zeta)[<|I_e(u-\xi)|^2|I_e(u-\zeta)|^2> - <|I_e(u-\xi)|^2><|I_e(u-\zeta)|^2>]d\xi d\zeta \tag{14}$$

where the angle brackets denote expectation. Furthermore, assume that $|I_e(u)|^2$ is well modeled by

$$|I_e(u)|^2 = |O(u)|^2 + n(u) \tag{15}$$

where $|O(u)|^2$ is the true object power spectrum and n(u) is zero mean wide sense stationary noise with variance equal to σ^2, and thus it follows that $\mathrm{var}\{|I_e(u)|^2\} = \sigma^2$. Substituting Eq.(15) into Eq.(14) gives

$$\mathrm{var}(|I_s(u)|^2) = \sigma^2 \int_{-\infty}^{\infty}\int W(\xi)W(\zeta)\frac{R_n(\xi-\zeta)}{\sigma^2}d\xi d\zeta \tag{16}$$

where $R_n(\xi-\zeta) = <n(u-\xi)n(u-\zeta)>$ and $R_n(0) = \sigma^2$. It can be seen that $\mathrm{var}\{|I_S(u)|^2\}$ is equal to $\mathrm{var}\{|I_e(u)|^2\}$ multiplied by an integral factor which determines the amount of reduction in variance caused by the application of support constraints.

Two asymptotic cases will be analyzed to help gain an understanding of what Eq.(16) means in terms of variance reduction. Consider first the case where the noise autocorrelation function is much broader than the Fourier transform of the support function. This is equivalent to assuming that $R_n(\xi-\zeta) \approx \sigma^2$ for all values of ζ and ξ for which the functions $W(\xi)$ and $W(\zeta)$ are significantly nonzero. In this case, Eq.(16) can be approximated by

$$\mathrm{var}(|I_s(u)|^2) \approx \sigma^2 \int_{-\infty}^{\infty}\int W(\zeta)W(\xi)d\xi d\zeta$$
$$= \sigma^2 \tag{17}$$

Thus, there is essentially no variance reduction from applying support constraints if the noise correlation is much broader than the Fourier transform of the support constraints.

Now consider the other asymptotic case where the noise autocorrelation function is much narrower than the Fourier transform of the support function. This case is more easily analyzed by using a change of variables in Eq.(16), which results in

$$\mathrm{var}(|I_s(u)|^2) = \sigma^2 \int_{-\infty}^{\infty}\int W(\xi+\frac{\zeta}{2})W(\xi-\frac{\zeta}{2})\frac{R_n(\zeta)}{\sigma^2}d\xi d\zeta \tag{18}$$

Because $R_n(\zeta)$ is much narrower than either $W(\cdot)$ term, the ζ dependence of the $W(\cdot)$ terms can be neglected. This gives

$$\begin{aligned}\mathrm{var}(|I_s(u)|^2) &\approx \sigma^2 \int_{-\infty}^{\infty}\int W(\xi)W(\xi)\frac{R_n(\zeta)}{\sigma^2}d\xi d\zeta \\ &= \sigma^2 \int_{-\infty}^{\infty} W(\xi)^2 d\xi \int_{-\infty}^{\infty}\frac{R_n(\zeta)}{\sigma^2}d\zeta\end{aligned} \tag{19}$$

The second integral term in Eq.(19) is independent of the support constraint size, while the first term, by Parseval's theorem, is the area of the support. This shows that $\mathrm{var}\{|I_s(u)|^2\}$ decreases as the support area decreases, and eventually asymptotes to zero as the support area goes to zero. Thus, the amount of variance reduction depends both upon the support constraint area and the relative correlation of the noise corrupting the measured Fourier data and the correlation imposed by the support constraints.

An area of research in which support constraints are used quite often is the area of speckle interferometry[12]. Therefore, the theoretical results developed in this section will be analyzed for the specific case of estimating the power spectrum of an object through atmospheric turbulence. The average power spectrum of the object multiplied by the telescope/atmosphere power spectrum transfer function, $\langle|I_e(u)|^2\rangle$, is calculated by

$$\langle|I_e(u)|^2\rangle = \frac{1}{M}\sum_{m=1}^{M}[|D_m(u)|^2 - N_m] \tag{20}$$

where M is the total number of frames of data, $D_m(u)$ is the Fourier transform of the m^{th} frame, and N_m is the number of photons in the m^{th} frame. This estimator assumes that the estimation process is shot noise limited, and thus it is only necessary to subtract N_m from each frame to obtain an unbiased estimate of the power spectrum.

Under the standard assumption of isoplanicity, it follows that $\langle|I_e(u)|^2\rangle$ is given by

$$\langle|I_e(u)|^2\rangle = |O(u)|^2\langle|\tau(u)|^2\rangle \tag{21}$$

where O(u) is the true object Fourier spectrum and $\langle|\tau(u)|^2\rangle$ is the power spectrum transfer function of the telescope/atmosphere system normalized to one at dc. An estimate of the true object power spectrum, $|O_e(u)|^2$, is obtained by dividing both sides of Eq.(21) by $\langle|\tau(u)|^2\rangle$, which yields

$$\langle|O_e(u)|^2\rangle = \frac{\langle|I_e(u)|^2\rangle}{\langle|\tau(u)|^2\rangle} \tag{22}$$

When the estimation process is shot noise limited, in the low light level regime, and for spatial frequencies sufficiently large that effects of the "seeing spike" are negligible, it has been shown[13] that the autocovariance of $\langle|I_e(u)|^2\rangle$ is given by

$$\langle|I_e(\xi)|^2|I_e(\zeta)|^2\rangle - \langle|I_e(\xi)|^2\rangle\langle|I_e(\zeta)|^2\rangle = |O(\xi-\zeta)|^2\langle|\tau(\xi-\zeta)|^2\rangle \tag{23}$$

Notice that the power spectrum noise correlation depends only upon the difference of ξ and ζ and is a function of the true object power spectrum and the telescope/atmosphere power spectrum transfer function. Although $\langle|\tau(u)|^2\rangle$ is most accurately calculated by solving a four-dimensional integral equation, a reasonably accurate simplification is given by[14]

$$\langle|\tau(u)|^2\rangle = [A^{\frac{1}{2}} + \frac{A^{\frac{1}{2}}B^{\frac{1}{2}}}{4} + B^{\frac{1}{2}}]^2 \tag{24}$$

The coefficients A and B are given by

$$\begin{aligned} A &= T_D^2(u)\exp\{-q(\frac{\lambda u}{r_o})^{\frac{5}{3}}\} \\ B &= 0.4355(\frac{r_o}{D})^2 T_D(u)[1+1.38(\frac{r_o}{\lambda u})^{0.48}]\exp\{-[2.5(\frac{\lambda u}{r_o})^2]^{-1}\} \end{aligned} \tag{25}$$

where r_0 is the Fried parameter which provides a measure of the correlation scale of the atmosphere, $T_D(u)$ is the diffraction limited incoherent telescope transfer function, D is the telescope diameter, λ is the observational wavelength, and q is a function of D/r_0 and can be approximated by

$$q \approx \frac{1}{0.17514 - 0.000078(\frac{D}{r_o})} \tag{26}$$

for $30 < D/r_0 < 170$. As D/r_0 approaches infinity, Eq.(24) does not hold and q approaches the more well known constant 6.88. Also, this approximation for q becomes less accurate the smaller D/r_0 becomes[14], with an inaccuracy of approximately 10% for D/r_0=30. For typical values of r_0 (≈ 10cm at λ=550nm) and D (1m to 4m), when observing in the visible wavelengths, the dominant effect governing the correlation scale in Eq.(23) is the exponential term in factor A. Under these conditions, if the support of the true object is much smaller than the seeing disk, which is defined as λ/r_0, the resulting variance given by Eq.(14) will approach zero. If the support of the object is much bigger than the seeing disk, applying support constraints will result in very little reduction of the variance. Although the power spectrum term $|O(u)|^2$ in Eq.(23) provides some decorrelation for large objects, and thus slows down the increase in variance as the support increases, eventually $\text{var}\{|I_s(u)|^2\}$ asymptotes to $\text{var}\{|I_e(u)|^2\}$.

Because $|O_e(u)|^2$, and not $|I_e(u)|^2$, is what is estimated in speckle interferometry, it is necessary to determine the covariance of $|O_e(u)|^2$ from the covariance of $|I_e(u)|^2$. It is easy to show that

$$\langle|O_e(\xi)|^2|O_e(\zeta)|^2\rangle - \langle|O_e(\xi)|^2\rangle\langle|O_e(\zeta)|^2\rangle = \frac{|O(\xi-\zeta)|^2\langle|\tau(\xi-\zeta)|^2\rangle}{\langle|\tau(\xi)|^2\rangle\langle|\tau(\zeta)|^2\rangle} \tag{27}$$

The effect the nonstationary terms have upon the variance reduction integral can be determined by substituting Eq.(27) into Eq.(14), which gives

$$\mathrm{var}(|I_s(u)|^2) = \int_{-\infty}^{\infty}\int W(\xi)W(\zeta)\frac{|O(\xi-\zeta)|^2 \langle|\tau(\xi-\zeta)|^2\rangle}{\langle|\tau(u-\xi)|^2\rangle\langle|\tau(u-\zeta)|^2\rangle}d\xi d\zeta \qquad (28)$$

Because $\langle|\tau(u)|^2\rangle$ is a slowly varying function for the frequencies for which Eq.(23) is valid, and the numerator is a strong function of $(\xi-\zeta)$, both terms in the denominator of the integrand are essentially independent of ξ and ζ and can be brought outside of the integral, which results in

$$\mathrm{var}(|I_s(u)|^2) = \frac{1}{\langle|\tau(u)|^2\rangle^2}\int_{-\infty}^{\infty}\int W(\xi)W(\zeta)|O(\xi-\zeta)|^2\langle|\tau(\xi-\zeta)|^2\rangle d\xi d\zeta \qquad (29)$$

This equation will be used for comparing the computer simulation results in the next section to theoretical predictions.

4. Computer Simulation Results

To determine the accuracy of the theoretical predictions developed in section 3, a computer simulation program was used to generate sequences of atmosphere and shot noise corrupted images. Average power spectrums of these images were calculated using Eq.(20), and the atmosphere/telescope attenuation effects were removed from image power spectrums using Eq.(22), where estimated system power spectrum transfer functions were obtained by using an unresolved star as the true object in the computer simulation. The parameters for the unresolved star simulation run were chosen so that the estimated system power spectrum had a much higher SNR than the estimated image power spectrum, where the power spectrum SNR was calculated as the sample mean divided by the square root of the sample variance at each spatial frequency. This was done so that the variances of the estimated object power spectrum points were a function only of the image power spectrum estimate. Sample variances of the power spectrum estimates were also calculated for use in the deconvolution algorithm.

The first step taken to validate the theoretical expressions was to compare the predicted power spectrum correlation (Eqs.(23)-(26)) against both computer simulated and field data. The field data used was collected on the (unresolved) single star Zeta Delphinus using a photon counting camera from the Stanford Center for Space and Astrophysics[15] mounted on the Kitt Peak Steward Observatory 2.3m telescope. The observing wavelength was 550nm and the spectral bandpass was 30nm. There were an average of 292 photons per frame and 2500 frames were used in estimating the correlation coefficient of the power spectrum correlation. Extensive analysis[16] of the data resulted in an estimated value for r_0 of 10.5cm. As noted in section 3, the power spectrum correlation coefficient depends only upon the difference of spatial frequencies, not their actual values. As a result, the correlation coefficient curve for the estimated power spectrum of Zeta Delphinus was calculated using sample statistics for several different center spatial frequencies and the results were averaged together. The center spatial frequencies were chosen to be far enough away from dc that the assumptions used in deriving Eqs.(23)-(26) were satisfied and such that the SNRs of the power spectrum at these frequencies were above one so that the estimates of the correlation coefficients would be accurate. The resulting correlation coefficient curve is shown in Fig.1 along with the coefficient curves obtained by using the computer simulation code and by theoretical predictions. Notice that the simulation and theoretical curves differ by a small amount at all spatial frequency differences, and that the field data curve matches the simulation curve at small differences and the theory curve at larger differences. Thus it can be seen that the field and simulation results match theoretical predictions quite well. However, since theoretical predictions will be compared to simulation results, it is necessary to refine the parameters in the theoretical expressions to provide a closer fit between simulation and theory. To this end, the q parameter was chosen not on the basis of Eq.(26), but so that the theory curve would agree with the simulation curve. The best fit was found to occur with q=4.6 as compared to the predicted value of 5.77, and Fig.2 shows the two curves. Notice the very close match now between theory and simulation. As discussed in the previous section, Eq.(26) becomes less accurate as D/r_0 decreases with a 10% mismatch for D/r_0=30. For this simulation D/r_0=22, so the mismatch between theory and simulation was expected.

Next, an algorithm was developed to estimate the autocorrelation from its power spectrum while using support constraints. A wide variety of algorithms have been proposed that could have been used[3,4,17]; however, most of these algorithms mix the application of support constraints and regularization constraints in such a way that it is impossible to determine which constraint caused the observed changes in the power spectrum. For this reason, a simple deconvolution algorithm was devised. First, it was determined what portion of the power spectrum was estimated with a SNR greater than one. Because only circularly symmetric objects were used, this region was defined as a circle centered at dc with a radius R_{snr} dependent upon the SNR. The deconvolutions were accomplished by minimizing the following cost function:

$$\text{cost function} = \sum_{|u|\le R_{snr}} \frac{1}{F^2(u)\sigma_e^2(u)} \left[|O(u)|^2 - F(u)|O_e(u)|^2 \right]^2 + \sum_{|u|>R_{snr}} \frac{1}{F^2(u)\sigma_a^2} \left[|O(u)|^2 \right]^2 \qquad (30)$$

where $\sigma_e(u)^2$ is the sample variance of the power spectrum estimate at u, the minimization is accomplished over all power spectrums $|O(u)|^2$ whose corresponding autocorrelations are within the support given by w(x), and σ_a^2 is the average of the variances for $|u|=R_{snr}$ and serves the function of a Lagrange multiplier for the regularization term. The first summation is the data matching term, and the second summation is the regularization term. Notice that the regularization process only involves spatial frequencies at which no data matching is to occur, and thus the effect of regularization is decoupled from the effect of support constraints except for support-induced correlations near the boundary defined by R_{snr}. Therefore, by comparing the recovered power spectrum to the measured power spectrum sufficiently far inside the circle defined by R_{snr} so that support-induced correlations involving spatial frequencies u for $|u|>R_{snr}$ are negligible, the improvement by using support constraints can be calculated. In order to smooth the transition between the two summations, a filter F(u) was used to multiply the measured power spectrum, and thus the sample variances must be multiplied by $F(u)^2$. For these simulation results, the smoothing filter F(u) was defined by

$$F(u) = \frac{J_1(2\pi\beta|u|)}{\beta|u|} \qquad (31)$$

where J_1 is a Bessel function of the first kind, order one, and the scaling parameter ß was chosen so that the first zero of the filter occurred where the power spectrum SNR was approximately 0.5. This filter was chosen because the inverse Fourier transform of F(u) has finite support, and thus support constraints can be applied in a manner consistent with the cost function.

The minimization of Eq.(30) was accomplished using an IMSL conjugate gradient routine with a user supplied cost function and gradient. All the minimizations were given 300 steps. The cost functions were reduced a factor of 20 on average from beginning to end, and the norm squared of the gradient always decreased at least six orders of magnitude. The starting point for the minimization was the inverse Fourier transform of $F(u)|O_e(u)|^2$. At the end of each minimization, the support-constrained power spectrum estimate $|O_s(u)|^2$ was divided by F(u) and a sample variance at each spatial frequency was determined by calculating the mean square difference between the true and estimated power spectrums. Because the noise processes and the true object power spectra were always circularly symmetric, all the variances with the same spatial frequency magnitudes were averaged together, which resulted in sample variances as a function of |u|. The same averaging was done for the sample variances of $|O_e(u)|^2$, and the sample variances of $|O_s(u)|^2$ for each |u| were divided by the sample variances of $|O_e(u)|^2$. These variance reduction factors were then averaged together to finally obtain a single number characterizing the variance reduction that occurred as a result of applying support constraints.

For the first computer simulation comparison, an unresolved star was used for the true object. The simulation parameters were as follows: r_0=11cm, D=2.3m, M=2000, and 200 photons/frame on average. An estimated object power spectrum was calculated using Eq.(22), and then the deconvolution algorithm was used for a variety of circular support constraints with diameters ranging from $0.35\lambda/r_0$ to $4.4\lambda/r_0$. The resulting variance reduction factors can be seen in Fig.3, where a normalized variance of 1.0 indicates no variance reduction. Notice how well theory and simulation results match for values of the support diameters which were less than $2.5\lambda/r_0$. For larger support diameters, the simulation results show a slightly larger normalized variance than theoretical predictions, but the match is still quite good. One possible reason for the mismatch in this region is that the main

lobe of the Fourier transform of the support constraint is only four to six pixels wide in this region, and thus coarse sampling could be contributing to a higher variance. It can be seen that the normalized variance does go to zero as the support diameter becomes small relative to the seeing disk diameter (and thus the noise correlation), and that the normalized variance starts to asymptote to one when the support diameter is three times the seeing disk diameter. Thus it appears, as expected, that the determining factor in the usefulness of support constraints is the relative size of the noise correlation function in the Fourier domain and the main lobe of the Fourier transform of the support function.

The second computer simulation comparison was accomplished to validate the theoretical expressions for a resolved object. A case which is essentially opposite to the unresolved star case is that of an object which is a uniform intensity disk. This object has a power spectrum whose falloff near dc is very steep, unlike an unresolved star which has a constant power spectrum independent of frequency. By Eq.(23), the noise correlation should fall off faster than for an unresolved star, and thus the normalized variance should rise slower as the support size increases than for the unresolved star. However, a uniform intensity disk has zeros in its power spectrum, so a point source with 10% of the intensity of the disk was added to remove these zeros without greatly affecting the shape of the disk power spectrum near dc. This allowed the sample variance reduction calculations to proceed more smoothly. Next, a series of computer simulations were accomplished for disks with diameters ranging from $0.25\lambda/r_0$ to $2\lambda/r_0$. The deconvolution algorithm was run for each of these cases, with support constraint diameters ranging from $0.6\lambda/r_0$ to $4.4\lambda/r_0$, where the increase in support constraint diameters reflects the fact that the autocorrelation support is twice the diameter of the object, and the addition of a small guard band resulting from the convolution of the support with the inverse Fourier transform of F(u). The results can be seen in Fig.4, where again there is very good agreement between theory and simulation. Notice that, compared to the unresolved star case, the rise in the normalized variance is slower, but eventually the normalized variance approaches one as well. The theory and simulation curves don't match as well as for the unresolved star case in the region where the support diameters are less than $2.5\lambda/r_0$, although the difference is small. A probable reason for the mismatch in these cases is that the theoretical curve assumes perfect disks, while the simulation results used discretized versions, and for small normalized support diameters the discrete approximation to disks is not extremely accurate. This was not a problem for the unresolved star case because the power spectrum was one at all spatial frequencies and thus did not suffer discretization problems.

The improvement in the SNR of power spectrum estimation as a result of applying support constraints is a function of the square root of the normalized variance. For an object whose autocorrelation support is the size of the seeing disk, an SNR improvement of approximately two is achieved, which indicates that large improvements in SNR using support constraints are not realistic for objects which are reasonably large. Another interesting point is that the SNR properties of power spectrum estimation in speckle interferometry get worse as r_0 decreases, but the improvement in power spectrum SNR achieved by applying support constraints increases as r_0 decreases. Thus, the use of support constraints helps offset the effects of increased atmospheric turbulence.

5. Conclusions

It was shown that superresolution using support constraints is an additive process, with the amount of achievable superresolution equal to 25% of the main lobe width of the Fourier transform of the support function when the measured Fourier data have a moderate SNR. For objects which are at all resolved, this amount of superresolution is virtually unnoticeable. It was also shown that support constraints are useful in reducing the variance of the measured Fourier data, with the amount of variance reduction dependent upon the relative size of the noise correlation and the correlation enforced by the support constraint.

Because all superresolution approaches attempt to derive additional Fourier data from measured Fourier data, it is clear that enforced correlations are the mechanism for superresolution. As a result, all superresolution should be additive in nature, and thus it is not realistic to expect significant amounts of accurately extrapolated Fourier spectra regardless of the constraint applied.

Acknowledgments

This research was funded in part by a grant from the U.S. Air Force Office of Scientific Research, AFOSR/NM, Bolling Air Force Base, Washington, D.C., and by the U.S. Air Force Phillips Laboratory, PL/LMI, Kirtland AFB, NM. The author also wishes to thank E.K. Hege and J.S. Morgan for supplying the field data on Zeta Delphinus.

References

1. G. Demoment, "Image reconstruction and restoration: overview of common estimation structures and problems," IEEE Trans.Acoust., Speech, Signal Processing, vol.37, pp.2024-2036 (1989)
2. M.I. Sezan and A.M. Tekalp, "Survey of recent developments in digital image restoration," Opt.Eng., vol.29, pp.393-404 (1990)
3. H. Stark, editor, Image Recovery: Theory and Application, Academic Press, Orlando, FL (1987)
4. I.J.D. Craig and J.C. Brown, Inverse Problems in Astronomy, Adam Hilger Ltd, Bristol (1986)
5. C.K. Rushforth and R.L. Frost, "Comparison of some algorithms for reconstructing space-limited images," J.Opt.Soc.Am, vol.70, pp.1539-1544 (1980)
6. R.W. Schafer, et.al., "Constrained iterative restoration algorithms," Proc.IEEE, vol.69, pp.432-450 (1981)
7. D. Slepian and H.O. Pollak, "Prolate spheroidal wave functions, Fourier analysis, and uncertainty - I," Bell Syst.Tech.J., vol.40, pp.43-63 (1961)
8. D. Slepian and E. Sonnenblick, "Eigenvalues associated with prolate spheroidal wave functions of zero order," Bell Syst.Tech.J., vol.44, pp.1745-1758 (1965)
9. C.K. Rushforth and R.W. Harris, "Restoration, resolution, and noise," J.Opt.Soc.Am, vol.58, pp.539-545 (1968)
10. M. Bendinelli, et.al., "Degrees of freedom, and eigenfunctions, for the noisy image," J.Opt.Soc.Am, vol.64, pp.1498-1502 (1974)
11. D.L. Fried and D.T. Sherwood, "Final report on ONR contract No. N00014-88-C-0692: Phased array imaging," the Optical Sciences Company report no. DR-514 (1990)
12. A. Labeyrie, "Attainment of diffraction-limited resolution in large telescopes by Fourier analyzing speckle patterns in star images," Astron.Astrophys., vol.6, pp.85-87 (1970)
13. D.L. Fried, "Covariance analysis of the Knox-Thompson imaging method," the Optical Sciences Company report no. TR-1111 (1991)
14. R.K. Szeto and D.L. Fried, "Numerical evaluation of the covariance of the phase of the Knox-Thompson phasor," the Optical Sciences Company report no. TR-1125 (1991)
15. J.G. Timothy, "Multianode microchannel array detector systems: performance characteristics," Opt.Eng., vol.24, pp.1066-1071 (1985)
16. D.L. Fried and D.T. Sherwood, "Analysis of some white-light speckle data: comparison of theory and experiment," the Optical Sciences Company report no. TR-926R (1989)
17. J.L.C. Sanz and T.S. Huang, "Unified Hilbert space approach to iterative least-squares linear signal restoration," J.Opt.Soc.Am.A, vol.11, pp.1455-1465 (1983)

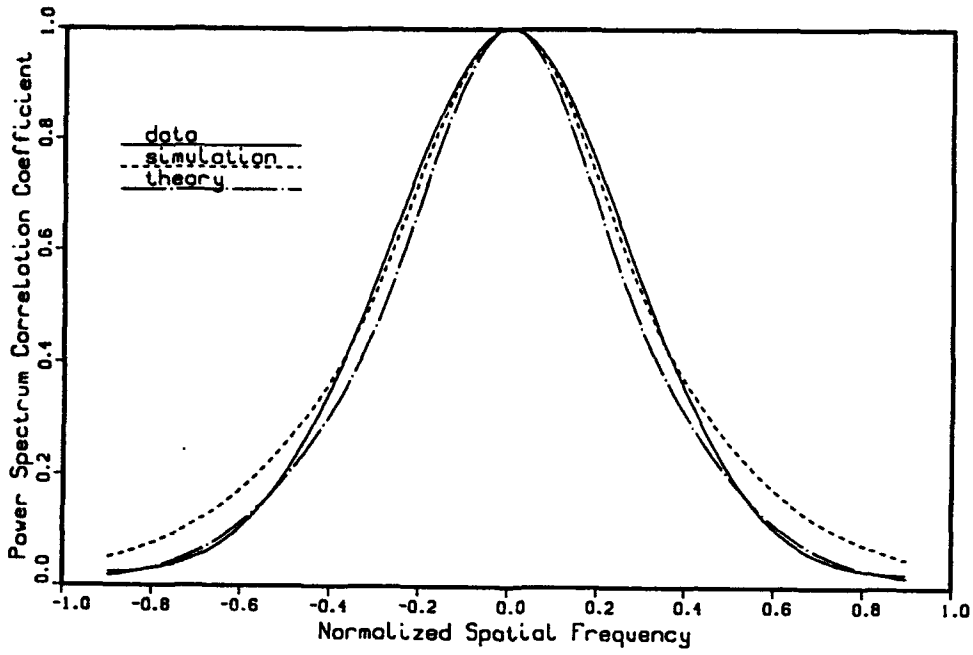

Fig.1: Three correlation coefficient curves for unresolved star power spectra: results from field data collected on Zeta Delphinus, computer simulation prediction, and theoretical prediction. The horizontal axis is angular frequency divided by the seeing cutoff angular frequency r_0/λ.

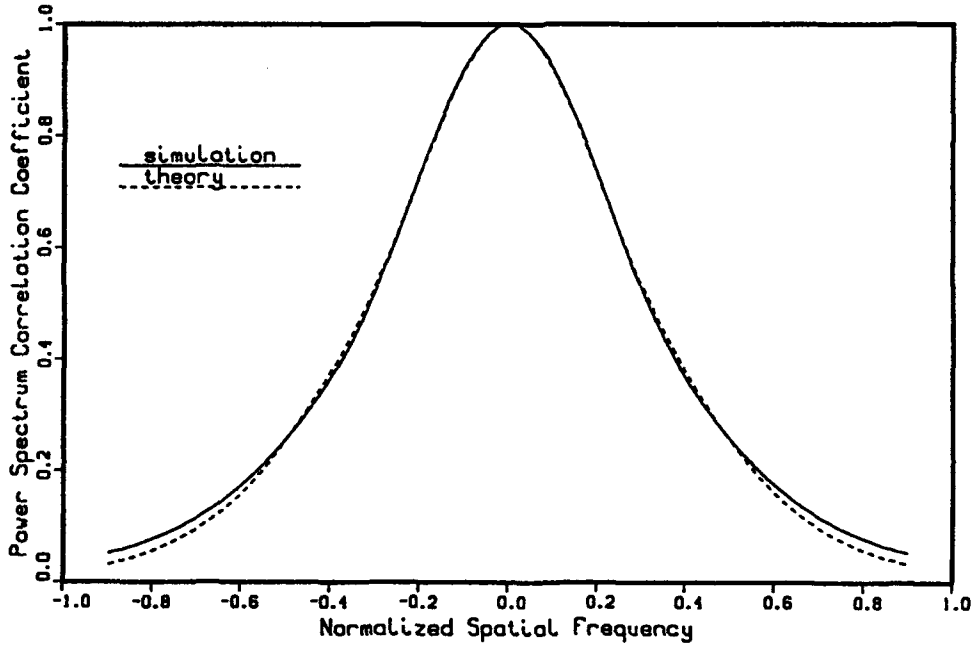

Fig.2: Two correlation coefficient curves for unresolved star power spectra: computer simulated prediction from Fig.1 and improved theoretical prediction. The horizontal axis is angular frequency divided by the seeing cutoff angular frequency r_0/λ.

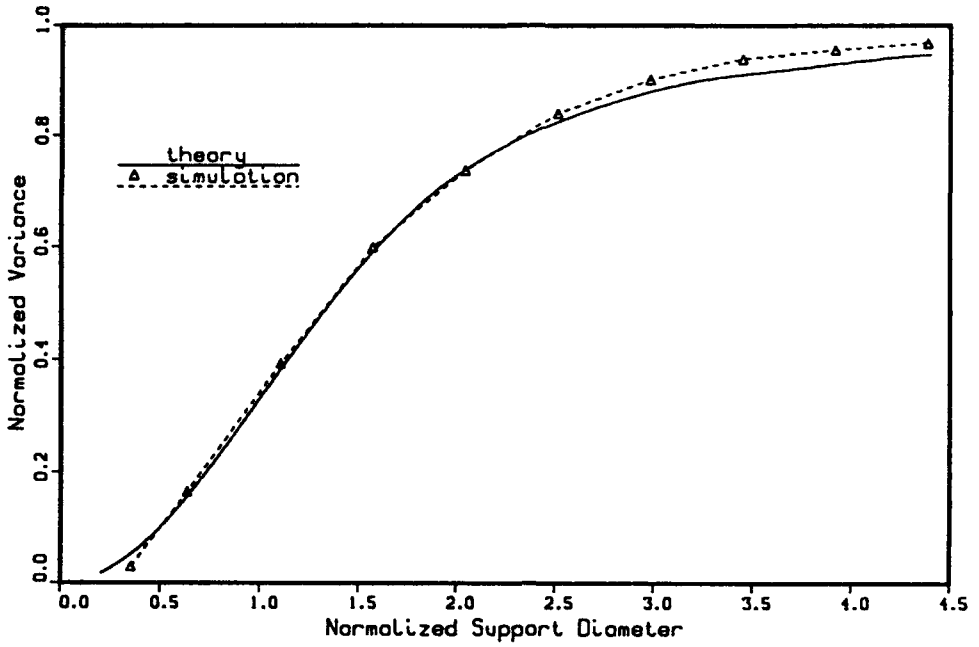

Fig.3: Variance reduction curves for a point source true object: theoretical predictions and results achieved from computer simulations. The horizontal axis is support diameter divided by the seeing disk diameter λ/r_0, and the vertical axis is the reduced variance achieved by applying support constraints divided by the variance obtained without using support constraints. The triangles in the simulation curve are actual datapoints.

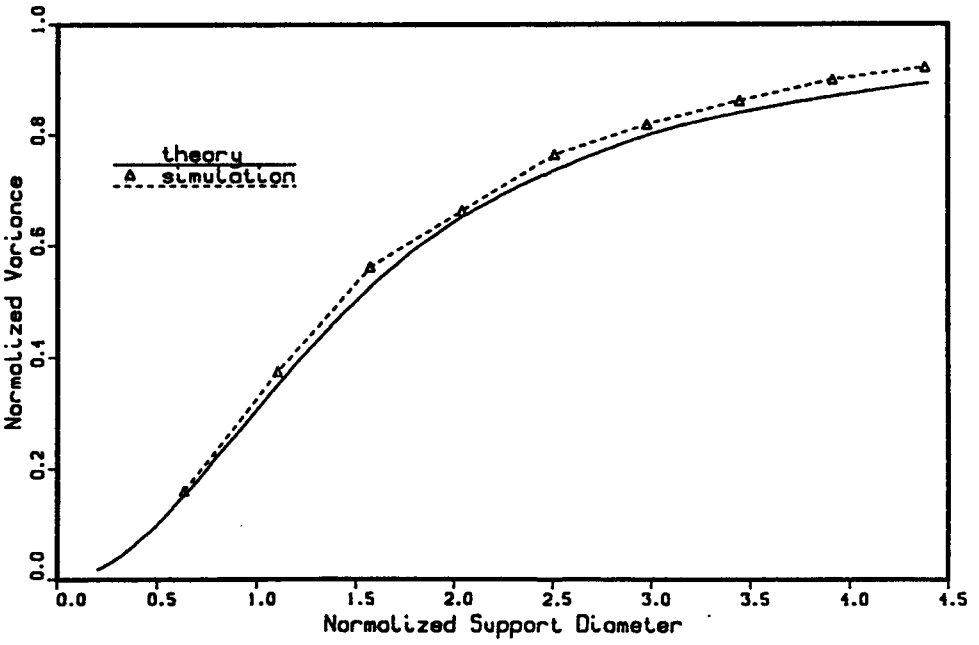

Fig.4: Variance reduction curves for a disk plus point source true object: theoretical predictions and results achieved from computer simulations. The horizontal axis is support diameter divided by the seeing disk diameter λ/r_0, and the vertical axis is the reduced variance achieved by applying support constraints divided by the variance obtained without using support constraints. The triangles in the simulation curve are actual datapoints.

APPENDIX B

Variance Reduction in Fourier Spectra and their Corresponding Images via Support Constraints

Charles L. Matson
Department of Electrical Engineering
Seattle Pacific University
Seattle, WA 98119
(206) 281-3643

Abstract

The use of support constraints for improving the quality of Fourier spectra, their associated images, and the relationship between the two domains is discussed in this paper. Theoretical relationships are derived which predict the noise reduction in both the image domain and the Fourier domain achieved by single and repeated application of support constraints for the case of wide sense stationary Fourier domain noise. It is shown that the application of support constraints can increase noise inside the support constraint if the application is not done correctly. An iterative algorithm is proposed which enforces support constraints in such a way that noise is never increased inside the support constraint and the algorithm achieves the minimum possible noise in a finite number of steps.

1. Introduction

The use of information in addition to measured Fourier data to improve the resolution in reconstructed signals has received a considerable amount of attention over the last five decades[1-7]. In particular, support constraints have been used in a variety of algorithms[1,2] both to achieve superresolution and to reduce the noise corrupting the measured data. In the area of superresolution, it has been shown that support constraints allow some spectral extrapolation to occur, but the amount of superresolution is less than a resolution element for data with moderate signal-to-noise ratios[7]. These superresolution results have been shown to be fundamental limits imposed by the quality of the measured data. In addition, the use of support constraints has been shown to reduce the noise in measured power spectra[7]. However, this work did not discuss the effect that the noise reduction in the power spectrum had upon its inverse Fourier transform, the autocorrelation function.

In this paper, the work discussed in Ref.[7] is extended from power spectra to Fourier spectra which are corrupted by wide sense stationary noise. Furthermore, the image domain consequences of applying support constraints in a repeated manner while requiring the Fourier spectra of the support constrained images to stay close to the measured data is discussed. It is shown that the use of support constraints can result in increased noise in the image domain inside the support constraint if the support constraints are not enforced in an optimal manner. In this paper, an algorithm is proposed which enforces support constraints in such a way that noise inside the support constraint is never increased and, when noise reduction is possible, achieves the minimum noise in a finite number of steps.

The outline of the paper is as follows: Section 2 contains the theory for variance reduction in the Fourier domain as a result of one application of support constraints, section 3 contains results for variance reduction in both the Fourier and image domain as a result of repeated application of support constraints, section 4 contains simulation results, and the conclusions are in section 5.

2. Fourier Domain Variance Reduction

This section contains results which predict the variance reduction in the Fourier domain as a result of one application of support constraints. Let $o(x)$ and $O(u)$ be Fourier transform pairs, where x and u are n-dimensional spatial and spatial frequency vectors, respectively, and $o(x)$ is real. Also, let the support constraint be given by $w(x)$, which also is real. Then, by definition, it follows that

$$o(x) = w(x)o(x) \tag{1}$$

Fourier transforming both sides of Eq.(1) results in

$$O(u) = \int_{-\infty}^{\infty} W(\xi)O(u-\xi)d\xi \tag{2}$$

where $W(u)$ is the Fourier transform of $w(x)$. It can be seen from Eq.(2) that the Fourier spectrum of $o(x)$ at any spatial frequency point u is related to the Fourier spectrum at every other spatial frequency point via the convolution operation. In essence, Eq.(2) shows that applying support constraints results in weighted interpixel averaging with the weights given by the Fourier transform of the window function. Let $O_e(u)$ be the pointwise estimated Fourier spectrum, and let $O_s(u)$ be the improved Fourier spectrum estimate which results from applying support constraints to $O_e(u)$. Then, at each spatial frequency u, it follows from Eq.(2) that

$$O_s(u) = \int_{-\infty}^{\infty} W(\xi) O_e(u-\xi)\,d\xi$$

$$= \int_{-\infty}^{\infty} W_r(\xi) O_{er}(u-\xi)\,d\xi - \int_{-\infty}^{\infty} W_i(\xi) O_{ei}(u-\xi)\,d\xi + j\left[\int_{-\infty}^{\infty} W_r(\xi) O_{ei}(u-\xi)\,d\xi + \int_{-\infty}^{\infty} W_i(\xi) O_{er}(u-\xi)\,d\xi\right] \qquad (3)$$

where the subscripts r and i indicate the real and imaginary parts of the variables, respectively.

It is necessary to calculate the variance of $O_S(u)$ in order to determine the effect support constraints have upon the measured Fourier spectra. Because $O_S(u)$ is a complex number for each u, it is necessary to calculate the variance of both the real and imaginary parts. The variance of $O_{Sr}(u)$, var$\{O_{Sr}(u)\}$, is given by

$$\text{var}\{O_{sr}(u)\} \equiv \langle [O_{sr}(u)]^2 \rangle - \langle O_{sr}(u) \rangle^2$$

$$= \left\langle \int_{-\infty}^{\infty} W_r(\xi) O_{er}(u-\xi)\,d\xi \int_{-\infty}^{\infty} W_r(\zeta) O_{er}(u-\zeta)\,d\zeta \right\rangle - \left\langle \int_{-\infty}^{\infty} W_r(\xi) O_{er}(u-\xi)\,d\xi \right\rangle \left\langle \int_{-\infty}^{\infty} W_r(\zeta) O_{er}(u-\zeta)\,d\zeta \right\rangle$$

$$+ \left\langle \int_{-\infty}^{\infty} W_i(\xi) O_{ei}(u-\xi)\,d\xi \int_{-\infty}^{\infty} W_i(\zeta) O_{ei}(u-\zeta)\,d\zeta \right\rangle - \left\langle \int_{-\infty}^{\infty} W_i(\xi) O_{ei}(u-\xi)\,d\xi \right\rangle \left\langle \int_{-\infty}^{\infty} W_i(\zeta) O_{ei}(u-\zeta)\,d\zeta \right\rangle$$

$$- 2\left\langle \int_{-\infty}^{\infty} W_r(\xi) O_{er}(u-\xi)\,d\xi \int_{-\infty}^{\infty} W_i(\zeta) O_{ei}(u-\zeta)\,d\zeta \right\rangle + 2\left\langle \int_{-\infty}^{\infty} W_r(\xi) O_{er}(u-\xi)\,d\xi \right\rangle \left\langle \int_{-\infty}^{\infty} W_i(\zeta) O_{ei}(u-\zeta)\,d\zeta \right\rangle$$

$$= \int\int_{-\infty}^{\infty} W_r(\xi) W_r(\zeta) \left[\langle O_{er}(u-\xi) O_{er}(u-\zeta) \rangle - \langle O_{er}(u-\xi) \rangle \langle O_{er}(u-\zeta) \rangle \right] d\xi\, d\zeta$$

$$+ \int\int_{-\infty}^{\infty} W_i(\xi) W_i(\zeta) \left[\langle O_{ei}(u-\xi) O_{ei}(u-\zeta) \rangle - \langle O_{ei}(u-\xi) \rangle \langle O_{ei}(u-\zeta) \rangle \right] d\xi\, d\zeta$$

$$- 2\int\int_{-\infty}^{\infty} W_r(\xi) W_i(\zeta) \left[\langle O_{er}(u-\xi) O_{ei}(u-\zeta) \rangle - \langle O_{er}(u-\xi) \rangle \langle O_{ei}(u-\zeta) \rangle \right] d\xi\, d\zeta \qquad (4)$$

where the angle brackets denote expectation. Similarly, it follows that

$$\mathrm{var}\{O_{si}(u)\} \equiv \langle [O_{si}(u)]^2 \rangle - \langle O_{si}(u) \rangle^2$$

$$= \int_{-\infty}^{\infty}\int W_r(\xi)W_r(\zeta)\left[\langle O_{ei}(u-\xi)O_{ei}(u-\zeta)\rangle - \langle O_{ei}(u-\xi)\rangle\langle O_{ei}(u-\zeta)\rangle\right]d\xi d\zeta$$

$$+ \int_{-\infty}^{\infty}\int W_i(\xi)W_i(\zeta)\left[\langle O_{er}(u-\xi)O_{er}(u-\zeta)\rangle - \langle O_{er}(u-\xi)\rangle\langle O_{er}(u-\zeta)\rangle\right]d\xi d\zeta$$

$$+ 2\int_{-\infty}^{\infty}\int W_r(\xi)W_i(\zeta)\left[\langle O_{ei}(u-\xi)O_{er}(u-\zeta)\rangle - \langle O_{ei}(u-\xi)\rangle\langle O_{er}(u-\zeta)\rangle\right]d\xi d\zeta \qquad (5)$$

To analyze these equations further, more information needs to be known about $O_e(u)$ in order that the expectations in Eqs.(4) and (5) can be evaluated. Therefore, define

$$\begin{aligned} N_r(u) &= O_{er}(u) - \langle O_{er}(u)\rangle \\ N_i(u) &= O_{ei}(u) - \langle O_{ei}(u)\rangle \end{aligned} \qquad (6)$$

where the complex noise (N_r, N_i) is a stochastic process which satisfies

$$\begin{aligned} \langle N_r(u_1)N_r(u_2)\rangle &= R_r(u_1-u_2) + R_r(u_1+u_2) \\ \langle N_i(u_1)N_i(u_2)\rangle &= R_i(u_1-u_2) - R_i(u_1+u_2) \\ \langle N_i(u_1)N_r(u_2)\rangle &= \langle N_r(u_1)N_i(u_2)\rangle = 0 \end{aligned} \qquad (7)$$

This model for the noise is general enough to include both CCD read noise and Poisson noise. The restriction that the covariance between the real and the imaginary is zero implies that the variance of the noise in the image domain is an even function of x. This restriction is made for clarity and simplicity. Also, for clarity and simplicity, the terms in Eq.(7) which are functions of u_1+u_2 will be neglected since, in general, their influence is relatively minor for all frequencies except those near dc. This results in Fourier domain noise which is wide sense stationary. Then, by substituting Eqs (6) and (7) into Eqs.(4) and (5) with this simplification, it follow that

$$\mathrm{var}\{O_{sr}(u)\} = \int_{-\infty}^{\infty}\int \left[W_r(\xi)W_r(\zeta)R_r(\xi-\zeta) + W_i(\xi)W_i(\zeta)R_i(\xi-\zeta)\right]d\xi d\zeta \qquad (8)$$

$$\mathrm{var}\{O_{si}(u)\} = \int_{-\infty}^{\infty}\int \left[W_r(\xi)W_r(\zeta)R_i(\xi-\zeta) + W_i(\xi)W_i(\zeta)R_r(\xi-\zeta)\right]d\xi d\zeta \qquad (9)$$

There are several interesting asymptotic properties that Eqs.(8) and (9) exhibit. The first is that, as the imaginary part of the window approaches zero, the variance reduction in the real (imaginary) part comes just from averaging the real (imaginary) parts, and thus there is no crosstalk between the real and imaginary components.

Two other asymptotic properties can be seen much more easily by rewriting Eqs.(8) and (9). Using the convolution-multiplication relationship between the Fourier and inverse Fourier domains, it can be easily shown that

$$\mathrm{var}\{O_{sr}(u)\} = \int_{-\infty}^{\infty} w_e^2(x) r_r(x)dx + \int_{-\infty}^{\infty} w_o^2(x) r_i(x)dx \tag{10a}$$

$$\mathrm{var}\{O_{si}(u)\} = \int_{-\infty}^{\infty} w_e^2(x) r_i(x)dx + \int_{-\infty}^{\infty} w_o^2(x) r_r(x)dx \tag{10b}$$

where $w_e(x)$ [=(w(x)+w(-x))/2] is the even part of w(x), $w_O(x)$ [=(w(x)-w(-x))/2] is the odd part of w(x), $r_r(x)$ is the inverse Fourier transform of $R_r(u)$, and $r_i(x)$ is the inverse Fourier transform of $R_i(u)$. Furthermore, it will prove useful to rewrite Eq.(10) in an alternate form. Let

$$\begin{aligned} w_e(x) &= w_s(x) + \frac{1}{2}\left[w_a(x) + w_{-a}(x)\right] \\ w_o(x) &= \frac{1}{2}\left[w_a(x) - w_{-a}(x)\right] \end{aligned} \tag{11}$$

where $w_S(x)$ is the symmetric part of w(x), $w_a(x)$ [=w(x)-$w_S(x)$] is the asymmetric part of w(x), and $w_{-a}(x) = w_a(-x)$. It is also easy to show that

$$\begin{aligned} w_e^n(x) &= w_s(x) + 2^{-n}\left[w_a(x) + w_{-a}(x)\right] \\ w_o^n(x) &= 2^{-n} w_a(x) + (-2)^{-n} w_{-a}(x) \end{aligned} \tag{12}$$

because the support functions w_S, w_a, and w_{-a} have no intersection. Then, by substituting Eq.(12) into Eq.(10) and by using the fact that $r_i(x)$ and $r_r(x)$ are even functions, it follows that

$$\mathrm{var}\{O_{sr}(u)\} = \int_{w_s(x)} r_r(x)dx + \frac{1}{2}\int_{w_a(x)} \left[r_i(x) + r_r(x)\right]dx \tag{13a}$$

$$\mathrm{var}\{O_{si}(u)\} = \int_{w_s(x)} r_i(x)dx + \frac{1}{2}\int_{w_a(x)} \left[r_i(x) + r_r(x)\right]dx \tag{13b}$$

Notice that the variances of the real and imaginary parts are now expressed in terms of the noises in the symmetric and asymmetric regions of the support function. This will be useful in the next section where image domain noise reduction is discussed.

Consider now the case when the support becomes very large and the Fourier domain noise is not white noise. For simplicity, assume that the support constraint is centered on the origin and expanded equally in all directions (this does <u>not</u> imply that the support constraint is symmetric, however). Then, as the support becomes arbitrarily large, the integral over $w_a(x)$ will go to zero, $w_S(x)$ will be large enough so that $r_r(x)$ and $r_i(x)$ will be essentially nonzero outside of $w_S(x)$, and then Eq.(13) becomes

$$\mathrm{var}\{O_{sr}(u)\} \approx \int_{-\infty}^{\infty} r_r(x)dx = R_r(0) \tag{14a}$$

$$\mathrm{var}\{O_{si}(u)\} \approx \int_{-\infty}^{\infty} r_i(x)dx = R_i(0) \tag{14b}$$

Thus, when the support constraint becomes arbitrarily large, no improvement is seen in the variance of $O_S(u)$ for nonwhite noise. However, if the Fourier domain noise is truly white, then support constraints will always result in variance reduction regardless of the size of the support constraint.

The third, and final, asymptotic property occurs when the support constraint becomes arbitrarily small and the Fourier domain noise is allowed to have any degree of correlation. Again assume that the support constraint is centered on the origin. Then, as the support constraint gets very small, eventually $r_r(x)$ and $r_i(x)$ are approximately constant and equal to $r_r(0)$ and $r_i(0)$, respectively, in the support region. Then Eq.(13) becomes

$$\mathrm{var}\{O_{sr}(u)\} \approx r_r(0) \int_{w_s(x)} dx + \frac{1}{2}[r_i(0)+r_r(0)] \int_{w_s(x)} dx \tag{15a}$$

$$\mathrm{var}\{O_{si}(u)\} \approx r_i(0) \int_{w_s(x)} dx + \frac{1}{2}[r_i(0)+r_r(0)] \int_{w_s(x)} dx \tag{15b}$$

and so the variances approach zero as the support area approaches zero. From Eqs.(10)-(15), it can be seen that one application of support constraints always results in some degree of variance reduction in the measured Fourier spectra, and under the right conditions can drive the variances arbitrarily close to zero.

3. Image Domain Variance Reduction

All of the results derived in the previous section are theoretical predictions for variance reductions in Fourier spectra resulting from a single application of support constraints in the image domain. However, it is necessary to look at what happens in the image domain since the primary goal of using support constraints or any other additional information is to improve the quality of the image inside the support constraint. Because of the invertibility of the Fourier transform, all the Fourier domain variance reductions discussed in section 2 are purely a result of zeroing out noise in the image domain outside of the known support. These variance reductions do not improve the quality of the image inside the support constraints and, as such, do not achieve any image quality improvement since it was already known that the image was zero outside the support. Therefore, a question naturally arises: are there any circumstances in which support constraints can improve image quality inside the support constraint? The answer is yes, and this section contains derivations which will specify what conditions are necessary for this to occur. The first observation to be made is that, if no change in made in $O_S(u)$ prior to inverse Fourier transforming, then reapplying the support constraint in the image domain is entirely redundant and no further variance reduction will occur in the Fourier domain. Also, no change in image quality inside the support constraint will occur. The question then arises, what would motivate changes in $O_S(u)$ prior to inverse Fourier transforming?

To analyze this question in more depth, it is important to realize what information is available in the Fourier domain. There exists measured Fourier data and also sample variances which provide a means to determine the quality of the measured Fourier data. Clearly, if by applying support constraints, the variance of $O_S(u)$ for all spatial frequencies is smaller than the variance of the measured Fourier data, then the measured data should not be used to force a change in $O_S(u)$, and thus the application of support constraints cannot be used to reduce the image domain noise inside the support constraint. Conversely, if by applying support constraints, the

variance of $O_s(u)$ for some spatial frequencies is larger than the variance of the measured Fourier data, it would make sense to replace those components of $O_s(u)$ with the measured Fourier data components. Only in this case would it be possible to lower the noise levels inside the support constraint. Therefore, the next question is, when would support constraints increase the variance of $O_s(u)$ for some spatial frequencies? To answer this question, it is first necessary to determine under what conditions support constraints do not increase the variances of $O_s(u)$ beyond the variances of $O_e(u)$ for any spatial frequency.

First, assume that the window function is symmetric so that there is no imaginary part to W(u). Then $w_a(x)$ is zero and Eq.(13) becomes

$$\mathrm{var}\{O_{sr}(u)\} = \int_{w_s(x)} r_r(x)dx \tag{16a}$$

$$\mathrm{var}\{O_{si}(u)\} = \int_{w_s(x)} r_i(x)dx \tag{16b}$$

Because $r_r(x)$ and $r_i(x)$ are nonnegative functions, restricting the integration from all x to $w_s(x)$ will never cause the variances to increase. Therefore, it is necessary to have an imaginary component to W(u) in order to have the possibility of increasing some variances of $O_s(u)$ beyond those of $O_e(u)$. This is equivalent to saying that the support function must have some asymmetry. However, the conclusion that the support constraint must have some asymmetry is a result of the noise being wide sense stationary. For nonstationary noise, this conclusion is not necessarily valid.

The next case in which the variances of $O_s(u)$ will always be less than or equal to the variances of $O_e(u)$ is when the noises corrupting the real and imaginary parts of $O_e(u)$ are identically distributed. In this case, Eq.(13) becomes

$$\mathrm{var}\{O_{sr}(u)\} = \int_{w(x)} r_r(x)dx = \mathrm{var}\{O_{si}(u)\} \tag{17}$$

It is clear that the variances of the real and imaginary parts are no greater than the variances of the measured data, so again there will be no reason to modify $O_s(u)$ due to increased variances and thus the applied support constraints will have no effect on the image inside the support constraint. However, this case does indicate under what conditions there might be a reason to modify spectral points of $O_s(u)$ because they have higher variances than $O_e(u)$. That is, Eq.(13) indicates that the application of support constraints causes coupling of the noises between the real and imaginary parts of the spectrum which is due to the noise in the asymmetric portions of the support constraint. If the noises are sufficiently different in magnitude, then the application of an asymmetric support constraint will decrease the variance of the imaginary part of $O_s(u)$ (the real part of $O_s(u)$) but increase the variance of the real part of $O_s(u)$ (the imaginary part of $O_s(u)$) beyond that of the measurements. Therefore, it appears that the only time support constraints can be used to improve image quality inside the support constraint is when either the real or imaginary component has a sufficiently lower noise variance than the other and the support constraint is not symmetric.

To pursue this further, assume that the real part of $O_e(u)$ is less noisy that the imaginary part. Because both parts of Eq.(13) have the same form, these results will also apply to the case of the imaginary part being less noisy than the real merely by interchanging the real and imaginary covariances. Therefore, it makes sense to employ an iterative algorithm which replaces the support constrained real part of the Fourier transform with the real part of the measured Fourier data on each iteration while leaving the imaginary component unchanged. Thus, the algorithm is as follows: (1) inverse Fourier transform $O_e(u)$, (2) apply support constraints, (3) Fourier transform, (4) replace the real part of the Fourier estimate with the measured data, but keep the imaginary components unchanged, (5) go back to step 1 and repeat until the noise is minimized inside the support constraint.

Now it will be shown that, using this algorithm, that both the real and imaginary components converge and what they converge to. First consider the imaginary part of the Fourier transform: after m iterations of the algorithm, the imaginary component will be given by

$$O_{si(m)}(u) = \mathcal{F}\left\{w_e^m(x)\mathcal{F}^{-1}[O_{ei}(u)]\right\} - j\sum_{k=0}^{m-1}\mathcal{F}\left\{w_e^k(x)w_o(x)\mathcal{F}^{-1}[O_{er}(u)]\right\} \quad (18)$$

where $\mathcal{F}$ and $\mathcal{F}$-1 denote the Fourier and inverse Fourier transform operation, respectively. This result can be derived by repeated application of Eq.(3). Using Eq.(18) and following the methods used to derive Eq.(13), it can be shown that the variance of $O_{si(m)}$ is given by

$$\begin{aligned}
\mathrm{var}\{O_{si(m)}(u)\} &= \int_{-\infty}^{\infty}\left[w_s(x) + 2^{-2m}(w_a(x)+w_{-a}(x))\right]r_i(x)dx \\
&+ \int_{-\infty}^{\infty}\frac{1}{4}(w_a(x)+w_{-a}(x))\sum_{k=0}^{m-1}\left[w_s(x)+\frac{k+1}{2^k}(w_a(x)+w_{-a}(x))\right]r_r(x)dx \\
&+ \int_{-\infty}^{\infty}\frac{1}{4}(w_a(x)+w_{-a}(x))\sum_{k=m}^{2m-2}\left[w_s(x)+\frac{2m-1-k}{2^k}(w_a(x)+w_{-a}(x))\right]r_r(x)dx \\
&= \int_{w_a(x)} r_i(x)dx + \int_{w_a(x)} 2^{(1-2m)}r_i(x)dx + \frac{1}{2}\left[\sum_{k=0}^{m-1}\frac{k+1}{2^k} + \sum_{k=m}^{2m-2}\frac{2m-1-k}{2^k}\right]\int_{w_a(x)} r_r(x)dx
\end{aligned} \quad (19)$$

where, in this equation and all following equations, the summation terms are zero if the upper limit is less than the lower limit. Now, in the limit as $m\to\infty$, the first summation approaches four, the second approaches zero, the second integral goes to zero, and it follows that

$$\mathrm{var}\{O_{si(\infty)}(u)\} = \int_{w_a(x)} r_i(x)dx + 2\int_{w_a(x)} r_r(x)dx \quad (20)$$

In a similar way, it can be shown that, after m iterations of the algorithm, the real part of the Fourier transform is given by

$$O_{sr(m)}(u) = \mathcal{F}\left\{w_e(x)\mathcal{F}^{-1}[O_{er}(u)]\right\} + j\,\mathcal{F}\left\{w_o(x)w_e^{m-1}(x)\mathcal{F}^{-1}[O_{ei}(u)]\right\} + \sum_{k=0}^{m-2}\mathcal{F}\left\{w_e^k(x)w_o^2(x)\mathcal{F}^{-1}[O_{er}(u)]\right\} \quad (21)$$

and the variance of $O_{sr(m)}$ is given by

$$\begin{aligned}
\mathrm{var}\{O_{sr(m)}(u)\} &= \int_{w_a(x)} r_r(x)dx + \int_{w_a(x)} 2^{(1-2m)}r_i(x)dx \\
&+ \left[\frac{1}{2} + \sum_{k=1}^{m-1}\frac{1}{2^k} + \frac{1}{8}\sum_{k=0}^{m-2}\frac{k+1}{2^k} + \frac{1}{8}\sum_{k=m-1}^{2m-4}\frac{2m-3-k}{2^k}\right]\int_{w_a(x)} r_r(x)dx
\end{aligned} \quad (22)$$

In the limit as $m \to \infty$, the first summation approaches one, the second approaches one half, the third approaches zero, the second integral goes to zero, and it follows that

$$\mathrm{var}\{O_{sr(\infty)}(u)\} = \int_{w_s(x)} r_r(x)dx + 2\int_{w_s(x)} r_r(x)dx \tag{23}$$

It is interesting to note that Eq.(22) indicates that the variance of the real part of the support constrained Fourier spectrum changes even though, on each iteration, the measured data replaces the support constrained real part. This is due to coupling between the real and imaginary parts enforced by the support constraint.

Notice in the previous equations that the changes in the variances of the real and imaginary support constrained components are due to changes in the noise in the asymmetric portions of the support constraint. Furthermore, because the goal of applying support constraints is to minimize noise in the image, not the Fourier spectrum, it is necessary to determine how the noise variances inside the support constraint in the image domain change as a function of the number of algorithm iterations. To this end, let $n_m(x)$ be the noise in the image domain after m iterations of the algorithm which results from the inverse Fourier transform of $(N_{r(m)}, N_{i(m)})$. Then it follows that $\langle n_m(x)\rangle = 0$ and that

$$\langle n_m(x_1)n_m(x_2)\rangle = \left\langle \int_{-\infty}^{\infty}\left[N_{r(m)}(u_1) + jN_{i(m)}(u_1)\right]e^{j2\pi x_1 u_1}du_1 \int_{-\infty}^{\infty}\left[N_{r(m)}(u_2) - jN_{i(m)}(u_2)\right]e^{-j2\pi x_2 u_2}du_2 \right\rangle$$

$$= \int_{-\infty}^{\infty}\int_{-\infty}^{\infty}\left[\langle N_{r(m)}(u_1)N_{r(m)}(u_2)\rangle + \langle N_{i(m)}(u_1)N_{i(m)}(u_2)\rangle - j\langle N_{r(m)}(u_1)N_{i(m)}(u_2)\rangle\right.$$

$$\left. + j\langle N_{i(m)}(u_1)N_{r(m)}(u_2)\rangle\right]e^{j2\pi x_1 u_1}e^{-j2\pi x_2 u_2}du_2 du_1 \tag{24}$$

After making a change of variables from u_1 to $\Delta u = (u_1 - u_2)$, it follows that

$$\langle n_m(x_1)n_m(x_2)\rangle = \int_{-\infty}^{\infty}\int_{-\infty}^{\infty}\left[R_{r(m)}(\Delta u) + R_{i(m)}(\Delta u) + jR_{ir(m)}(\Delta u) - jR_{ri(m)}(\Delta u)\right]e^{j2\pi x_1 \Delta u}e^{j2\pi(x_1 - x_2)u_2}d(\Delta u)du_2$$

$$= \mathcal{F}^{-1}\left\{R_{r(m)}(u) + R_{i(m)}(u) + jR_{ir(m)}(u) - jR_{ri(m)}(u)\right\}\delta(x_1 - x_2) \tag{25}$$

where $R_{r(m)}$ is the autocovariance of the real part of the Fourier domain noise, $R_{i(m)}$ is the autocovariance of the imaginary part of the Fourier domain noise, and $R_{ir(m)}$ and $R_{ri(m)}$ are the cross-covariances of the imaginary and the real and the real and the imaginary parts of the Fourier domain noise, respectively, after m iterations. $R_{r(m)}$ and $R_{i(m)}$ can be obtained by generalizing Eqs.(19) and (22), and $R_{ir(m)}$ and $R_{ri(m)}$ can be derived from Eqs.(18) and (21). Substituting these expressions into Eq.(25) gives

$$\sigma_m^2(x) \equiv \mathcal{F}^{-1}\left\{R_{r(m)}(u)+R_{i(m)}(u)+jR_{ir(m)}(u)-jR_{ri(m)}(u)\right\}$$

$$= \left[r_r(x)+r_i(x)\right]w_a(x) \;+\; 2^{(2-2m)}r_i(x)w_a(x) \;+\; \frac{1}{2}\left[\sum_{k=0}^{m-1}\frac{k+1}{2^k}+\sum_{k=m}^{2m-2}\frac{2m-1-k}{2^k}\right]w_a(x)r_r(x)$$

$$+\left[\frac{1}{2}+\sum_{k=1}^{m-1}\frac{1}{2^k}+\frac{1}{8}\sum_{k=0}^{m-2}\frac{k+1}{2^k}+\frac{1}{8}\sum_{k=m-1}^{2m-4}\frac{2m-3-k}{2^k}\right]w_a(x)r_r(x) \qquad (26)$$

and, as $m\rightarrow\infty$,

$$\sigma_\infty^2(x)=\left[r_r(x)+r_i(x)\right]w_a(x)+4r_r(x)w_a(x) \qquad (27)$$

Eq.(27) implies that the more asymmetric the object and the less noisy the real part of the measured spectra, the lower the variance of the image domain noise inside the support constraint. If the support of the object is completely asymmetric, then the noise in the image is completely determined by the noise in the real part of the Fourier spectrum. Thus it could be construed that, if the object is moved off center sufficiently far, then support constraints can be used to completely remove all the noise from the image if the real portion of the Fourier data was noise free. This is true under the assumptions of the noise model used in the theoretical derivation. However, if the object is not centered in the image plane, the assumption of uncorrelated real and imaginary noises is no longer valid due to the induced tilt.

The noise in the image domain within the support constraint is given by Eq.(26), and it is clear that the noise within the symmetric portion of the support constraint is unaffected by repeated support constraint applications. However, the noise in the asymmetric portion is a function of the number of support applications. It is not clear from Eq.(26) the number of iterations needed to minimize the noise inside the support constraint. Therefore, to determine the number of iterations to reach the minimum noise level, it is necessary to calculate the difference in the variances between the m and the (m-1) iteration and determine when the difference stops being negative and becomes positive. After some algebraic manipulation, the desired difference is given by

$$\sigma_m^2(x)-\sigma_{m-1}^2(x)=\frac{1}{2^{2m}}\left\{\left[\left(5+\sum_{k=0}^{m-4}\frac{1}{2^k}+\sum_{k=0}^{m-5}\frac{1}{2^{k+1}}\right)2^m+20\right]r_r(x)-12r_i(x)\right\}w_a(x) \qquad ;\; m\geq 4$$

$$=\frac{1}{16}\left[13r_r(x)-3r_i(x)\right]w_a(x) \qquad ;\; m=3$$

$$=\frac{1}{4}\left[5r_r(x)-3r_i(x)\right]w_a(x) \qquad ;\; m=2 \qquad (28)$$

Notice that the only region in the image domain where variances are changing as a result of the algorithm is in the asymmetric region of the support constraint. Also notice that the term in Eq.(28) which causes $\sigma_m^2(x)-\sigma_{m-1}^2(x)$ to be negative, and thus decrease the error in the support constraint from the previous step, is $r_i(x)$ multiplied by a constant factor. However, the positive term consists of $r_r(x)$ multiplied by an increasing function of m which approaches ∞ as $m\rightarrow\infty$, and thus $\sigma_m^2(x)-\sigma_{m-1}^2(x)$ becomes positive for some finite value of m as long as $r_r(x)>0$. This means that the number of iterations needed to achieve the minimum amount of noise inside the support constraint is a finite number (for $r_r(x)>0$) and increasing the iterations beyond this level will increase the noise. If $r_r(x)=0$, then the noise levels inside the support constraint decrease for every value of m and the minimum noise

level occurs for m=∞. If the ratio $r_r(x)/r_i(x)$ is large enough, then $\sigma_m^2(x) - \sigma_{m-1}^2(x)$ will always be positive for more than one application of support constraints and there is no possibility of reducing the error in the image domain inside the support constraint. The upper bound for $r_r(x)/r_i(x)$ that allows a decrease in the image domain variance via repeated applications of support constraints can be determined by setting $\sigma_m^2(x) - \sigma_{m-1}^2(x)$ equal to zero for m=2 and solving for $r_r(x)/r_i(x)$, which results in

$$\frac{r_r(x)}{r_i(x)} = \frac{3}{5} \tag{29}$$

Thus, if the noise properties are known, it can be determined a priori whether or not support constraints can be used to lower the amount of noise inside the support constraint.

The results contained in Eqs.(26)-(29) reflect the variance properties of the noise in the image domain at each point. However, in general $r_r(x)$ and $r_i(x)$ will have different functional forms, and thus the number of iterations needed to minimize the variance in the image domain will be a function of x. Therefore, it is necessary to calculate the integral of the variance of the noise over all x to determine the number of iterations required to minimize the total noise in the image. This is easily accomplished by replacing all the functions of x in Eqs.(26)-(29) with their integrals over x. In particular, it is easy to show that Eq.(29) becomes

$$\frac{\int_{w_s(x)} r_r(x)dx}{\int_{w_s(x)} r_i(x)dx} = \frac{3}{5} \tag{30}$$

which determines the dividing line between support constraints being able to reduce noise inside the support constraint or not relative to the total noise in the image domain.

All of the above results occur when the real part of the support constrained Fourier spectrum is kept equal to the measured data while letting the imaginary become what the support constraints require. An obvious alternative to this algorithm is to constrain both the real and imaginary parts of the measured Fourier data at each iteration to stay within some region about its mean value, typically determined from the variances of the noises. This has been the suggested approach to use when employing a convex projections approach to include additional information[8,9]. However, it will be shown via computer simulation in the next section that this modification to the algorithm usually results in more noise than the original algorithm.

4. Computer Simulation Results

The first step undertaken in the computer simulation effort was to validate the theoretical derivations in the previous section. To this end, an off-axis point source was used as the uncorrupted object. It was then Fourier transformed and zero mean gaussian complex white noise with real and imaginary variances σ_r^2 and σ_i^2, respectively, was added for various σ_r^2/σ_i^2 ratios. This results in $r_i(x) = \sigma_i^2$ and $r_r(x) = \sigma_r^2$. Because the results are completely symmetric for $\sigma_r^2 > \sigma_i^2$, results for $\sigma_r^2 < \sigma_i^2$ only are shown. In addition, because the noise is delta-correlated, the terms in Eq.(7) which are functions of u_1+u_2 are zero except at dc. All simulations used the mean of the measured Fourier data and the true (not estimated) variance of the noise to determine the Fourier domain constraints.

For each dataset, the algorithm described in the previous section was used to apply support constraints until the algorithm converged. The support constraint applied was a triangle which partially overlaps the origin so that the area of the triangle which is asymmetric about the origin is 83% of the total triangle area. Sample variances were calculated at each spatial frequency and at each point inside the support and averaged at each iteration to provide sample variances of the support constrained Fourier spectrum and of the image before the real part was replaced with the initial data. Fig.1 shows the theoretical predictions and simulation results for the real

part of the support constrained Fourier spectra, Fig.2 shows the same results for the imaginary part of the support constrained Fourier spectra, and Fig.3 shows the total variance inside the asymmetric part of the support constraint. The symmetric part is not shown because, as predicted by Eq.(28), it remains unchanged during the repeated application of support constraints. Notice the close match between simulation and theory. It can be seen in Fig.3 that there is no change in the variance between the first and second iteration for $\sigma_r^2/\sigma_i^2=0.6$, and then the noise increases. This result confirms the theoretical prediction given by Eq.(29).

These results were obtained by constraining the real part of the support constrained Fourier data to match the measured Fourier data at each iteration, but the imaginary part was left unconstrained. Next, these results were compared to the results obtained by requiring both the real and imaginary parts of the support constrained Fourier data to remain within a specified region about the measured Fourier data. Prior to implementing this modification to the algorithm, the Fourier data was smoothed using the results of Eq.(16); that is, Eq.(16) predicts that the result of applying a symmetric support constraint will be a decrease in the variance of both the real and imaginary parts of the Fourier spectrum. Of course, this does not decrease the noise inside the support constraint in the image domain, but it can be used to decrease the noise in the Fourier data before using it as a constraint. For this part of the computer simulation, the smallest symmetric support constraint that included the actual support constraint was calculated, the initial data was smoothed, and a reduced variance σ_s^2 was calculated using Eq.(16). This smoothed data with the refined variance estimate was then used for the initial data in the algorithm. Fig.4 compares the results from the original algorithm and the modified algorithm for the case where $\sigma_r^2/\sigma_i^2=1$ and where the Fourier domain constraint was that the support constrained Fourier spectrum was required to stay with $\pm 1\sigma$ of the smoothed data. Bounds of $\pm 2\sigma$ and $\pm 3\sigma$ were also used, but the results were very similar to the $\pm 1\sigma$ case. The result of running this modified algorithm until it converged was increased noise both in the symmetric and asymmetric parts of the support constraint. As predicted by Eq.(29), noise reduction is not possible for a noise ratio of $\sigma_r^2/\sigma_i^2=1$. Notice that, for m>2, the modified algorithm resulted in lower noise levels inside the support constraint, but it still increased the noise inside the support constraint.

The results from using the modified algorithm for the case of $\sigma_r^2/\sigma_i^2=0.6$ (which is the borderline case for noise reduction using support constraints) are shown in Fig.5. In this case, the modified algorithm resulted in increased noise inside the support constraint if the algorithm was run until convergence is achieved. If, however, the algorithm had been stopped at the second iteration, the modified algorithm resulted in slightly less noise than the original algorithm. Once again, the modified algorithm resulted in increased noise in the symmetric part of the support constraint.

The third case to be looked at is for $\sigma_r^2/\sigma_i^2=0.2$. The results can be seen in Fig.6. Notice that the original algorithm results in lower noise levels in the image as compared to the results from using the modified algorithm. It is clear from looking at these three examples that, if the noise statistics are known, it can be decided a priori whether support constraints will increase or decrease the noise inside the support constraint. If the noise levels will decrease, then the original algorithm produces the best or comparable results as compared to the modified algorithm as long as the iteration number for which the minimum is obtained is calculated and the algorithm is stopped at that point. If the noise statistics are not known, the modified algorithm using the smoothed data is the best compromise to using support constraints if one is unsure whether support constraints will result in increased or decreased noise in the image. Although the modified algorithm does not achieve the minimum noise in the image, in general, excessive noise in the image is also avoided.

As a final example, a satellite model was used as the true object. Fig.7 shows the model used, and Fig.8 shows the support of the satellite. The white region of the support is the symmetric region, and the gray region is the asymmetric region. Zero mean white gaussian noise with a variance equal to 10^7 times the dc value of the image was added to the imaginary part of the satellite's Fourier transform, but the real part was kept noise-free. From Eq.(29) it follows then that the minimum noise level is reached only at infinity. The noisy image is shown in Fig.9, where the satellite image is completely masked by the noise. The original algorithm was run for 20 iterations, replacing the noisy real part of the Fourier transform of the support constrained image with the noise-free data each iteration. The resulting image is shown in Fig.10. Notice, by comparing Fig.8 with Fig.10 that the noise in the symmetric part of the image remained unchanged, while the asymmetric part of the image is now essentially noise-free.

5. Conclusions

Theoretical results have been derived which predict the effects of repeated applications of support constraints in both the image and Fourier domain for the case of wide sense stationary Fourier domain noise. These results assume that, for each iteration of the algorithm, the initially less noisy part of the Fourier spectrum (real or imaginary) replaces the (real or imaginary) part of the support constrained Fourier spectrum. It was shown that this algorithm converges, but the point of minimum noise is achieved for a finite number of iterations if both the real and the imaginary parts of the measured Fourier data are noisy, and iterating beyond that point increases the noise in the image. It was also shown that constraining the support constrained Fourier data to remain with specified bounds of the measured data results in the comparable or higher noise levels in the final image than the original algorithm when the algorithm is stopped at the point of minimum noise. This is due to the fact that measured data will always have data points outside the $\pm 1\sigma$ (or 2σ, 3σ, etc.) regions centered on the true values. Thus, requiring the support constrained Fourier data to stay close to the measured data can result in mitigating the variance reduction achievable by support constraints. Because the noise is assumed to be wide sense stationary, the support constraint is required to have asymmetry and the noises corrupting the real and imaginary parts of the measured Fourier data must be sufficiently dissimilar for noise reduction inside the support constraint to be achieved.

A key result from this work is that enforcing support constraints can result in higher noise levels inside the support constraint than before the constraints were applied if the algorithm is continued until convergence is obtained. Another key result is that the point of minimum noise in the image domain is always reached before convergence (for noisy Fourier data). This appears to be a fundamental property of noisy data. As a result, the convex projections method should be used with caution. This is because the convex set which results from keeping the support constrained Fourier spectrum within a region about the mean of the measured Fourier spectrum does not intersect the convex set which results from applying a support constraint in the image domain, in general. Although the set in the Fourier domain can be made large enough to intersect the support convex set, doing this will usually result in a set so large that there is no change inside the support constraint resulting from applying support constraints. A better approach than this is to use the algorithm proposed in this paper.

Acknowledgments

This research was funded by a grant from the U.S. Air Force Office of Scientific Research, AFOSR/NM, Bolling Air Force Base, Washington, D.C. The research was also supported by the Advanced Imaging Division, Air Force Phillips Laboratory, Kirtland Air Force Base, New Mexico.

References

1. G. Demoment, "Image reconstruction and restoration: overview of common estimation structures and problems," IEEE Trans.Acoust., Speech, Signal Processing, vol.37, pp.2024-2036 (1989)
2. M.I. Sezan and A.M. Tekalp, "Survey of recent developments in digital image restoration," Opt.Eng., vol.29, pp.393-404 (1990)
3. H. Stark, editor, Image Recovery: Theory and Application, Academic Press, Orlando, FL (1987)
4. D.C. Youla, "Generalized image restoration by the method of alternating projections," IEEE Trans. Circuits Syst., vol. CAS-25, (1978)
5. D.C. Youla and H. Webb, "Image restoration by the method of convex projections: Part 1 - Theory," IEEE Trans. Medical Imaging, vol. M1-1, pp.81-94 (1982)
6. M.I. Sezan and H. Stark, "Image restoration by the method of convex projections: Part 2- Applications and numerical results," IEEE Trans. Medical Imaging, vol. M1-1, pp.95-101 (1982)
7. C.L. Matson, "Fourier spectrum extrapolation and enhancement using support constraints," to appear in IEEE Trans.Signal Processing
8. H.J. Trussell and M.R. Civanlar, "The feasible solution in signal restoration," IEEE Trans.Acoust., Speech, and Signal Processing, vol.32, pp.201-212 (1984)
9. M.R. Civanlar and H.J. Trussell, "Digital signal restoration using fuzzy sets," IEEE Trans.Acoust., Speech, and Signal Processing, vol.34, pp.919-936 (1986)

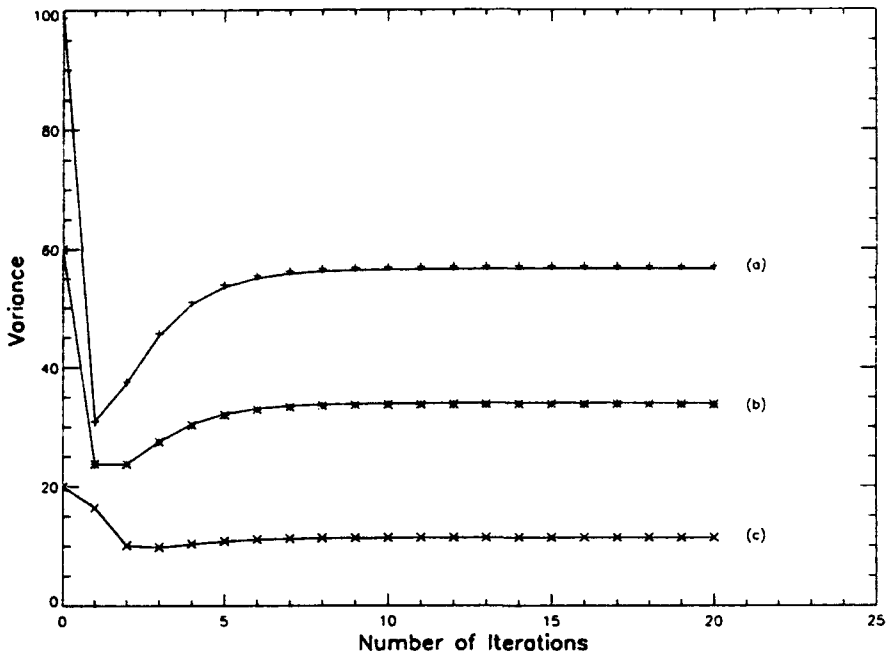

Fig.1. Variance of individual elements of the real part of the support constrained Fourier spectrum as a function of the number of iterations for (a) $\sigma_r^2/\sigma_i^2 = 1$, (b) $\sigma_r^2/\sigma_i^2 = 0.6$, and (c) $\sigma_r^2/\sigma_i^2 = 0.2$. The solid lines are theoretical predictions and the symbols represent simulation data points.

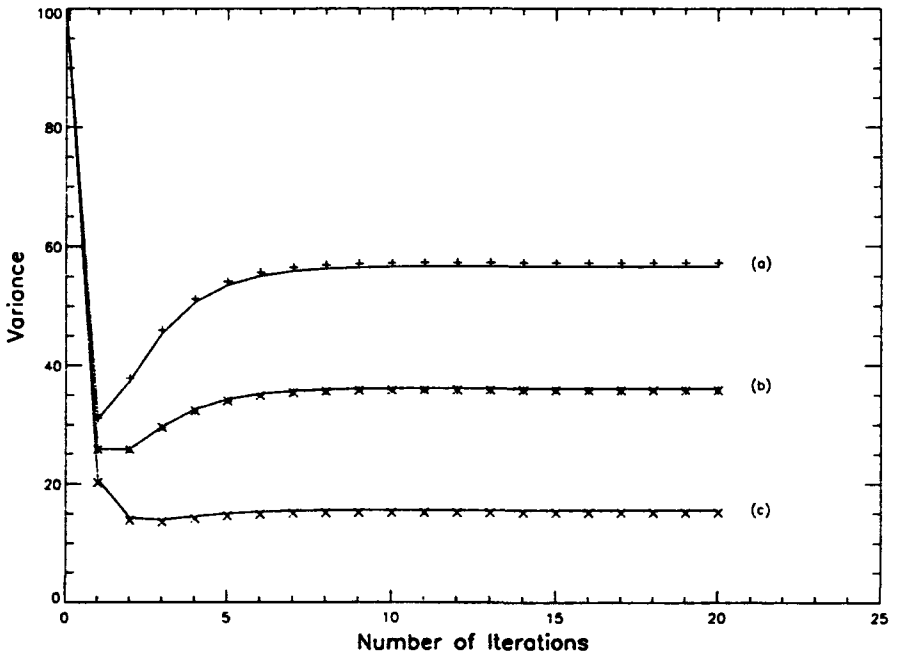

Fig.2. Variance of individual elements of the imaginary part of the support constrained Fourier spectrum as a function of the number of iterations for (a) $\sigma_r^2/\sigma_i^2 = 1$, (b) $\sigma_r^2/\sigma_i^2 = 0.6$, and (c) $\sigma_r^2/\sigma_i^2 = 0.2$. The solid lines are theoretical predictions and the symbols represent simulation data points.

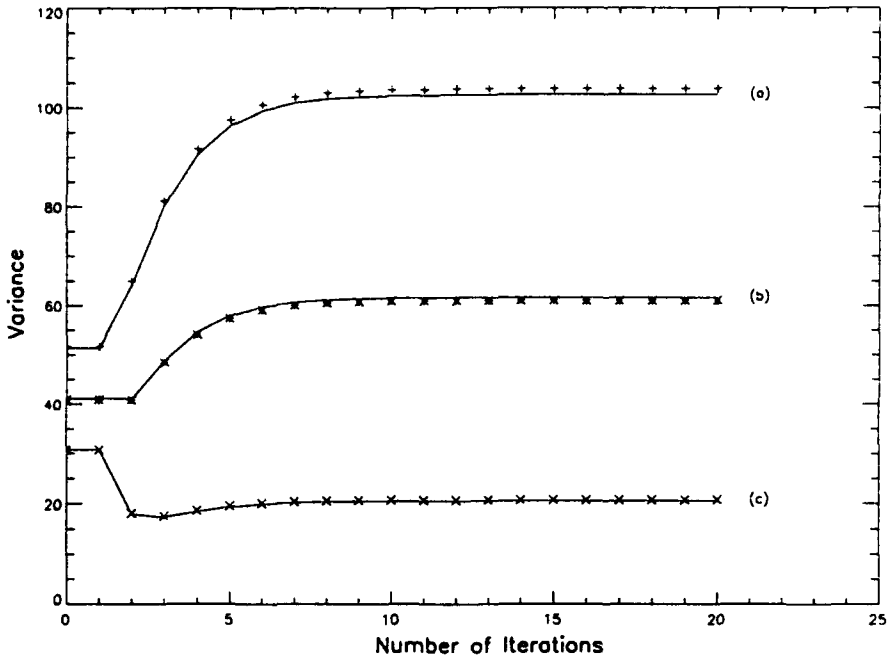

Fig.3. Total variance in the asymmetric region of the support constraint as a function of the number of iterations for (a) $\sigma_r^2/\sigma_i^2 = 1$, (b) $\sigma_r^2/\sigma_i^2 = 0.6$, and (c) $\sigma_r^2/\sigma_i^2 = 0.2$. The solid lines are theoretical predictions and the symbols represent simulation data points.

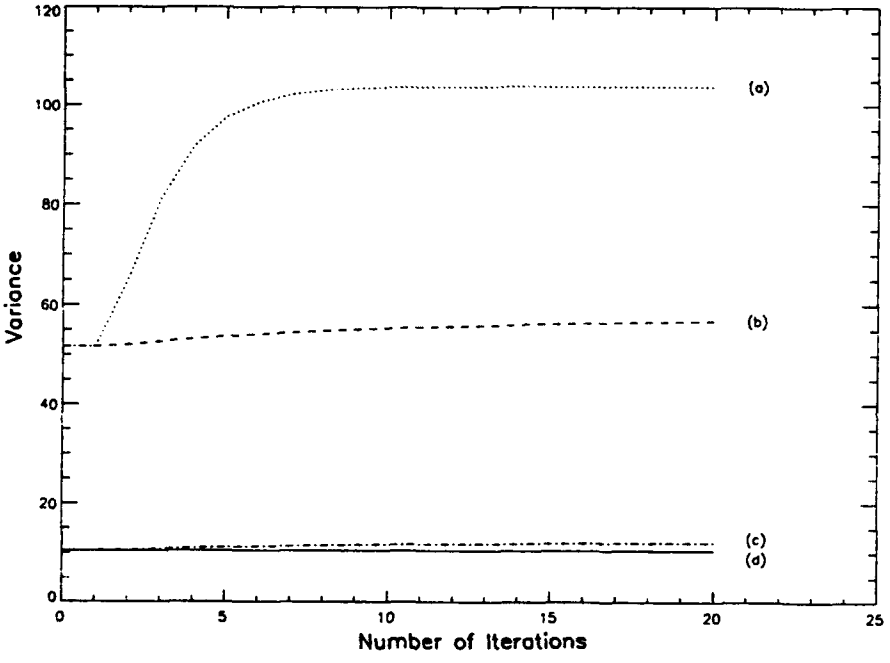

Fig.4. Variances for $\sigma_r^2/\sigma_i^2 = 1$ as a function of the iteration number. Curves (a) and (b) are the total variances in the asymmetric region of the support constraint for the original algorithm and the modified algorithm, respectively. Curves (c) and (d) are the total variances in the symmetric region of the support constraint for the modified algorithm and the original algorithm, respectively.

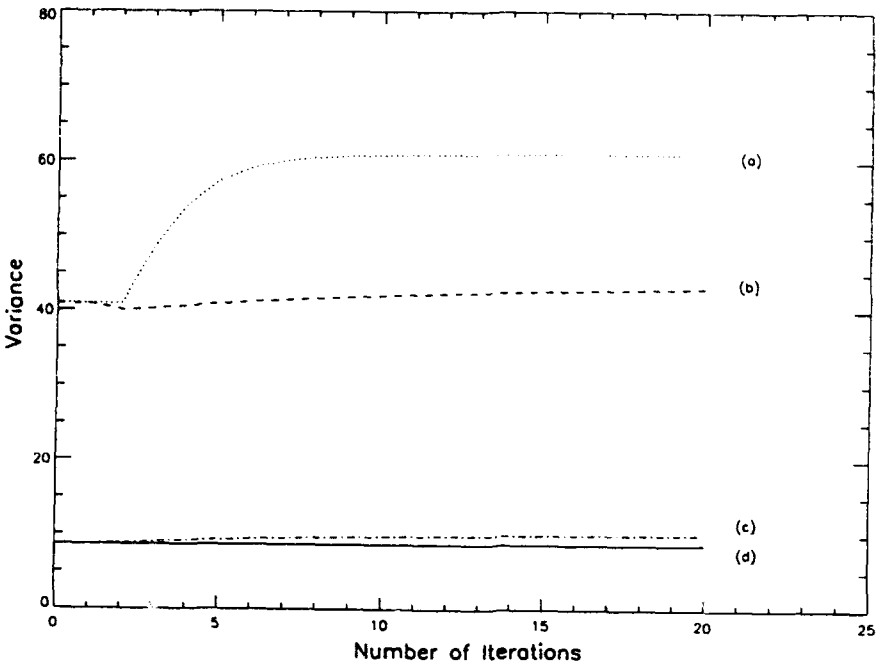

Fig.5. Variances for $\sigma_r^2/\sigma_i^2 = 0.6$ as a function of the iteration number. Curves (a) and (b) are the total variances in the asymmetric region of the support constraint for the original algorithm and the modified algorithm, respectively. Curves (c) and (d) are the total variances in the symmetric region of the support constraint for the modified algorithm and the original algorithm, respectively.

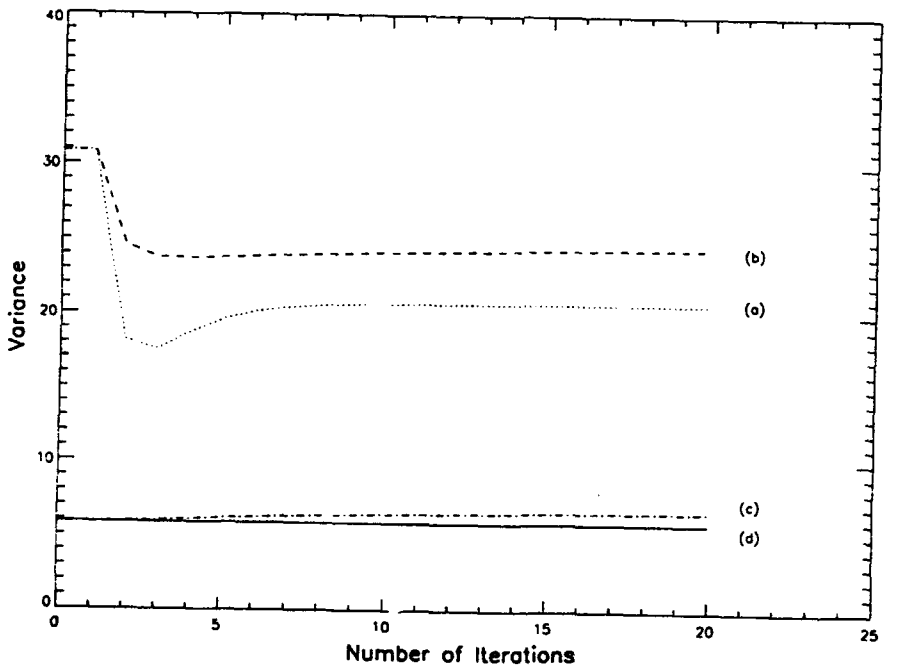

Fig.6. Variances for $\sigma_r^2/\sigma_i^2 = 0.2$ as a function of the iteration number. Curves (a) and (b) are the total variances in the asymmetric region of the support constraint for the original algorithm and the modified algorithm, respectively. Curves (c) and (d) are the total variances in the symmetric region of the support constraint for the modified algorithm and the original algorithm, respectively.

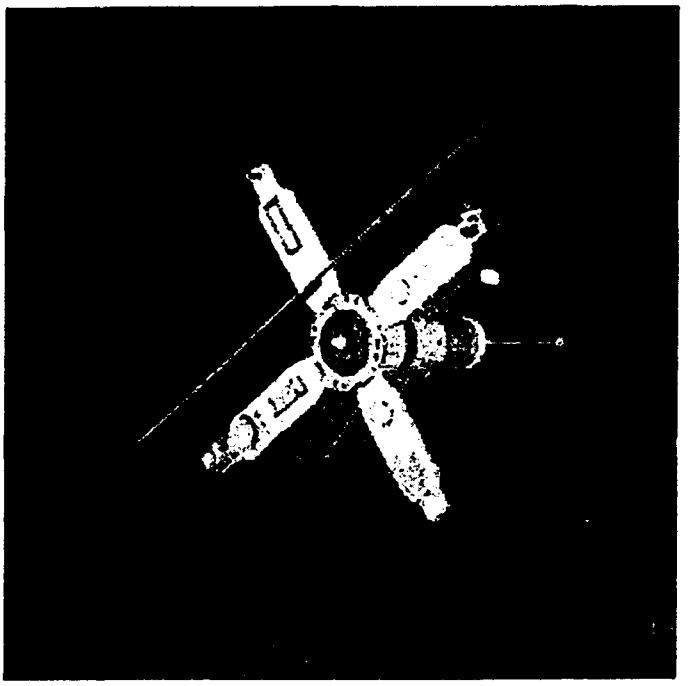

Fig.7. Uncorrupted satellite image.

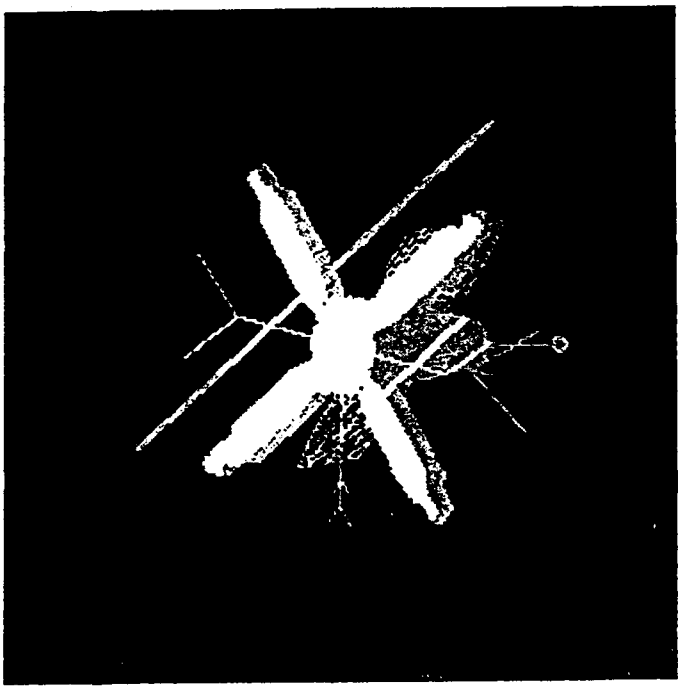

Fig.8. Support region of satellite image in Fig.7. The symmetric part of the support is shown in white, while the asymmetric part is shown in gray.

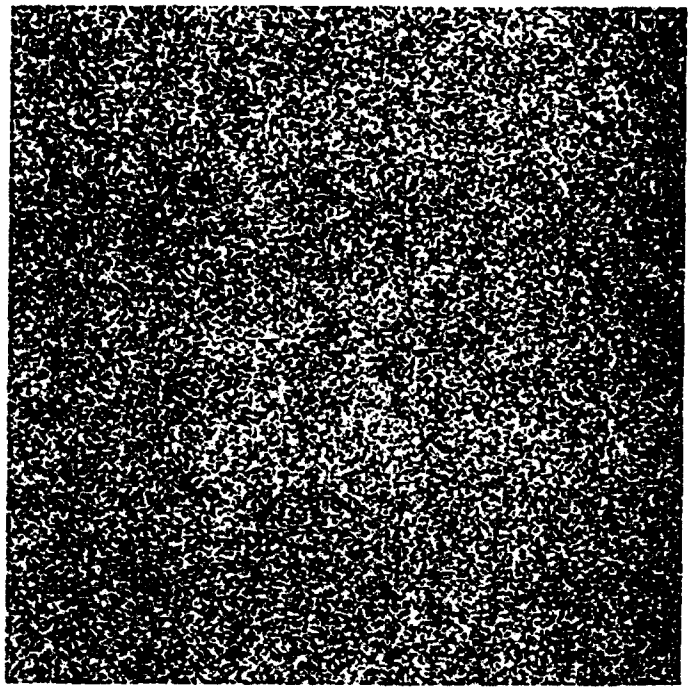

Fig.9. Noise corrupted satellite image for $\sigma_i^2=10^7$ times the dc value of the image and $\sigma_r^2=0.0$.

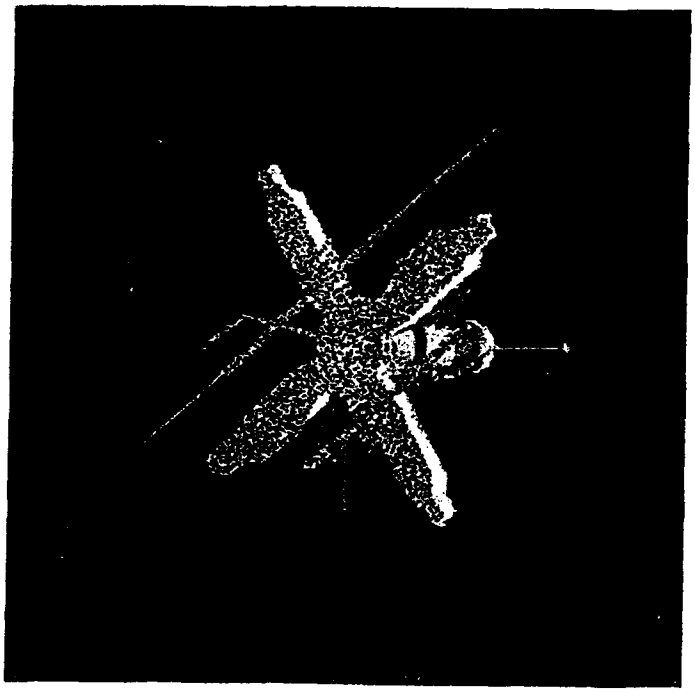

Fig.10. Reconstructed satellite image after 20 iterations of the original algorithm.

APPENDIX C

Positivity and its role in error reduction in images

Charles L. Matson
Phillips Laboratory/LIMI, Kirtland AFB, NM 87117
(505) 846-2049 (voice)
(505) 846-2045 (fax)
matson@plk.af.mil (email)

Abstract

In this paper, the role positivity plays in error reduction in images is analyzed both theoretically and with computer simulations for the case of wide-sense stationary Fourier domain noise. It is shown that positivity behaves as a signal- and noise-dependent support constraint. As a result, the mechanism by which positivity results in noise reduction in images is by correlating measured Fourier spectra. Noise reduction occurs in the asymmetric part of the positivity-induced support constraint when positivity is applied just as noise reduction occurs in the asymmetric part of the true support constraint when support is applied. In addition, the positivity-induced support constraint changes size, in general, for each iteration of the algorithm.

1. Introduction

Noise reduction in images with the use of knowledge in addition to the measured data has received much attention over the years[1-3]. Recently, a detailed analysis of how support functions as a constraint to reduce noise inside the support constraint has been completed[4,5]. It has been shown that, for wide-sense stationary Fourier domain noise, support constraints can be used to reduce the noise inside the support constraint if the ratio of the real and imaginary Fourier data variances is sufficiently small or large. It has also been shown that support, for this type of noise, does not result in noise reduction in the symmetric part of the support constraint, only in the asymmetric part.

In this paper, the same approach as in Ref.5 is taken to analyze positivity as a constraint for Fourier domain wide-sense stationary noise. It is shown that positivity acts as a signal- and noise-dependent support constraint. Inside the asymmetric part of the positivity-induced support constraint, noise reduction is possible just as when using support as a constraint. Inside the symmetric part of the positivity-induced support constraint, no noise reduction is possible just as when using support as a constraint. In addition, noise reduction inside the object's support using positivity is greater than when using the true support constraint in the high-noise environment. The paper is organized as follows: Section 2 contains the theoretical development, Section 3 contains the computer simulation results, and Section 4 contains the conclusions.

2. Theory

Let o(x) be the uncorrupted image and let i(x) be the measured image. Then i(x) is given by

$$i(x) = o(x) + n(x) \tag{1}$$

where n(x) is the inverse Fourier transform of zero-mean wide-sense stationary noise ($N_r(u)$,$N_i(u)$) whose second moments satisfy

$$\begin{aligned} \langle N_r(u_1)N_r(u_2)\rangle &= R_r(u_1-u_2)+R_r(u_1+u_2) \\ \langle N_i(u_1)N_i(u_2)\rangle &= R_i(u_1-u_2)-R_i(u_1+u_2) \\ \langle N_i(u_1)N_r(u_2)\rangle &= \langle N_r(u_1)N_i(u_2)\rangle = 0 \end{aligned} \tag{2}$$

where the terms involving sums of spatial frequencies will be neglected since they only have an impact near dc. This noise model is sufficiently general to accurately characterize CCD read noise and photon noise. Assume also that the data was measured in the Fourier domain so that there exists both the measured data I(u), the Fourier transform of i(x), and its variance, var{I(u)}, at each frequency.

Next, an algorithm must be chosen which will be used to enforce positivity as a constraint while requiring I(u) to remain close to the measured Fourier data in some sense in terms of var{I(u)}. Because the noise in the Fourier domain is wide-sense stationary, the variance of both the real and the imaginary parts of I(u) will be independent of frequency. Both because of ease of analysis and because it has performance comparable to or better than a standard convex projections[6-8] algorithm when using support as the image domain constraint for wide-sense stationary noise, the following algorithm[5] will be used. Starting in the image domain and assuming that the variance of the real part of I(u) is less than or equal to the variance of the imaginary part of I(u), (1) zero out all negative values of i(x), (2) Fourier transform i(x), (3) replace the real part of the positivity-constrained Fourier spectrum with the real part of the measured data, (4) inverse Fourier transform, and (5) start over with step 1 as long as the noise has not been minimized yet. In Ref.5, it is shown that the minimum noise achieved inside the support constraint occurs before the algorithm converges. However, this is not the case for positivity, in general.

In step one of the algorithm, the locations in which i(x) is zeroed out form a signal- and noise-dependent support constraint. In general, with each additional iteration of the algorithm, the signal-dependent support constraint will change. As a result, the first step in analyzing the algorithm's performance is to determine how the support changes on each iteration. Let $w_1(x)$ be the support constraint obtained during the first iteration of the algorithm as a result of the zeroes that exist in i(x) and the zeroes that result from enforcing the positivity constraint. Furthermore, let $i_1(x)$ be the image at the end of the first iteration, which is given by

$$i_1(x)=\frac{1}{2}[i(x)+i(-x)]+\frac{1}{2}[w_1(x)i(x)-w_1(-x)i(-x)] \tag{3}$$

where the first bracketed term is the inverse Fourier transform of the real part of I(u) and the second bracketed term is the inverse Fourier transform of the imaginary part of $I_1(u)$, the Fourier transform of $i_1(x)$. To determine the new signal-dependent support constraint to be used for the second iteration, $w_2(x)$, obtained by imposing positivity upon $i_1(x)$, it is useful to separate the image domain into four non overlapping regions: (1) $w_1(x)=w_1(-x)=1$, (2) $w_1(x)=w_1(-x)=0$, (3) $w_1(x)=0$ and $w_1(-x)=1$, and (4) $w_1(x)=1$ and $w_1(-x)=0$.

Region 1 after one iteration: because $w_1(x)=w_1(-x)=1$, Eq.(3) becomes

$$\begin{aligned} i_1(x)&=\frac{1}{2}[i(x)+i(-x)]+\frac{1}{2}[i(x)-i(-x)] \\ &=i(x) \end{aligned} \tag{4}$$

Since $w_1(x)=1$, i(x) is nonnegative and thus $w_2(x)=w_1(x)=1$. This means that once points in the image domain are in region 1, they stay there.

Region 2 after one iteration: because $w_1(x)=w_1(-x)=0$, Eq.(3) becomes

$$i_1(x)=\frac{1}{2}[i(x)+i(-x)] \tag{5}$$

Because $w_1(x)=w_1(-x)=0$, both i(x) and i(-x) are either zero or negative. Thus it follows that $i_1(x)\le 0$ and thus $w_2(x)=w_1(x)=0$. As for region 1, once points are in region 2, they never leave.

Region 3 after one iteration: because $w_1(x)=0$ and $w_1(-x)=1$, Eq.(3) becomes

$$\begin{aligned} i_1(x)&=\frac{1}{2}[i(x)+i(-x)]-\frac{1}{2}i(-x) \\ &=\frac{1}{2}i(x) \end{aligned} \tag{6}$$

Since $w_1(x)=0$, $i(x)\le 0$, and thus $w_2(x)=w_1(x)=0$. Furthermore, once a point's support function becomes zero, it stays zero. However, region 3 will change in size since region 4 changes in size, as shown next.

Region 4 after one iteration: because $w_1(x)=1$ and $w_1(-x)=0$, Eq.(3) becomes

$$\begin{aligned} i_1(x)&=\frac{1}{2}[i(x)+i(-x)]+\frac{1}{2}i(x) \\ &=i(x)+\frac{1}{2}i(-x) \end{aligned} \tag{7}$$

In this region, $i_1(x)$ could be either positive or negative, depending upon the relative size of i(x) and i(-x). If $i_1(x)>0$, then $w_2(x)=w_1(x)=1$. If, however, $i_1(x)\le 0$, then $w_2(x)=0$. Thus this point would move from region 4 into region 2. Thus, it can be seen that after one iteration, the support size has not increased in size and probably has decreased in size.

Following the same steps as above, it can be shown that, after n iterations, $i_n(x)$ is given by

$$i_n(x) = \frac{1}{2}[i(x) + i(-x)] + \frac{1}{2}[w_n(x)i_{n-1}(x) - w_n(-x)i_{n-1}(-x)] \tag{8}$$

where $i_{n-1}(x)$ depends upon the region it is in. In addition to finding $i_n(x)$, it is necessary to find the sizes of the regions and total mean square error (MSE) in the regions to determine how positivity is affecting the noise characteristics of the iterated data.

Region 1 after n iterations: because $w_n(x)=w_n(-x)=1$, Eq.(8) becomes

$$\begin{aligned} i_n(x) &= \frac{1}{2}[i(x) + i(-x)] + \frac{1}{2}[i(x) - i(-x)] \\ &= i(x) \end{aligned} \tag{9}$$

So, after n iterations, region 1 remains unchanged in size and the image remains unchanged. The size of region 1 can be found by multiplying the area of the image by the joint probability that i(x)>0 and i(-x)>0, which is given by

$$\begin{aligned} P\{i(x) > 0 \text{ and } i(-x) > 0\} &= P\{o(x) + n(x) > 0 \text{ and } o(-x) + n(-x) > 0\} \\ &= P\{n(x) > -o(x) \text{ and } n(-x) > -o(-x)\} \end{aligned} \tag{10}$$

In addition, the mean square error (MSE) in the region is given by

$$MSE_{\text{region 1}} = \sum_{\text{region 1}}[i(x) - o(x)]^2 = \sum_{\text{region 1}} E\{n^2(x) | n(x) > -o(x) \text{ and } n(-x) > -o(-x)\} \tag{11}$$

Notice that both the size of region 1 and the error in region 1 are unaffected by the application of positivity and thus are independent of the number of iterations. This is the same as for support constraints[5].

Region 2 after n iterations: because $w_n(x)=w_n(-x)=0$, Eq.(8) becomes

$$i_n(x) = \frac{1}{2}[i(x) + i(-x)] \tag{12}$$

The elements in this region that were in this region after one iteration are still here, since positivity is not changing the value of $i_n(x)$. As discussed above, points from region 4 can migrate in here. However, once the points make it in here, they stay here. The size of the region is found by multiplying the area of the image by the probability of being in this region which is given by

$$\begin{aligned} P\{w_n(x) = 0 \text{ and } w_n(-x) = 0\} &= P\{w(x) = 0 \text{ and } w(-x) = 0\} \\ &\quad + P\{\text{points from region 4 moving to region 2 after n iterations}\} \\ &= P\{n(x) \le -o(x) \text{ and } n(-x) \le -o(-x)\} + [P_{4(0)} - P_{4(n)}] \end{aligned} \tag{13}$$

where $P_{4(n)}$ is the probability that a point is in region 4 at the n^{th} iteration. The MSE in this region is given by

$$MSE_{\text{region 2(n)}} = \sum_{\text{region 2(n)}} o^2(x) \tag{14}$$

and changes, in general, on each iteration.

Region 3 after n iterations: because $w_n(x)=0$ and $w_n(-x)=1$, Eq.(8) becomes

$$i_n(x)=\frac{1}{2^n}i(x) \tag{15}$$

and this region is decreasing in size since region 4 is. The probability that a point is in this region after n iterations is given by

$$\begin{aligned} P\{w_n(x)=0 \text{ and } w_n(-x)=1\} &= P\{w(x)=0 \text{ and } w(-x)=1\} \\ &\quad -P\{\text{points from region 4 moving to region 2 after n iterations}\} \\ &= P\{n(x)\le -o(x) \text{ and } n(-x)\ge -o(-x)\}-\left[P_{4(0)}-P_{4(n)}\right] \end{aligned} \tag{16}$$

and the total MSE in this region after n iterations is given by

$$MSE_{\text{region 3(n)}}=\sum_{\text{region 3(n)}} o^2(x) \tag{17}$$

Region 4 after n iterations: because $w_n(x)=1$ and $w_n(-x)=0$, Eq.(8) becomes

$$i_n(x)=i(x)+i(-x)\sum_{k=1}^{n}\frac{1}{2^k} \tag{18}$$

As for the previous regions, the size of this region is equal to the area of the image times the probability that a point is in this region which is given by

$$\begin{aligned} P\{w_n(x)=1 \text{ and } w_n(-x)=0\} &= P\{i_n(x)>0 \text{ and } i_n(-x)\le 0\} \\ &= P\left\{n(x)+n(-x)\sum_{k=1}^{n}\frac{1}{2^k}>-o(x)-o(-x)\sum_{k=1}^{n}\frac{1}{2^k} \text{ and } n(-x)\le -o(-x)\right\} \end{aligned} \tag{19}$$

and the MSE in this region after n iterations is given by

$$\begin{aligned} MSE_{\text{region 1}} &= \sum_{\text{region 1}}\left[i_n(x)-o(x)\right]^2 \\ &= \sum_{\text{region 1}} E\left\{\left[n(x)+\left[n(-x)+o(-x)\right]\sum_{k=1}^{n}\frac{1}{2^k}\right]^2 \;\middle|\; w_n(x)=1 \text{ and } w_n(-x)=0\right\} \end{aligned} \tag{20}$$

All the above equations assumed that the real part of the noise was less noise than the imaginary, and so the real part of the iterated Fourier data was constrained to match the measured data, while the imaginary part was left totally unconstrained. If the imaginary part is less noisy than the real part of the measured Fourier data, the imaginary would be constrained and the real would be left totally unconstrained. Because the positivity constraint dramatically alters the dc value of the image, the algorithm which constrains just the imaginary can allow large errors to occur. As a result, when the imaginary is less noisy than the real, all the imaginary values of the iterated

data are constrained to match the measured data; but, in addition, the dc value of the iterated data is constrained to stay within $\pm 2\sigma$ of the measured dc value. This modification of the algorithm makes theoretical predictions difficult since the algorithm has become nonlinear. Therefore, for this case only computer simulations will be run.

Summarizing, positivity behaves as a signal- and noise-dependent support constraint which changes, in general, on each iteration. No noise reduction occurs in the region of the symmetric positivity-enforced support, and the only noise reduction that occurs outside the positivity-enforced constraint results from zeroing out negative numbers. Effectively, the noise changes that occur inside the object's true support occur in the asymmetric part of the positivity-constrained support, both because noise values change on each iteration and also because the size of the positivity-enforced asymmetric support changes in size. Thus, the role positivity plays in error reduction is very much like support constraints, where correlation of Fourier spectra bring about noise changes in the asymmetric part of the support constraint. The major difference between positivity and support is that positivity-enforced support constraints can change each iteration, while support constraints do not.

3. Computer simulation results

In this section, computer simulation results are presented both to validate the theoretical results presented in Section 2 and to show graphically the effect positivity has on noise properties. Because probabilities and expected values must be calculated for sums of random variables, the noise corrupting the image was chosen to be the sum of two gaussian stochastic processes $n_e(x)$ and $n_o(x)$ which satisfy

$$\begin{aligned} \langle n_e(x_1)n_e(x_2)\rangle &= \sigma_e^2\delta(x_1-x_2)+\sigma_e^2\delta(x_1+x_2) \\ \langle n_o(x_1)n_o(x_2)\rangle &= \sigma_o^2\delta(x_1-x_2)-\sigma_o^2\delta(x_1+x_2) \\ \langle n_e(x_1)n_o(x_2)\rangle &= 0 \end{aligned} \tag{21}$$

in order to make calculations tractable. This form of image domain noise results in Fourier-domain noise which is effectively wide-sense stationary except at dc. If σ_e^2 is less than σ_o^2, the real part of the Fourier data is less noisy than the imaginary, and vice versa. In addition, since the statistical quantities are dependent upon o(x), for simplicity o(x) was chosen to be constant inside a triangular support region and zero outside.

The first computer simulations used an image with an average SNR of 0.5 inside the object's true support. In Figures 1 and 2, normalized mean square error plots inside the object's true support constraint are shown for the asymmetric and symmetric support regions, respectively, and $\sigma_e^2/\sigma_o^2 = 0.1$. In Figures 3 and 4, the same plots are shown for all the same values except $\sigma_e^2/\sigma_o^2 = 10$. In each figure, the MSE for a positivity constraint, support constraint, and both positivity and support are shown. For the support constraint MSE determination, at each iteration the image's negative values were zeroed before error calculations, but the negative numbers were restored before the next application of support constraints. This allowed a more fair comparison between the three types of constraints. For the positivity case, theoretical values determined from the results in Section 2 for $\sigma_e^2/\sigma_o^2 = 0.1$ are also shown. Notice that in the asymmetric region of the true support positivity, support, and both positivity and support all achieved approximately the same error reductions. However, in the symmetric region of the support positivity with and without support constraints resulted in lower values than for support alone (where no noise reduction occurred). This is due to negative image values inside the symmetric part of the true support constraint resulting in a noise-induced asymmetric support, which results in reduced MSE. Also notice that using both positivity and support as a constraint sometimes resulted in the same MSE plots as with just positivity or support alone, and other times it results in MSE plots which were in between the error plots resulting from using either support or positivity alone. Notice that the results are quite similar for both $\sigma_e^2/\sigma_o^2 = 0.1$ and $\sigma_e^2/\sigma_o^2 = 10$.

Next, the simulations were run for the same scenario as above except that the average SNR inside the object's true support was chosen to be 1. It can be seen from Figures 5-8 that positivity alone is becoming less effective as a constraint when compared to support or both support and positivity. Finally, computer simulations were run for an average SNR of 5. The results are in Figures 9-12, and it can be seen that positivity alone as a constraint is much less effective than support, and when positivity and support are both applied the results are

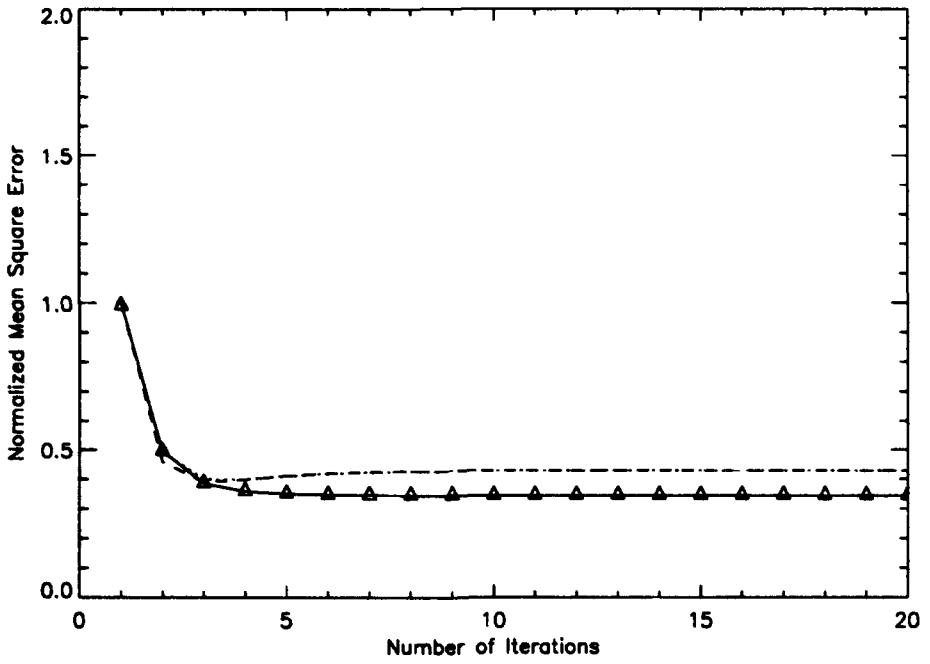

Figure 1. Normalized MSE inside asymmetric part of object's true support for SNR=0.5, σ_e^2 / σ_o^2 =0.1. The dotted line is for a support constraint, the dashed line is for both support and positivity, and the solid line is for positivity alone. The triangles denote theoretically calculated points for positivity constraint alone.

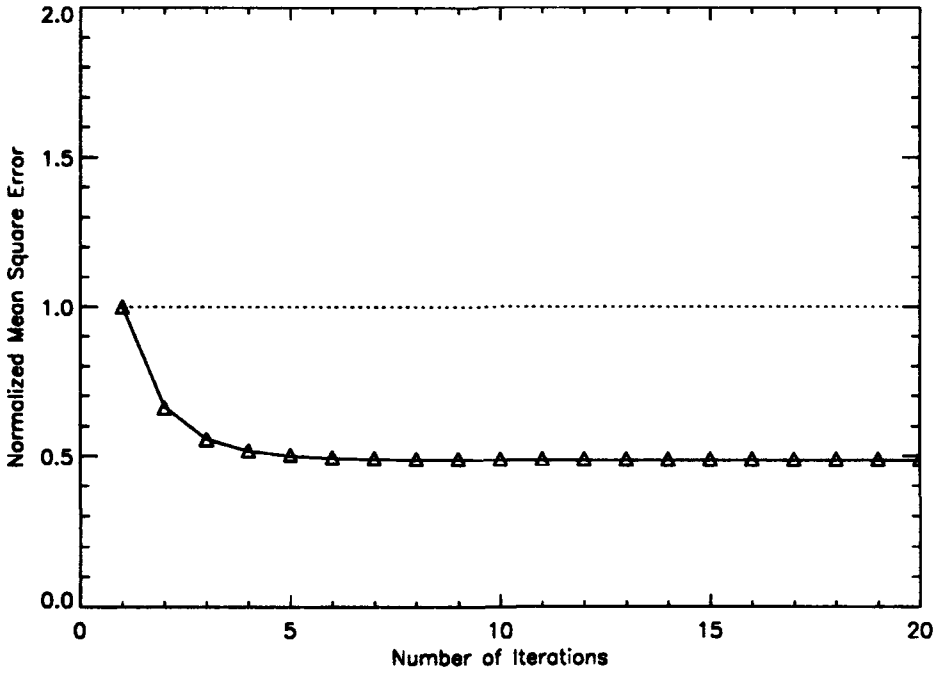

Figure 2. Normalized MSE inside symmetric part of object's true support for SNR=0.5, σ_e^2 / σ_o^2 =0.1. The dotted line is for a support constraint, the dashed line is for both support and positivity, and the solid line is for positivity alone. The triangles denote theoretically calculated points for positivity constraint alone.

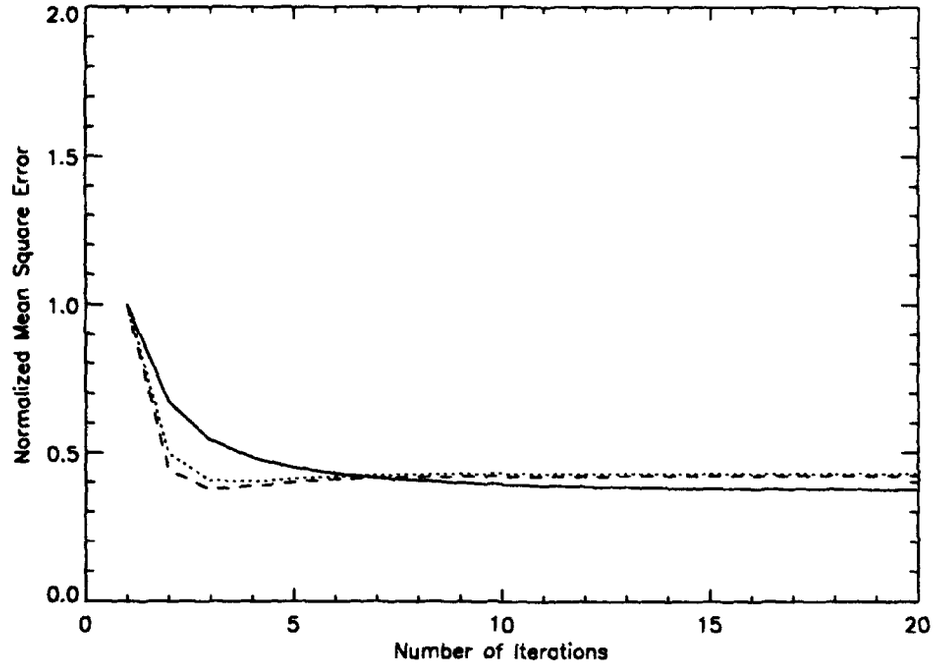

Figure 3. Normalized MSE inside asymmetric part of object's true support for SNR=0.5, σ_e^2 / σ_o^2 =10. The dotted line is for a support constraint, the dashed line is for both support and positivity, and the solid line is for positivity alone.

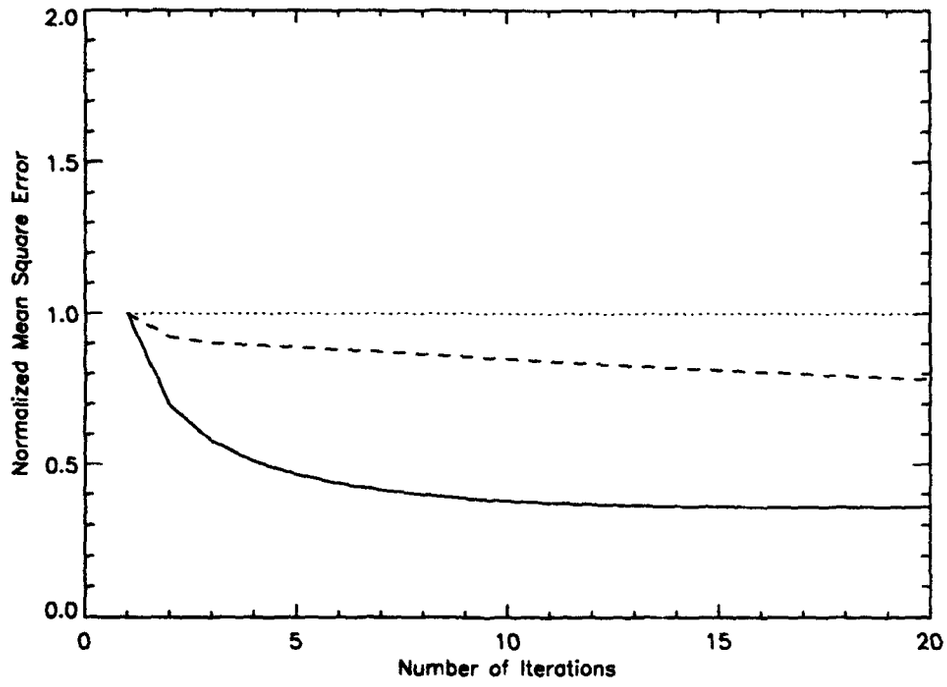

Figure 4. Normalized MSE inside symmetric part of object's true support for SNR=0.5, σ_e^2 / σ_o^2 =10. The dotted line is for a support constraint, the dashed line is for both support and positivity, and the solid line is for positivity alone.

indistinguishable from using support alone. This is as expected since, with higher SNRs, the noise rarely results in negative image values inside the true support, and so positivity has little impact on providing a support constraint.

4. Conclusions

An analysis has been provided which shows the effect that positivity has upon noise reduction in images for the case of wide-sense stationary Fourier domain noise. It has been shown theoretically and with the use of computer simulations that positivity as a constraint acts as a signal- and noise-dependent support constraint. There are two mechanisms by which positivity causes noise reduction inside the true support of the object. The first mechanism is noise reduction in the asymmetric part of the support constraint due to mismatches between the variances of the real and imaginary noises corrupting the Fourier spectra. The second mechanism is that of reducing the size of the positivity-enforced support constraint due to negative values in the image. Positivity has been shown to be most effective for images with SNRs less than one, and essentially ineffective for SNRs greater than five. The effect of positivity was compared to support via computer simulations, and it was shown that positivity and support had comparable effect in the asymmetric part of the support, but positivity did better in the symmetric part of the support for low SNRs and worse for high SNRs. Comparable results were obtained with positivity, on average, for $\sigma_e^2 / \sigma_o^2 < 1$ and $\sigma_e^2 / \sigma_o^2 > 1$.

Because positivity behaves as a signal- and noise-dependent support constraint, it follows that positivity works by enforcing correlations among Fourier spectra just as support does[4,5]. As a result, the noise correlation properties are key to determining how effective positivity will be as a constraint.

Acknowledgments

This research was funded by a grant from the U.S. Air Force Office of Scientific Research, Bolling Air Force Base, Washington, D.C.

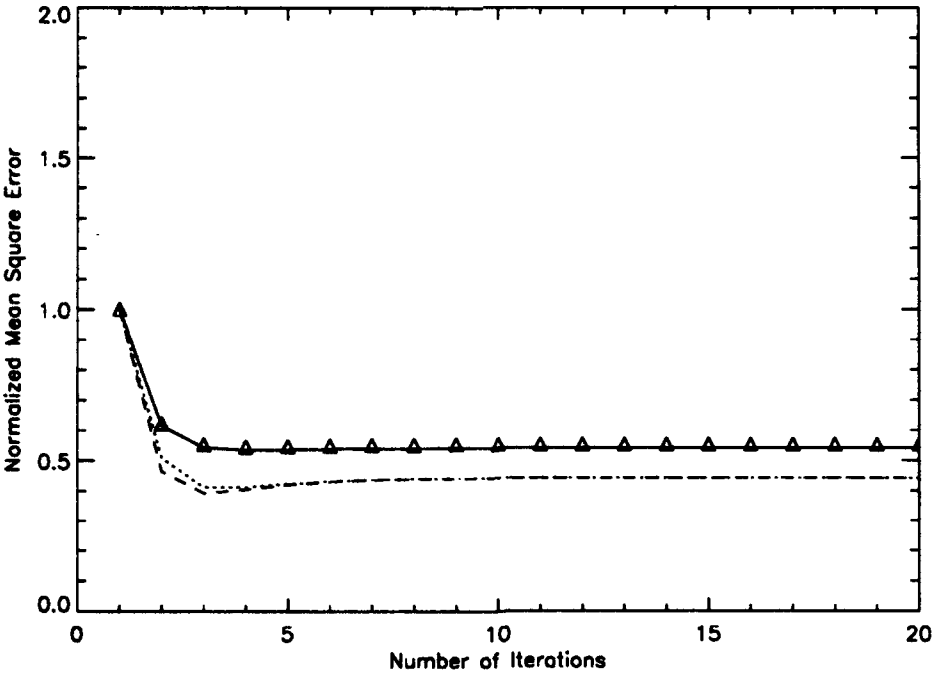

Figure 5. Normalized MSE inside asymmetric part of object's true support for SNR=1.0, σ_e^2 / σ_o^2 =0.1. The dotted line is for a support constraint, the dashed line is for both support and positivity, and the solid line is for positivity alone. The triangles denote theoretically calculated points for positivity constraint alone.

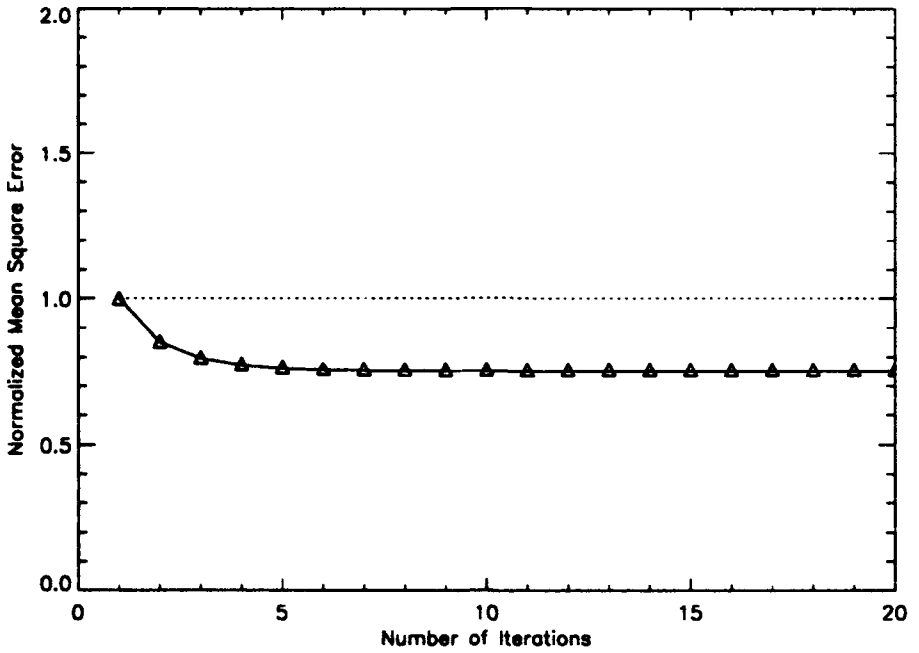

Figure 6. Normalized MSE inside symmetric part of object's true support for SNR=1.0, σ_e^2 / σ_o^2 =0.1. The dotted line is for a support constraint, the dashed line is for both support and positivity, and the solid line is for positivity alone. The triangles denote theoretically calculated points for positivity constraint alone.

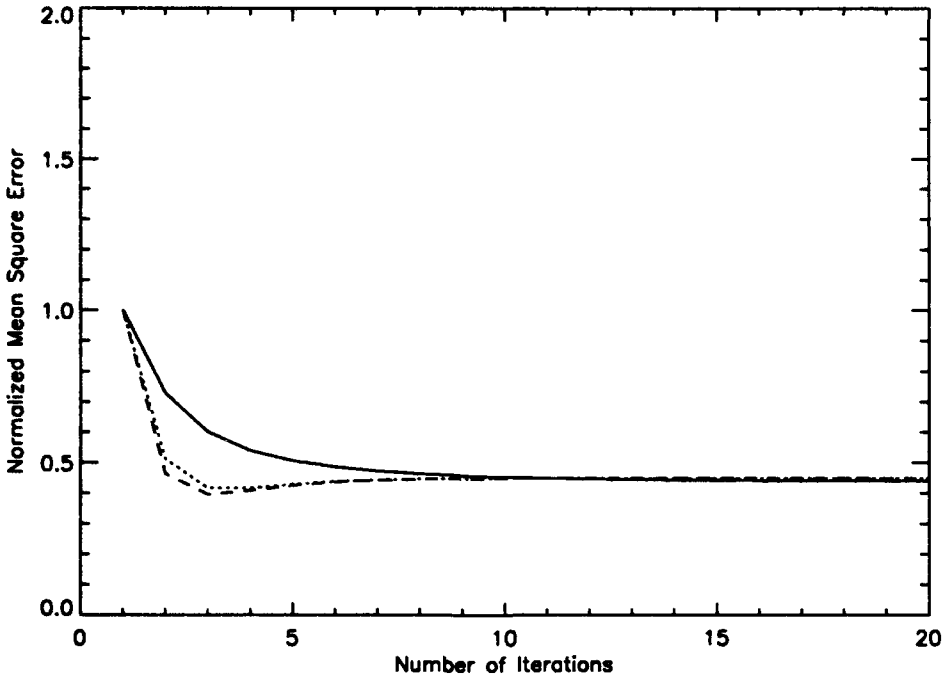

Figure 7. Normalized MSE inside asymmetric part of object's true support for SNR=1, σ_e^2 / σ_o^2 =10. The dotted line is for a support constraint, the dashed line is for both support and positivity, and the solid line is for positivity alone.

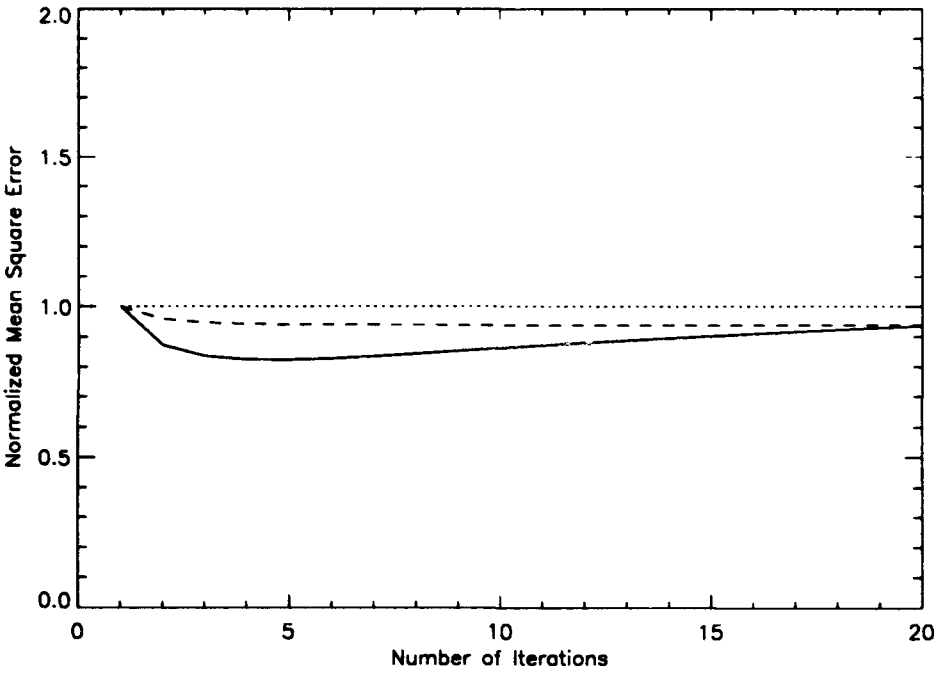

Figure 8. Normalized MSE inside symmetric part of object's true support for SNR=1, σ_e^2 / σ_o^2 =10. The dotted line is for a support constraint, the dashed line is for both support and positivity, and the solid line is for positivity alone.

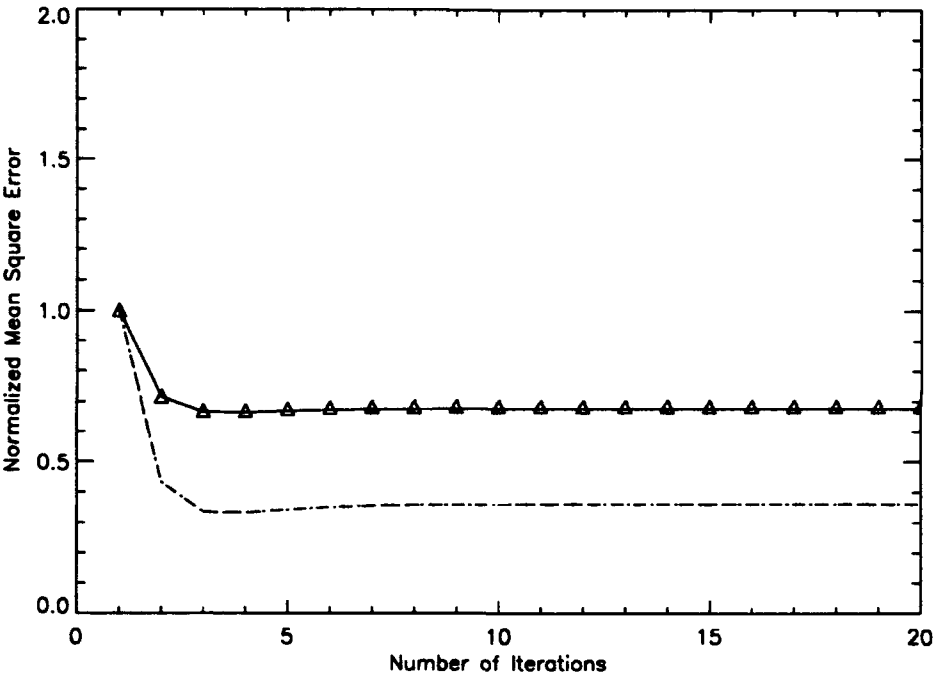

Figure 9. Normalized MSE inside asymmetric part of object's true support for SNR=5, σ_e^2 / σ_o^2 =0.1. The dotted line is for a support constraint, the dashed line is for both support and positivity, and the solid line is for positivity alone. The triangles denote theoretically calculated points for positivity constraint alone.

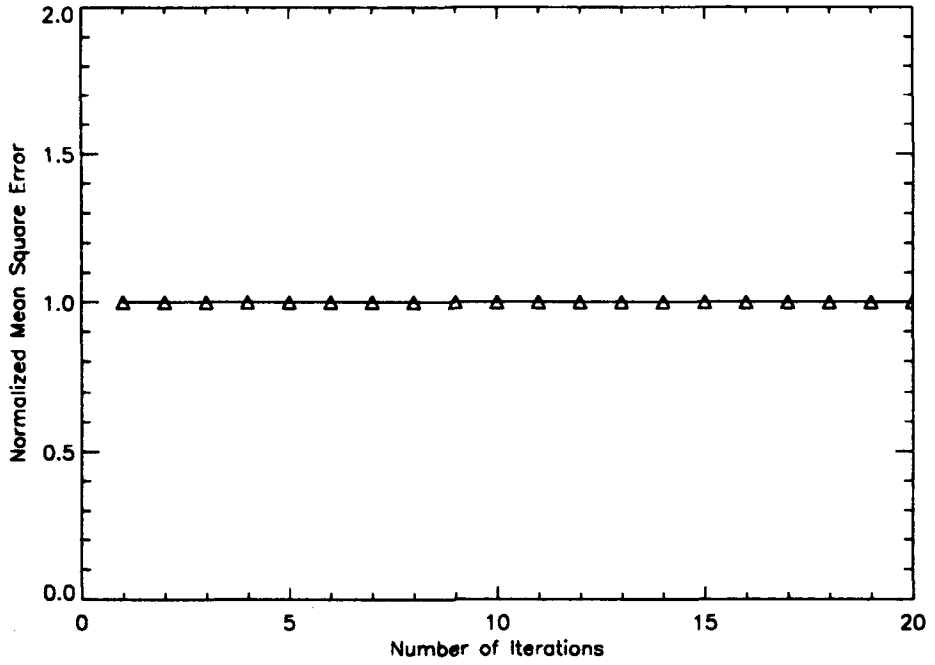

Figure 10. Normalized MSE inside symmetric part of object's true support for SNR=5, σ_e^2 / σ_o^2 =0.1. The dotted line is for a support constraint, the dashed line is for both support and positivity, and the solid line is for positivity alone. The triangles denote theoretically calculated points for positivity constraint alone.

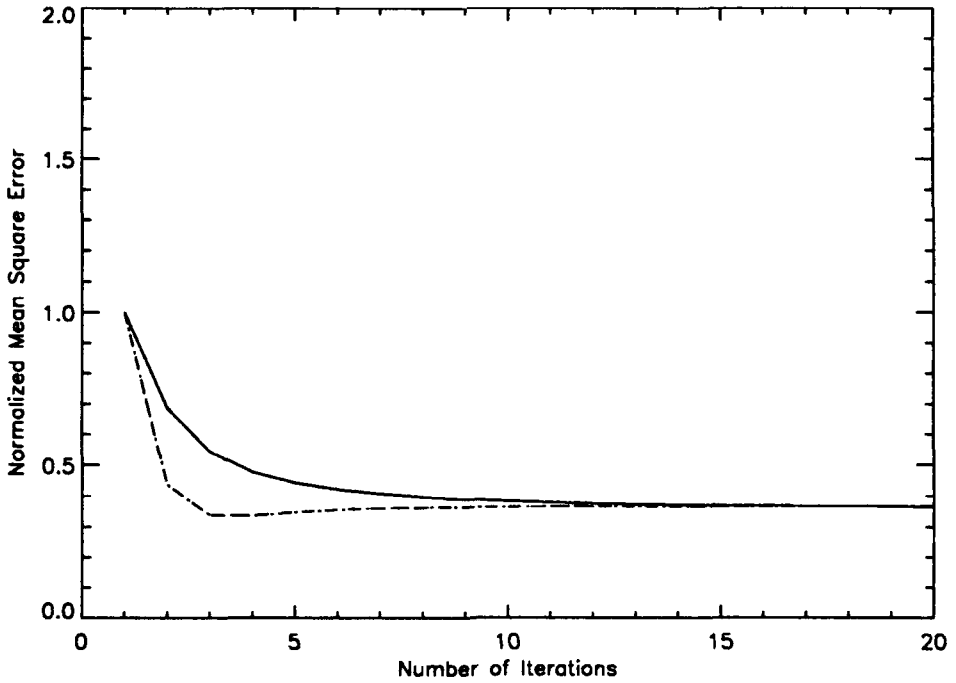

Figure 11. Normalized MSE inside asymmetric part of object's true support for SNR=5, σ_e^2 / σ_o^2 =10. The dotted line is for a support constraint, the dashed line is for both support and positivity, and the solid line is for positivity alone.

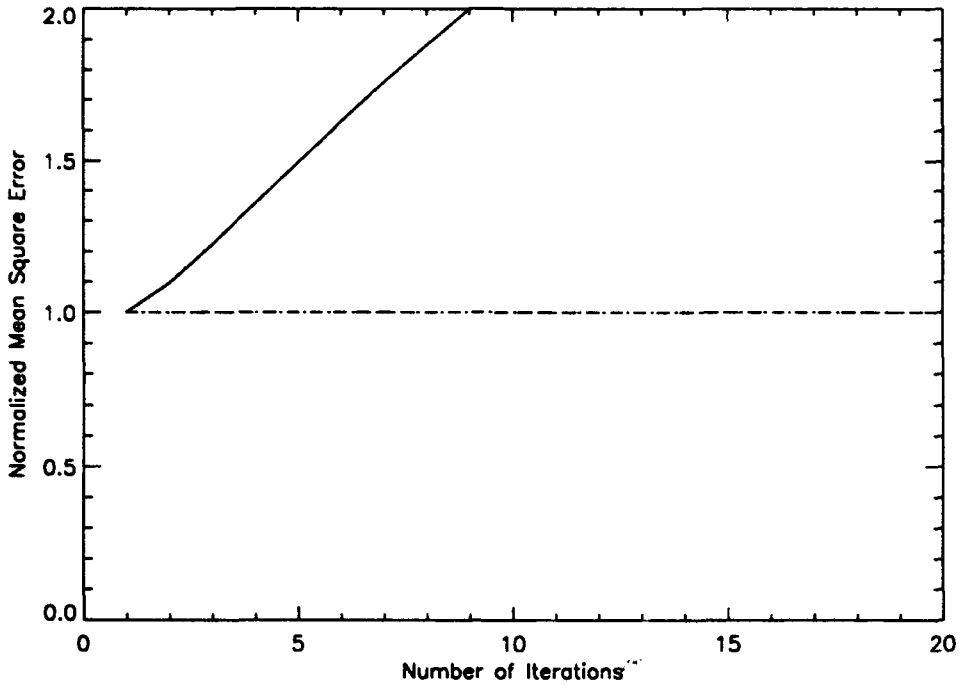

Figure 12. Normalized MSE inside symmetric part of object's true support for SNR=5, σ_e^2 / σ_o^2 =10. The dotted line is for a support constraint, the dashed line is for both support and positivity, and the solid line is for positivity alone.

References

1. G. Demoment, "Image reconstruction and restoration: overview of common estimation structures and problems," IEEE Trans.Acoust., Speech, Signal Processing, vol.37, pp.2024-2036 (1989)

2. M.I. Sezan and A.M. Tekalp, "Survey of recent developments in digital image restoration," Opt.Eng., vol.29, pp.393-404 (1990)

3. H. Stark, editor, *Image Recovery: Theory and Application*, Academic Press, Orlando, FL (1987)

4. C.L. Matson, "Fourier spectrum extrapolation and enhancement using support constraint," to appear in IEEE Trans. Signal Proc., January 1994

5. C.L. Matson, "Variance reduction in Fourier spectra and their corresponding images with the use of support constraints," to appear in J.Opt.Soc.Am.A., January 1994

6. D.C. Youla, "Generalized image restoration by the method of alternating projections," IEEE Trans. Circuits Syst., vol. CAS-25, (1978)

7. D.C. Youla and H. Webb, "Image restoration by the method of convex projections: Part 1 - Theory," IEEE Trans. Medical Imaging, vol. M1-1, pp.81-94 (1982)

8. M.I. Sezan and H. Stark, "Image restoration by the method of convex projections: Part 2- Applications and numerical results," IEEE Trans. Medical Imaging, vol. M1-1, pp.95-101 (1982)

APPENDIX D

Error reduction in images using high-quality prior knowledge

Charles L. Matson
Phillips Laboratory/LIMI, Kirtland AFB, NM 87117
(505) 846-2049 (voice)
(505) 846-2045 (fax)
matson@plk.af.mil (email)

Abstract

The use of information about an image in addition to measured data has been demonstrated to provide the possibility of decreasing the noise in the measured data. A new constraint, recently proposed, is that of perfect knowledge of part of an image. In this paper, these results are generalized and the usefulness of this new constraint to decrease noise outside the region of prior knowledge is shown to be a function of the measured data noise-correlation properties. In particular, it is shown that prior high-quality knowledge is a generalization of support constraints.

1. Introduction

The use of additional information for error reduction in images, either by superresolution or noise-reduction in measured data, has received much attention[1-6]. The types of additional information include information such as support regions, positivity, and energy constraints[3], as well as others. Recently, it has been proposed[7] that part of a image may be known exactly, and this can be used as a constraint to decrease noise levels in the image outside the region of perfectly known data. In this paper, the results in Ref.7 are generalized and made rigorous. It is shown that high-quality prior knowledge is a generalization of support constraints, and thus the ability to reduce noise levels in the image outside the region of high-quality data is a function of the statistical properties of the noise corrupting the image[6].

2. Theory

Let an estimated image be given by $o_e(x)$. Suppose that a region of this image is known, by some means such as earlier photographs or computer modeling, with much higher (but not necessarily perfect) accuracy. Let $o_p(x)$ denote this prior information, and let $w_p(x)$ be the binary support function defining this region. Furthermore, let $w_e(x)$ denote the binary support function for the complement of this region. Then the composite image $\hat{o}_e(x)$ can be formed as follows:

$$\hat{o}_e(x) = w_e(x)o_e(x) + w_p(x)o_p(x) \tag{1}$$

Assuming that measured Fourier data is available, along with an estimate of its variance, it is now necessary to determine the effect this prior knowledge has upon the quality of the constrained Fourier spectrum relative to the measured spectrum. Fourier transforming Eq.(1) gives

$$\hat{O}_e(u) = \int_{-\infty}^{\infty} W_e(\xi)O_e(u-\xi)d\xi + \int_{-\infty}^{\infty} W_p(\xi)O_p(u-\xi)d\xi$$

$$= \int_{-\infty}^{\infty} W_{er}(\xi)O_{er}(u-\xi)d\xi - \int_{-\infty}^{\infty} W_{ei}(\xi)O_{ei}(u-\xi)d\xi + j\left[\int_{-\infty}^{\infty} W_{er}(\xi)O_{ei}(u-\xi)d\xi + \int_{-\infty}^{\infty} W_{ei}(\xi)O_{er}(u-\xi)d\xi\right]$$

$$+ \int_{-\infty}^{\infty} W_{pr}(\xi)O_{pr}(u-\xi)d\xi - \int_{-\infty}^{\infty} W_{pi}(\xi)O_{pi}(u-\xi)d\xi + j\left[\int_{-\infty}^{\infty} W_{pr}(\xi)O_{pi}(u-\xi)d\xi + \int_{-\infty}^{\infty} W_{pi}(\xi)O_{pr}(u-\xi)d\xi\right] \tag{2}$$

where the subscripts r and i refer to the real and imaginary parts of a complex quantity, respectively, and capital letters denote Fourier transforms. To determine the change in quality of the constrained Fourier transform, it is necessary to calculate the variances of the real and imaginary parts of $\hat{O}_e(u)$, since algorithms using this constraint would seek to constrain the modified data to stay close to the measured data. This can be accomplished in a straightforward although tedious way. To simplify matters, assume that the noises corrupting the high-quality prior knowledge are uncorrelated with noises corrupting the measured data. Thus, cross-covariance terms are zero and we get

$$\text{var}\{\hat{O}_{er}(u)\} \equiv <[\hat{O}_{er}(u)]^2> - <\hat{O}_{er}(u)>^2$$

$$= \int_{-\infty}^{\infty}\int\left[W_{er}(\xi)W_{er}(\zeta)\text{covar}\left\{O_{er}(u-\xi),O_{er}(u-\zeta)\right\}+W_{pr}(\xi)W_{pr}(\zeta)\text{covar}\left\{O_{pr}(u-\xi),O_{pr}(u-\zeta)\right\}\right]d\xi d\zeta$$

$$+ \int_{-\infty}^{\infty}\int\left[W_{ei}(\xi)W_{ei}(\zeta)\text{covar}\left\{O_{ei}(u-\xi),O_{ei}(u-\zeta)\right\}+W_{pi}(\xi)W_{pi}(\zeta)\text{covar}\left\{O_{pi}(u-\xi),O_{pi}(u-\zeta)\right\}\right]d\xi d\zeta$$

$$- 2\int_{-\infty}^{\infty}\int\left[W_{er}(\xi)W_{ei}(\zeta)\text{covar}\left\{O_{er}(u-\xi),O_{ei}(u-\zeta)\right\}+W_{pr}(\xi)W_{pi}(\zeta)\text{covar}\left\{O_{pr}(u-\xi),O_{pi}(u-\zeta)\right\}\right]d\xi d\zeta \quad (3)$$

In the case of high-quality prior data, the covariance of this prior data is much less than the covariance of the measured data. Thus all the second covariance terms in the integrals are insignificant compared to the first, so Eq.(3) can be rewritten as

$$\text{var}\{\hat{O}_{er}(u)\} \approx \int_{-\infty}^{\infty}\int W_{er}(\xi)W_{er}(\zeta)\text{covar}\left\{O_{er}(u-\xi),O_{er}(u-\zeta)\right\}d\xi d\zeta$$

$$+ \int_{-\infty}^{\infty}\int W_{ei}(\xi)W_{ei}(\zeta)\text{covar}\left\{O_{ei}(u-\xi),O_{ei}(u-\zeta)\right\}d\xi d\zeta$$

$$- 2\int_{-\infty}^{\infty}\int W_{er}(\xi)W_{ei}(\zeta)\text{covar}\left\{O_{er}(u-\xi),O_{ei}(u-\zeta)\right\}d\xi d\zeta \quad (4)$$

which is precisely the same result[6] as is obtained if the object had support $w_e(x)$. In the same way, the variance of the imaginary part can be shown to be

$$\text{var}\{\hat{O}_{ei}(u)\} \approx \int_{-\infty}^{\infty}\int W_{er}(\xi)W_{er}(\zeta)\text{covar}\left\{O_{ei}(u-\xi),O_{ei}(u-\zeta)\right\}d\xi d\zeta$$

$$+ \int_{-\infty}^{\infty}\int W_{ei}(\xi)W_{ei}(\zeta)\text{covar}\left\{O_{er}(u-\xi),O_{er}(u-\zeta)\right\}d\xi d\zeta$$

$$+ 2\int_{-\infty}^{\infty}\int W_{er}(\xi)W_{ei}(\zeta)\text{covar}\left\{O_{ei}(u-\xi),O_{er}(u-\zeta)\right\}d\xi d\zeta \quad (5)$$

which, again, is the same result as for an object with support constraint $w_e(x)$. Thus, as long as the prior knowledge is much less noisy than the measured data and its noise is uncorrelated with the measured data, using the prior knowledge is effectively the same as applying a support constraint. As a result, all the previously developed support theory[6] applies. In particular, although the overall noise in the Fourier domain has decreased since noise has been eliminated in the image domain, it is the behavior of the variances at each spatial frequency that determines if noise reduction outside the region of prior knowledge can occur. All the noise reduction achieved so far occurs only as a result of the noise removed from the prior knowledge area.

As for support, the prior knowledge must cause the variances in the constrained Fourier data to increase beyond that of the measured Fourier data in order for noise reduction outside the prior knowledge region to occur. As for the support theory[6], we will assume Fourier domain wide-sense stationary noise of the form

$$\begin{aligned} N_r(u) &\equiv O_{cr}(u) - E\{O_{cr}(u)\} \\ N_i(u) &\equiv O_{ci}(u) - E\{O_{ci}(u)\} \end{aligned} \tag{6}$$

where E{} denotes expected value and the complex noise (N_r, N_i) is a stochastic process which satisfies

$$\begin{aligned} \langle N_r(u_1)N_r(u_2)\rangle &= R_r(u_1-u_2)+R_r(u_1+u_2) \\ \langle N_i(u_1)N_i(u_2)\rangle &= R_i(u_1-u_2)-R_i(u_1+u_2) \\ \langle N_i(u_1)N_r(u_2)\rangle &= \langle N_r(u_1)N_i(u_2)\rangle = 0 \end{aligned} \tag{7}$$

The terms involving sums of spatial frequencies will be neglected since they only have an impact near dc. In particular, for the computer simulation results in Section 3, the noise will be assumed to be gaussian and delta-correlated in the Fourier domain; that is,

$$\begin{aligned} \langle N_r(u_1)N_r(u_2)\rangle &= \sigma_r^2\delta(u_1-u_2) \\ \langle N_i(u_1)N_i(u_2)\rangle &= \sigma_i^2\delta(u_1-u_2) \\ \langle N_i(u_1)N_r(u_2)\rangle &= \langle N_r(u_1)N_i(u_2)\rangle = 0 \end{aligned} \tag{8}$$

3. Computer Simulation Results

The algorithm used to enforce the prior knowledge constraints is the same as described in Ref.6; here, only a summary will be given. The algorithm's steps are: (1) in the image domain, replace the measured data with the prior knowledge in the region where prior knowledge is available, (2) Fourier transform, (3) if the real (imaginary) part of the measured Fourier data is less noisy than the imaginary (real), replace the iterated real (imaginary) part of the Fourier data with the measured data, but leave the imaginary (real) unchanged, (4) inverse Fourier transform, and (5) go back to step (1) until noise is minimized outside the region of prior knowledge. As discussed in Ref.6, this point of minimum noise will always occur prior to convergence of the algorithm as long as the variances of both the real and imaginary parts of the measured Fourier data are nonzero.

The picture in Figure 1 is the true image used for demonstrating the effectiveness of high-quality prior data. Figure 2 shows this picture corrupted with Fourier domain wide-sense stationary noise as in Eq.(8), with $\sigma_r^2 / \sigma_i^2 = .02$ and an average signal-to-noise ratio (SNR) in the image domain of 1. The algorithm described above was run for 20 iterations, and the prior knowledge was assumed to be perfect and in the lower right-hand quadrant of the image. Because the noise is wide-sense stationary, the only error reduction predicted by theory is in the asymmetric part of the support of the noisy data. Figure 3 shows the noisy image with the high-quality prior knowledge inserted but before the algorithm has been run, and Figure 4 shows the resulting image after running the algorithm. As can be seen, error reduction only occurred in the asymmetric part of the support of the noisy data.

Figure 1. True image

Figure 2. True image with noise added.

Figure 3. Noisy image with high-quality prior knowledge inserted.

Figure 4. Image after prior-knowledge is enforced

Since the prior-knowledge constraint is effectively a support constraint, the theory developed in Ref.6 can be used to predict the error reduction in the image at each step of the iteration. Figure 5 contains this comparison between theory and computer simulation. Notice the close match between theory and simulation. Also, notice that the point of minimum noise (at the 6th iteration) is barely discernible. This is due to the large mismatch between the real and imaginary variances. In addition, although it is not shown in Figure 5, the error in the symmetric part of the measured data support remained unchanged, as predicted by theory.

4. Conclusions

Prior high-quality knowledge of part of an image is a generalization of support constraints, and can be used to reduce the noise in the measured-data part of the image. The ability of prior knowledge to reduce noise outside the region of prior knowledge depends upon the noise correlation properties.

Acknowledgments

This research was funded by a grant from the U.S. Air Force Office of Scientific Research, Bolling AFB, Washington, D.C.

References

1. G. Demoment, "Image reconstruction and restoration: overview of common estimation structures and problems," IEEE Trans.Acoust., Speech, Signal Processing, vol.37, pp.2024-2036 (1989)
2. M.I. Sezan and A.M. Tekalp, "Survey of recent developments in digital image restoration," Opt.Eng., vol.29, pp.393-404 (1990)
3. H. Stark, editor, Image Recovery: Theory and Application, Academic Press, Orlando, FL (1987)
4. C.L. Matson, "Noise reduction in adaptive optics imagery with the use of support constraints," to be submitted to Applied Optics (Dec 1993)
5. C.L. Matson, "Fourier spectrum extrapolation and enhancement using support constraint," to appear in the IEEE Trans. Signal Proc., January 1994
6. C.L. Matson, "Variance reduction in Fourier spectra and their corresponding images with the use of support constraints," to appear in the J.Opt.Soc.Am.A., January 1994
7. R.A. Carreras, "Image restoration using nonlinear optimization techniques with a knowledge-based constraint," Proc.SPIE, vol.2029, pp.209-226 (1993)

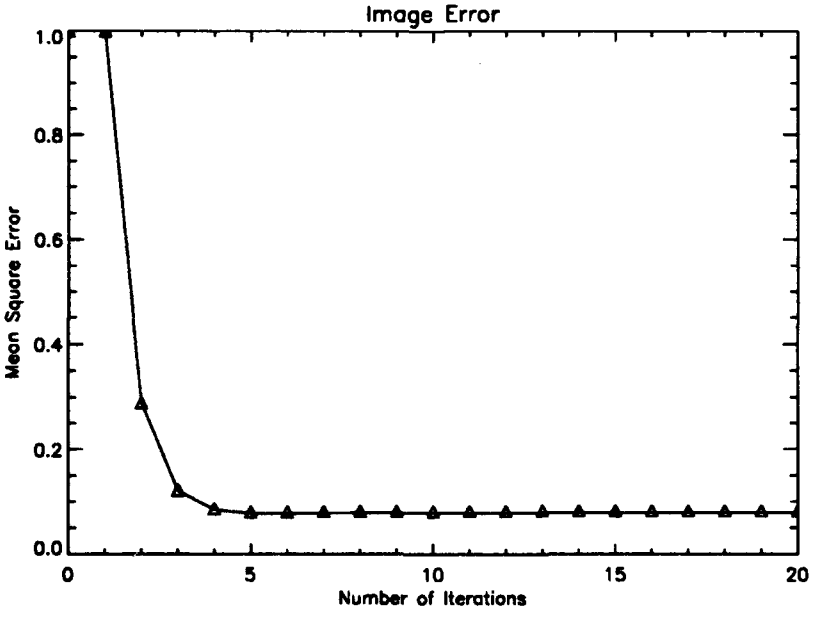

Figure 4. Normalized mean square error in the iterated image as a function of iteration number. The solid line is the theoretical prediction, and symbols denote computer simulation values.

APPENDIX E

Noise reduction in adaptive optics imagery with the use of support constraints

Charles L. Matson
Phillips Laboratory/LIMI, Kirtland AFB, NM 87117

Michael C. Roggemann
Dept of Engr Physics, Air Force Institute of Technology, Wright Patterson AFB, OH 45433

Abstract

The use of support constraints for noise reduction in images obtained with telescopes that use adaptive optics for atmospheric correction is discussed in this paper. Noise covariances are derived for this type of data, including the effects of shot noise and CCD read noise. The effectiveness of support constraints in achieving noise reduction is discussed in terms of these noise properties and in terms of the type of algorithms used to enforce the support constraint. Both a convex projections and a cost function minimization algorithm are used to enforce the support constraints, and it is shown via computer simulation and field data that the cost function algorithm results in artifacts in the reconstructions. The convex projections algorithms produced mean square error decreases in the image domain of approximately 10% for high light levels, but essentially no error decreases for low light levels.

1. Introduction

Atmospheric turbulence has long been recognized as the limiting factor in ground-based telescope resolution. Wavefront sensing and adaptive optics have been proposed as a method to lessen the impact of atmospheric turbulence distortion[1,2]. This approach has indeed been successful in generating substantially higher resolution from ground-based telescopes than otherwise achievable[3-5]. However, despite the method of image reconstruction and amount of image quality, the use of additional information beyond that of the measured data to improve image quality has been pursued for many decades[6-8]. One particular type of additional information, support constraints, has long been recognized as a means to superresolve data in the Fourier domain beyond the measurement region[9-12]. Recently[13,14], it has been shown that support constraints provide a means to improve the quality of the measured data itself in addition to providing a means for superresolution. The ability to improve the measured data has been shown to be a function of the statistical properties of the noise corrupting the measured data. In this paper, this recent theory is applied to imagery obtained from telescopes employing adaptive optics for atmospheric correction. The outline of the paper is as follows: the necessary statistical properties of the measured data noise are derived in Section 2, and the algorithms used to enforce support constraints are described in Section 3. Section 4 contains results from both computer simulations and field data, and Section 5 contains the conclusions.

2. Noise Covariances in Adaptive Optics Imagery

It has been previously shown[13,14] that the noise correlation properties in measured data are key to determining how effective support constraints can be in accomplishing noise reduction in images. Therefore, in this section, the noise covariances will be derived for adaptive optical imagery. The three noise sources considered are photon noise, CCD read noise, and noise resulting from imperfect atmospheric distortion removal by the adaptive optic system.

The detected image, d(x), is given by

$$d(x) = \sum_{k=1}^{K} \delta(x - x_k) + n_{CCD}(x) \tag{1}$$

where K is the number of detected photons and the effects of spatial integration due to finite detector size are neglected. The noise term $n_{CCD}(x)$ is assumed to be zero mean and delta-correlated with variance r(x). This corresponds to idealized CCD read noise with the flat-fielding and bias removal already accomplished. The Fourier transform of d(x), D(u), is given by

$$D(u) = \sum_{k=1}^{K} e^{-j2\pi u x_k} + N_{CCD}(u) \tag{2}$$

It is straightforward to show that the expected value of D(u), E{D(u)}, is given by

$$E\{D(u)\} = \overline{K} O_n(u) \overline{H}(u) \tag{3}$$

where $\overline{K}$ is the average photons per frame, $O_n(u)$ is the true object Fourier spectrum normalized to one at dc, and $\overline{H}(u)$ is the average optical transfer function of the atmosphere and telescope with adaptive optics and is real[15].

The covariances of the real and imaginary parts of D(u), as well as the cross-correlation between the real and imaginary parts, will now be derived, as these are the specific statistical expressions needed for predicting the performance of the deconvolution algorithms. Let the subscripts r and i denote the real and imaginary parts of a complex quantity, respectively. Then

$$\text{covar}\{D_r(u), D_r(v)\} = E\{D_r(u) D_r(v)\} - E\{D_r(u)\} E\{D_r(v)\}$$

$$= E\left\{\sum_{k=1}^{K}\cos(2\pi u x_k)\sum_{m=1}^{K}\cos(2\pi v x_m)\right\} + E\{N_{CCDr}(u)N_{CCDr}(v)\} - \overline{K}^2\overline{H}(u)\overline{H}(v)O_{nr}(u)O_{nr}(v) \quad (4)$$

$$\text{covar}\{D_i(u),D_i(v)\} = E\{D_i(u)D_i(v)\} - E\{D_i(u)\}E\{D_i(v)\}$$

$$= E\left\{\sum_{k=1}^{K}\sin(2\pi u x_k)\sum_{m=1}^{K}\sin(2\pi v x_m)\right\} + E\{N_{CCDi}(u)N_{CCDi}(v)\} - \overline{K}^2\overline{H}(u)\overline{H}(v)O_{ni}(u)O_{ni}(v) \quad (5)$$

$$\text{covar}\{D_r(u),D_i(v)\} = E\{D_r(u)D_i(v)\} - E\{D_r(u)\}E\{D_i(v)\}$$

$$= E\left\{\sum_{k=1}^{K}\cos(2\pi u x_k)\sum_{m=1}^{K}\sin(2\pi v x_m)\right\} + E\{N_{CCDr}(u)N_{CCDi}(v)\} - \overline{K}^2\overline{H}(u)\overline{H}(v)O_{nr}(u)O_{ni}(v) \quad (6)$$

where the equalities are obtained by noting that the CCD read noises are independent of all other noise sources. Following standard covariance calculation methods[16,17], it can be shown that

$$\text{covar}\{D_r(u),D_r(v)\} = \frac{\overline{K}}{2}O_{nr}(u-v)\overline{H}(u-v) + \frac{\overline{K}}{2}O_{nr}(u+v)\overline{H}(u+v) + \frac{1}{2}R_r(u-v) + \frac{1}{2}R_r(u+v)$$
$$+\overline{K}^2O_{nr}(u)O_{nr}(v)\text{covar}\{N_{AOr}(u),N_{AOr}(v)\} + \overline{K}^2O_{ni}(u)O_{ni}(v)\text{covar}\{N_{AOi}(u),N_{AOi}(v)\} \quad (7)$$

$$\text{covar}\{D_i(u),D_i(v)\} = \frac{\overline{K}}{2}O_{nr}(u-v)\overline{H}(u-v) - \frac{\overline{K}}{2}O_{nr}(u+v)\overline{H}(u+v) + \frac{1}{2}R_r(u-v) - \frac{1}{2}R_r(u+v)$$
$$+\overline{K}^2O_{ni}(u)O_{ni}(v)\text{covar}\{N_{AOr}(u),N_{AOr}(v)\} + \overline{K}^2O_{nr}(u)O_{nr}(v)\text{covar}\{N_{AOi}(u),N_{AOi}(v)\} \quad (8)$$

$$\text{covar}\{D_r(u),D_i(v)\} = -\frac{\overline{K}}{2}O_{ni}(u-v)\overline{H}(u-v) + \frac{\overline{K}}{2}O_{ni}(u+v)\overline{H}(u+v) - \frac{1}{2}R_i(u-v) + \frac{1}{2}R_i(u+v)$$
$$+\overline{K}^2O_{nr}(u)O_{ni}(v)\text{covar}\{N_{AOr}(u),N_{AOr}(v)\} - \overline{K}^2O_{ni}(u)O_{nr}(v)\text{covar}\{N_{AOi}(u),N_{AOi}(v)\} \quad (9)$$

where R(u) is the Fourier transform of r(x), and $N_{AO}(u)$ is the noise associated with the imperfect adaptive optics (AO) correction. Used in the derivation of Eqs.(7)-(9) is the fact that the real and imaginary parts of N_{AO} are uncorrelated. The first two terms in Eqs.(7)-(9) are due to photon noise, the second two terms are due to CCD read noise, and the last two terms are due to AO noise. No closed form expression is available for N_{AO}. However, accurate computer simulations[3] can be used to determine the structure of the variances and covariances of N_{AO} for desired telescope/r_0/AO combinations. For the computer simulations discussed in this paper, two combinations were utilized. The first combination assumes D/r_0 =5, one actuator per r_0 cell, and a one meter unobscured aperture. The second combination assumes D/r_0 =16, one actuator per r_0 cell, and a 1.6 meter obscured aperture. This combination is a model of the 1.6 meter compensated telescope at the Air Force Maui Optical Station (AMOS). Radially averaged variances of N_{AO} for the first and second combinations are shown in Figure 1. Notice that there is a marked dissimilarity in the magnitudes of the noises for most spatial frequencies. This dissimilarity implies the possibility of noise reduction with the use of support constraints[14], but in fact this does not occur, as will be shown in the next section. This is due to the fact that the correlation of the noises, as well as their relative magnitudes, determine the ability of support constraints to cause error reduction[13,14]. The correlation coefficients of the covariances can be seen in Figure 2. This plot is for the first combination and assumes that the correlation

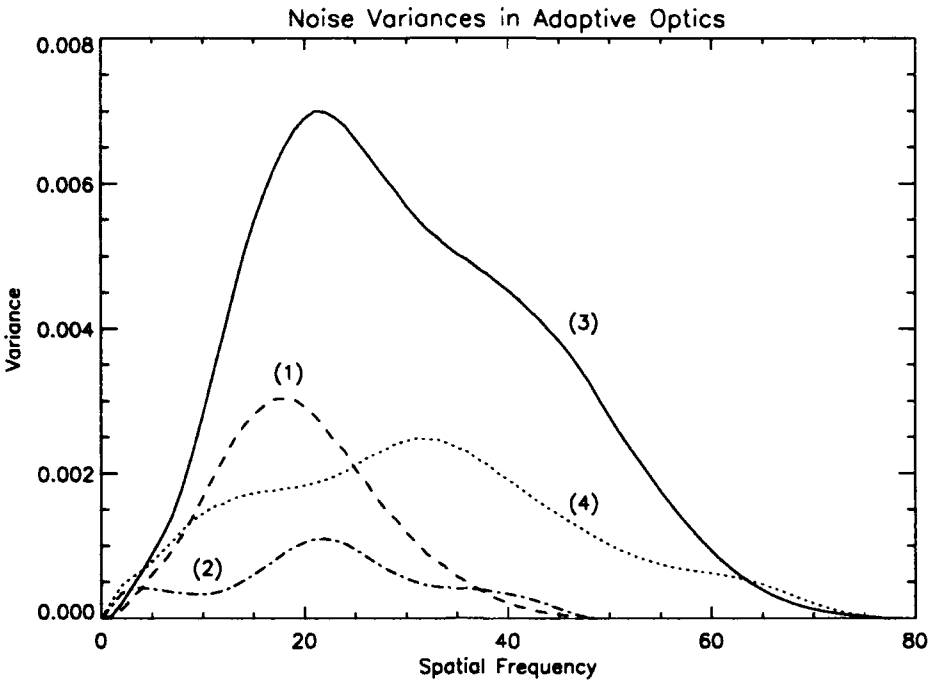

Figure 1. Adaptive optics noise variances. Curves (1) and (2) are the radially-averaged real and imaginary noise variances for combination 1 described in the text, respectively, while curves (3) and (4) are the radially-averaged real and imaginary noise variances for combination 2.

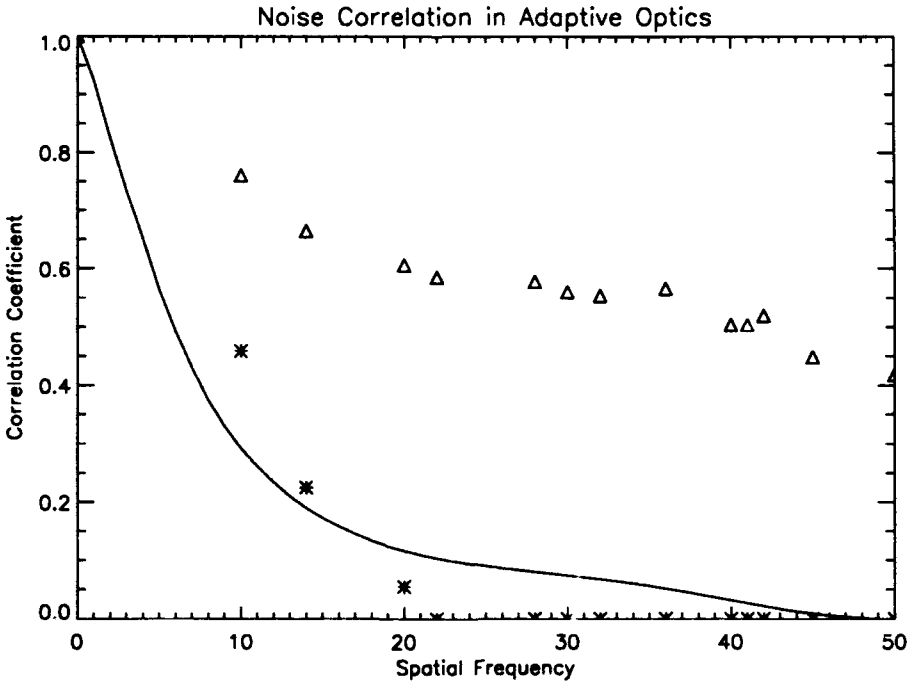

Figure 2. Adaptive optics noise correlation coefficients for combination 1. The solid line is a plot of the compensated OTF, while the triangles are computer simulation points for the real correlation coefficients and the asterisks are computer simulation points for the imaginary correlation coefficients.

coefficients are independent of location and orientation, which is a simplifying assumption. Also plotted with the correlation coefficients is the OTF of the atmosphere/telescope combination. The inverse Fourier transform of the OTF is essentially finite in extent and this finite extent enforces correlation among the noises in the Fourier domain. As expected, the shape of the OTF provides a lower limit to the correlation of the adaptive optics noise. Notice that the real part of the noises are much more correlated than the imaginary parts of the noise. The large amount of correlation is the determining factor in the amount of noise reduction achievable using support constraints. Because the noises are so highly correlated, the covariances in Eqs.(7)-(9) can be approximated by their variances, which results in

$$\text{covar}\{D_r(u),D_r(v)\} \approx \frac{\overline{K}}{2}O_{nr}(u-v)\overline{H}(u-v)+\frac{\overline{K}}{2}O_{nr}(u+v)\overline{H}(u+v)+\frac{1}{2}R_r(u-v)+\frac{1}{2}R_r(u+v)$$
$$+\overline{K}^2O_{nr}(u)O_{nr}(v)\text{var}\{N_{AOr}(u)\}+\overline{K}^2O_{ni}(u)O_{ni}(v)\text{var}\{N_{AOi}(u)\} \quad (10)$$

$$\text{covar}\{D_i(u),D_i(v)\} \approx \frac{\overline{K}}{2}O_{nr}(u-v)\overline{H}(u-v)-\frac{\overline{K}}{2}O_{nr}(u+v)\overline{H}(u+v)+\frac{1}{2}R_r(u-v)-\frac{1}{2}R_r(u+v)$$
$$+\overline{K}^2O_{ni}(u)O_{ni}(v)\text{var}\{N_{AOr}(u)\}+\overline{K}^2O_{nr}(u)O_{nr}(v)\text{var}\{N_{AOi}(u)\} \quad (11)$$

$$\text{covar}\{D_r(u),D_i(v)\} \approx -\frac{\overline{K}}{2}O_{ni}(u-v)\overline{H}(u-v)+\frac{\overline{K}}{2}O_{ni}(u+v)\overline{H}(u+v)-\frac{1}{2}R_i(u-v)+\frac{1}{2}R_i(u+v)$$
$$+\overline{K}^2O_{nr}(u)O_{ni}(v)\text{var}\{N_{AOr}(u)\}-\overline{K}^2O_{ni}(u)O_{nr}(v)\text{var}\{N_{AOi}(u)\} \quad (12)$$

3. Algorithm Description and Performance Prediction

In this section, the two algorithms used to enforce support constraints in the deconvolution process will be described. Predictions of their performance will also be analyzed in terms of the noise correlation properties developed in the previous section. It is assumed that an unbiased estimate of the true Fourier data exists, along with an unbiased estimate of the variances of the estimate of the mean. It is also assumed that the estimated Fourier data exists only in a finite region. For the results in this paper, it is assumed that this region is roughly centered at dc and the outer limits are determined either by a low-pass filter such as a telescope causes (in the infinite signal-to-noise (SNR) case) or the outer limits are determined by the SNR of the data becoming sufficiently small that only noise exists outside these limits. However, these results are easily generalized to the case where a number of finite regions of Fourier data are measured such as in interferometry.

Convex Projections

The first algorithm to be described is a convex projections approach[18-20]. The steps of the algorithm are as follows: (1) apply support constraints in the image domain, (2) Fourier transform the support-constrained data, (3) modify the support-constrained Fourier data so that it stays within a $\pm 2\sigma$ region about the measured mean where measured data is available, and constrain the magnitude of the support-constrained data to stay near zero outside of this region, (4) inverse Fourier transform the data, (5) go to step 1 and continue until the image changes are insignificant. The most important conceptual step in this algorithm is step (3). If, after applying support constraints, the support-constrained Fourier data is within the $\pm 2\sigma$ measured data region, support constraints cannot change the noise properties in the image domain inside the support constraint because no changes can be made in the Fourier domain. Therefore, the key to the usefulness of support constraints is the effect they have upon the iterated Fourier data. To analyze this further, let $O_S(u)$ be the iterated Fourier data after one application of support constraints. Following the development in Ref.14, the variance of the real and imaginary parts of $O_S(u)$ are given by

$$\mathrm{var}\{O_{rr}(u)\} = \int_{-\infty}^{\infty}\int W_r(\xi)W_r(\zeta)F(u-\xi)F(u-\zeta)\mathrm{covar}\{D_r(u-\xi),D_r(u-\zeta)\}d\xi d\zeta$$

$$+ \int_{-\infty}^{\infty}\int W_i(\xi)W_i(\zeta)F(u-\xi)F(u-\zeta)\mathrm{covar}\{D_i(u-\xi),D_i(u-\zeta)\}d\xi d\zeta$$

$$- 2\int_{-\infty}^{\infty}\int W_r(\xi)W_i(\zeta)F(u-\xi)F(u-\zeta)\mathrm{covar}\{D_r(u-\xi),D_i(u-\zeta)\}d\xi d\zeta \qquad (13)$$

and

$$\mathrm{var}\{O_{ii}(u)\} = \int_{-\infty}^{\infty}\int W_r(\xi)W_r(\zeta)F(u-\xi)F(u-\zeta)\mathrm{covar}\{D_i(u-\xi),D_i(u-\zeta)\}d\xi d\zeta$$

$$+ \int_{-\infty}^{\infty}\int W_i(\xi)W_i(\zeta)F(u-\xi)F(u-\zeta)\mathrm{covar}\{D_r(u-\xi),D_r(u-\zeta)\}d\xi d\zeta$$

$$+ 2\int_{-\infty}^{\infty}\int W_r(\xi)W_i(\zeta)F(u-\xi)F(u-\zeta)\mathrm{covar}\{D_i(u-\xi),D_r(u-\zeta)\}d\xi d\zeta \qquad (14)$$

where F(u) is a real filter which deconvolves out $\overline{H}(u)$ and filters the resulting Fourier spectrum to minimize the noise amplification effects, and W(u) is the Fourier transform of the support constraint w(x). It is necessary to insert Eqs.(10)-(12) into Eqs.(13) and (14) to analyze the variances further. This will be done for two limiting cases: high light level and low light level.

In the high light level case (infinite SNR), the last two terms in Eqs.(10)-(12) dominate the covariances. Substituting these equations with this simplification into Eq.(13) gives

$$\mathrm{var}_{HL}\{O_{rr}(u)\} \approx \overline{K}^2F^2(u)\mathrm{var}\{N_{AOr}(u)\}\int_{-\infty}^{\infty}\int W_r(\xi)W_r(\zeta)O_{nr}(u-\xi)O_{nr}(u-\zeta)d\xi d\zeta$$

$$+\overline{K}^2F^2(u)\mathrm{var}\{N_{AOi}(u)\}\int_{-\infty}^{\infty}\int W_r(\xi)W_r(\zeta)O_{ni}(u-\xi)O_{ni}(u-\zeta)d\xi d\zeta$$

$$+\overline{K}^2F^2(u)\mathrm{var}\{N_{AOr}(u)\}\int_{-\infty}^{\infty}\int W_i(\xi)W_i(\zeta)O_{ni}(u-\xi)O_{ni}(u-\zeta)d\xi d\zeta$$

$$+\overline{K}^2F^2(u)\mathrm{var}\{N_{AOi}(u)\}\int_{-\infty}^{\infty}\int W_i(\xi)W_i(\zeta)O_{nr}(u-\xi)O_{nr}(u-\zeta)d\xi d\zeta$$

$$-2\overline{K}^2F^2(u)\mathrm{var}\{N_{AOr}(u)\}\int_{-\infty}^{\infty}\int W_r(\xi)W_i(\zeta)O_{nr}(u-\xi)O_{ni}(u-\zeta)d\xi d\zeta$$

$$+2\overline{K}^2F^2(u)\mathrm{var}\{N_{AOi}(u)\}\int_{-\infty}^{\infty}\int W_r(\xi)W_i(\zeta)O_{ni}(u-\xi)O_{nr}(u-\zeta)d\xi d\zeta \qquad (15)$$

where F(u) is assumed approximately constant in the region where the integrands of Eq.(15) are significantly nonzero. This approximation is reasonably valid where the object is significantly larger than the width of the inverse Fourier transform of F(u), which should be the case when the object is well-resolved by the telescope. Furthermore, the integrals in Eq.(15) are multiplications of convolutions which can be simplified to obtain

$$\mathrm{var}_{HL}\{O_{nr}(u)\} \approx F^2(u)\left[\overline{K}^2O_{nr}^2(u)\mathrm{var}\{N_{AOr}(u)\}+\overline{K}^2O_{ni}^2(u)\mathrm{var}\{N_{AOi}(u)\}\right] \qquad (16)$$

where the term in the square brackets is seen, by Eq.(10), to be the variance of the real part of the measured Fourier data, and thus Eq.(16) reflects the starting variance of the real part of the measured data scaled by the filter F(u). In the same way, it can be shown that

$$\mathrm{var}_{HL}\{O_{ni}(u)\} \approx F^2(u)\left[\overline{K}^2O_{ni}^2(u)\mathrm{var}\{N_{AOr}(u)\}+\overline{K}^2O_{nr}^2(u)\mathrm{var}\{N_{AOi}(u)\}\right] \qquad (17)$$

which is the starting variance of the imaginary part of the measured data scaled by F(u), as well. As a result, the variances of the support-constrained Fourier data are, on average, the same as the variances of the measured Fourier data. This means that most of the support-constrained Fourier spectrum will reside inside the $\pm 2\sigma$ region and thus the application of support constraints will not have much effect on noise reduction inside the support constraint due to the inability of the measured data to act as an effective constraint. The reason that support constraints do not allow noise reduction is that the noises are too correlated, which results from $\mathrm{var}\{N_{AOr}(u)\}$, $\mathrm{var}\{N_{AOi}(u)\}$, and F(u) being essentially constant where the integrands are significantly nonzero, which is only an approximation. As a result, some variance modification can occur as a result of support constraints since these terms are not exactly constant as previously assumed. However, although the terms are not exactly constant, they are still closely approximated by a constant, so not much noise reduction is expected in this case. Looking again at Figure 1, it can be seen that, in some regions, $\mathrm{var}\{N_{AOr}(u)\}$ and $\mathrm{var}\{N_{AOi}(u)\}$ are changing quite rapidly. Thus some noise reduction in images due to the constraining of the support-constrained Fourier data to remain in the measured data $\pm 2\sigma$ region should occur, but probably not much. In addition, this result assumes that the region of integration where the integrand is significantly nonzero is contained inside the region of measured data. However, in regions near the edge of the measured data, the zeros representing the non-measured data will be correlated in

via the integrals in Eqs.(13) and (14), and thus the variances of the support-constrained Fourier data will become significantly worse near the data region edges, in general. Although this does not improve the quality of the measured Fourier data, it extends the measured data out into regions where no data was measured. This is the essence of superresolution.

Consider now the low light level case, where photon noise dominates and CCD read noise is not an issue. Then the first two terms in Eqs.(10)-(12) are dominant and, looking at the variances of the real part of the support-constrained Fourier data, Eq.(13) becomes

$$\mathrm{var}_{LL}\{O_{sr}(u)\} \approx \frac{\overline{K}}{2}F^2(u)\int_{-\infty}^{\infty}\int W_r(\xi)W_r(\zeta)\left[O_{nr}(\zeta-\xi)\overline{H}(\zeta-\xi)+O_{nr}(2u-\zeta-\xi)\overline{H}(2u-\zeta-\xi)\right]d\xi d\zeta$$

$$+\frac{\overline{K}}{2}F^2(u)\int_{-\infty}^{\infty}\int W_i(\xi)W_i(\zeta)\left[O_{nr}(\zeta-\xi)\overline{H}(\zeta-\xi)-O_{nr}(2u-\zeta-\xi)\overline{H}(2u-\zeta-\xi)\right]d\xi d\zeta$$

$$+\overline{K}F^2(u)\int_{-\infty}^{\infty}\int W_r(\xi)W_i(\zeta)\left[O_{ni}(\zeta-\xi)\overline{H}(\zeta-\xi)-O_{ni}(2u-\zeta-\xi)\overline{H}(2u-\zeta-\xi)\right]d\xi d\zeta \qquad (18)$$

The first term in the brackets in the integrands of Eq.(18) is a function only of the difference in spatial frequencies. Without the filter F(u) effects or the second terms in the brackets (which are only significant near dc) the noise model would fit the wide-sense stationary model assumed in Ref.14 and the variances of the real and imaginary parts of the measured data would be equal. It has been shown[14] that this type of noise results in no noise reduction, and even a slight noise increase inside the support constraint. For Eq.(18), because of the term F(u) and the second terms in the brackets in Eq.(18), noise reduction may be possible, but if noise reduction is achieved not much is expected since the noises are essentially wide-sense stationary. Of course, near the edge of the measured data region, the variances of the support-constrained Fourier data will be affected quite a bit because of the zeros outside the measured data region, so superresolution is possible because of this as for the high-light level case. Overall, less noise reduction is expected for the low-light level case than for the high-light level case since the real and imaginary variances are essentially identical away from dc, but large amounts of noise reduction in either case are not expected. The same functional dependence is seen in the variances of the imaginary part of the support-constrained Fourier data as well, so the same conclusions apply.

The situation where CCD read noise dominates is essentially identical to the case where shot noise dominates, so not much noise reduction is expected in this limit, as well.

One final issue with the convex projections approach is that the $\pm 2\sigma$ region in the Fourier domain will, in general, not be the true $\pm 2\sigma$ region since it is created from measured data. As a result, errors in creating this region should result in less noise reduction than what would occur with an accurate $\pm 2\sigma$ region.

Cost Function Minimization

The second algorithm used to enforce support constraints is a cost function minimization approach. The cost function minimized is given by

$$\text{cost function} = \sum_{\text{data region}}\left\{\frac{\left[O_{sr}(u)-F(u)D_r(u)\right]^2}{F^2(u)\sigma_{sr}^2(u)}+\frac{\left[O_{si}(u)-F(u)D_i(u)\right]^2}{F^2(u)\sigma_{si}^2(u)}\right\}$$

$$+ \sum_{\substack{\text{outside} \\ \text{data region}}} \left[\frac{O_{sr}^2(u)}{\sigma_{sr}^2} + \frac{O_{i}^2(u)}{\sigma_{si}^2} \right] \tag{19}$$

where the $\sigma_{sr}^2(u)$ and $\sigma_{si}^2(u)$ terms are the variances of the real and imaginary parts of the measured Fourier data, respectively, and the minimization is over all object Fourier spectra O_S. The first two summations are the data matching terms, while the third is the regularization term. The parameters $1/\sigma_{sr}^2$ and $1/\sigma_{si}^2$ act as regularization parameters and are calculated by setting σ_{sr}^2 and σ_{si}^2 equal to the average variances of the real and imaginary parts of the measured Fourier spectrum, respectively, at the edge of the data matching region. The cost function is minimized by using a conjugate gradient minimization approach.

The cost function minimization approach should have a performance similar to the convex projections approach with one major exception. Because no "hard edges" are established by the cost function for the region in the Fourier domain where the support-constrained Fourier data must remain as the minimization proceeds, the correlation of the zeros outside of the measured data region into the measured data region can significantly modify the measured Fourier data. This results in much worse performance for the cost function approach as compared to the convex projections approach.

4. Algorithm Performance

The computer simulation runs presented in this section were accomplished using a highly accurate simulation which models the effects of atmosphere, telescope, adaptive optics, photon noise, and CCD read noise[3]. Because the noise effects for both CCD read noise and photon noise are structurally similar, CCD read noise was not included in the simulations. The computer simulation was used to obtain both images and point source corrections. Sample means and sample variances were calculated and used in the deconvolution algorithms.

Both algorithms were run for a variety of true objects using the two telescope/AO combinations discussed in Section 3. For each true object, both a high and a low light level case was run. For each computer simulation run, a filter F(u) was chosen as follows:

$$F(u) = \frac{\mathcal{F}(\text{circ})}{\overline{H}(u)} \tag{20}$$

where the Fourier transform of the circle function was chosen in order that a finite support could be applied in a way consistent with the $\pm 2\sigma$ region in the Fourier domain. The size of the circle was chosen such that the first zero of its Fourier transform was located just outside the region of accurately measured Fourier data. Thus most of the energy in the filter was located in the region in Fourier space where measured data was available. This was done since it has been shown[13] that very little superresolution is achievable for data with moderate SNRs and so most of the emphasis in the algorithm was placed upon improving the quality of the measured data and not superresolution. The true object's Fourier spectrum was also multiplied by $\mathcal{F}(\text{circ})$ and the mean square error between the blurred true object and the deconvolved support-constrained object was calculated at each iteration of the algorithm. This approach follows that of Lannes[21], where the amount of achievable superresolution is approximately determined before the deconvolution process is started, and the measured data is modified by a filter to be consistent with this amount of superresolution.

A number of interesting results were seen from the computer simulation runs. The first is that the cost function minimization algorithm consistently produced deconvolved images which had noticeable artifacts. In general, the mean square error in the image increased after deconvolution with this algorithm, but in one case severe artifacts were seen in the reconstruction even though the mean square error in the image decreased. The problem appears to be the inability of the algorithm to enforce hard limits on the Fourier data to stay within the $\pm 2\sigma$ region at the boundaries of the measured data. Later in this section results will be shown which demonstrate this problem.

The convex projections algorithm, in general, resulted in decreased noise levels in the image. The high light level scenario resulted in the most noise reduction, as expected, and noise levels never increased as a result of support constraints. The average mean square error reduction in the image was approximately 10%. In the low light level scenario, on average, no reduction in noise occurred. Sometimes the noise slightly increased and sometimes the noise slightly decreased. This also is consistent with expectations from the theory in Section 3. Two different forms of the convex projections algorithm were used. The first allowed superresolution to occur, while the second explicitly zeroed out extrapolated data and required the iterated Fourier data near the edge of the measured data region to exactly match the measured data. In general, the algorithm which allowed superresolution to occur resulted in noisier image reconstructions. This also was expected since superresolution is an inherently noisy process[13].

Two computer simulation results will now be discussed in detail. The first run used the second telescope/adaptive optics combination which is a realistic model of the AMOS compensated 1.6m telescope. The true object was a Voyager picture of Dione, a moon of Saturn. A high light level case was run with 10^{10} photons per frame. This resulted in Fourier data which had SNRs of well over 10 for all spatial frequencies except those at the extreme edge of the telescope transfer function. The measured data was truncated at where the SNR approached one. One hundred iterations of both the convex projection algorithm and the cost function algorithm were run. The convex projections algorithm was run twice. The second time, in the Fourier domain the support-constrained data was zeroed out outside of the measured region on each iteration. In addition, in an annulus region 15 pixels wide at the edge of the measured Fourier data, the support-constrained Fourier data was replaced with the measured data. This second approach to convex projections was accomplished to keep the correlation of the zeros outside of the measured data from propagating inwards and corrupting the measured data. Thus the image domain errors for this case reflect only the changes in the measured Fourier data region and no superresolution is achieved at all.

Figure 3 shows the error in the Dione reconstructions as a function of iteration number for both convex projection algorithms and the cost function algorithm. Notice that the error dramatically increases for the cost function algorithm, while both convex projections algorithms result in reduced noise. The convex projection algorithm which explicitly prevents any superresolution from occurring has lower noise levels than for the one which allows some superresolution to occur. This is not surprising, since it has been shown that any superresolution in the Fourier data is much noisier than the measured data[13]. The true blurred image, the linear deconvolution image with no support constraints, and the images resulting from the convex projections and cost function algorithms are shown in Figure 4. The images all look very similar. Although it does not reproduce well on paper, the cost function reconstruction has a series of concentric rings near the edge of Dione's horizon which are artifacts not contained in the true image. Thus the increase in noise shown in Figure 3 is not just a generalized noise increase but a result of specific artifacts. To analyze this effect further, slices of the magnitude of the reconstructed Fourier spectra were plotted and compared to the true Fourier spectrum. The results are shown in Figure 5. Notice that the cost function reconstruction is much noisier than the convex projections reconstruction near the edge of the measured data region, with the error decreasing as spatial frequency is decreased. This is consistent with the explanation given in Section 3, that the cost function algorithm doesn't prevent the zeros outside the data region from strongly affecting the measured Fourier data near the region boundary.

The convex projection reconstruction doesn't have any dramatic improvement in image quality. Apparently, the algorithm resulted in lower noise levels throughout the image, but even the achieved mean square error reduction of 35% did not produce dramatic image improvements.

The low light level computer simulation run for Dione used all the same parameters as for the high light level case except that 10^4 photons per frame were utilized. The error in the image reconstructions as a function of the iteration number are shown in Figure 6. Notice that all the reconstructions are more noisy than at the start, but the cost function algorithm again has the most noise.

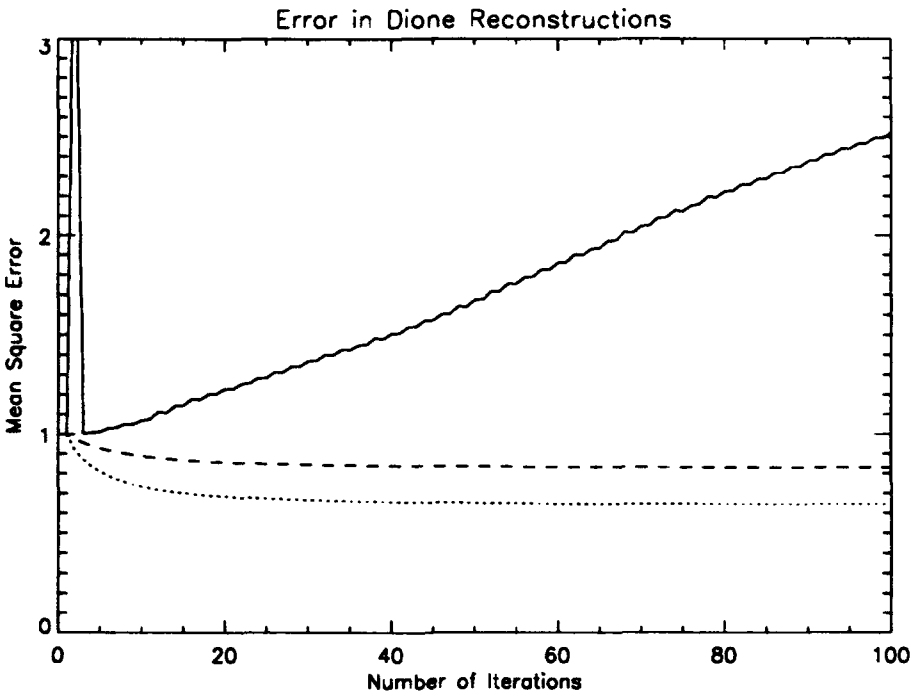

Figure 3. Mean square error in the Dione reconstructions for 10^{10} photons/frame. The solid line is from the cost function minimization algorithm, the dashed line is from the convex projections algorithm with superresolution, and the dotted line is from the convex projections algorithm with no superresolution.

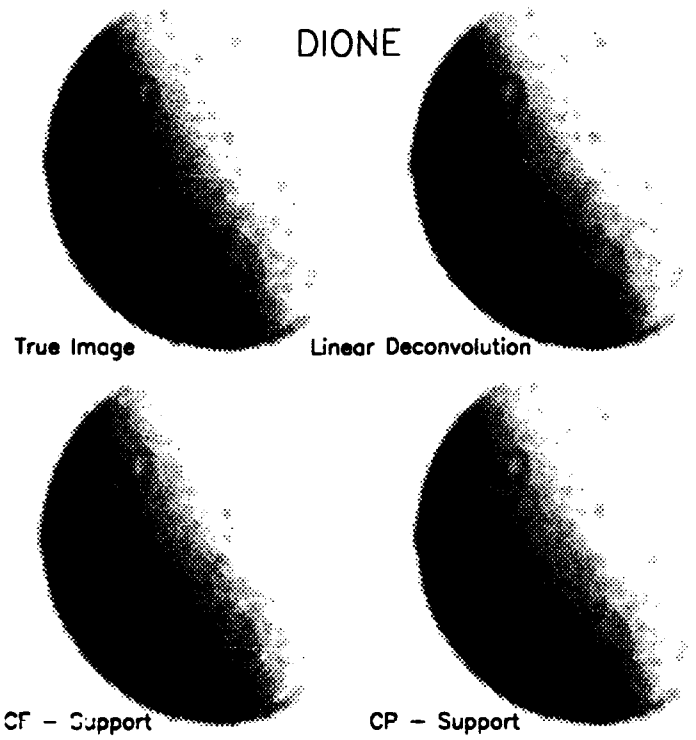

Figure 4. Dione images: blurred true image, linear deconvolution reconstruction, and reconstructions using the cost function and convex projection algorithms.

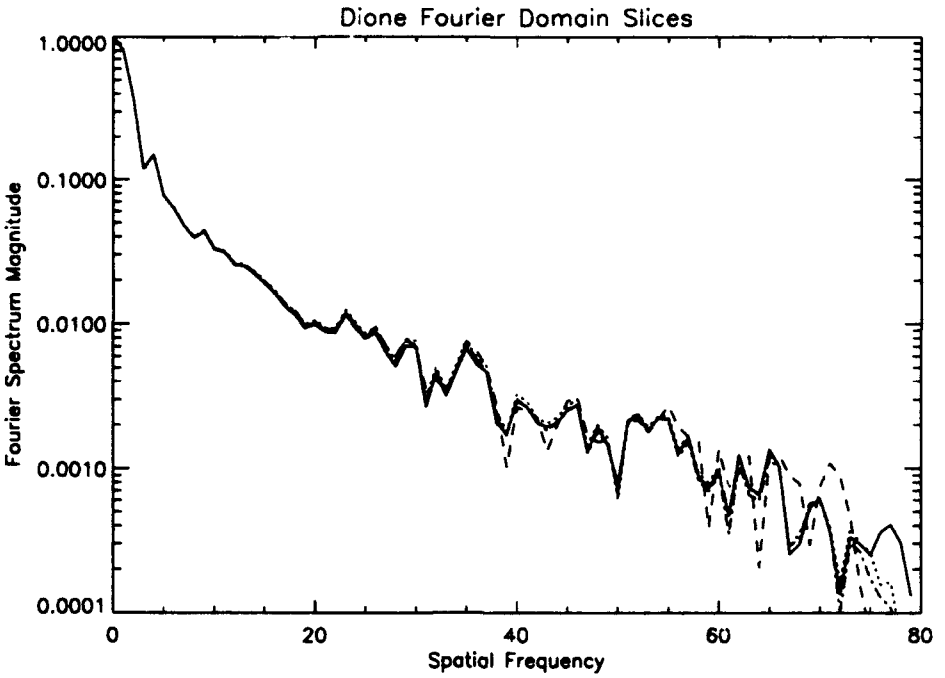

Figure 5. Normalized Dione Fourier domain slices: solid line is from the true blurred Dione spectrum, dashed line is from cost function reconstruction, dotted line is from the linear reconstruction, and the dot-dash line is from the convex projections reconstruction.

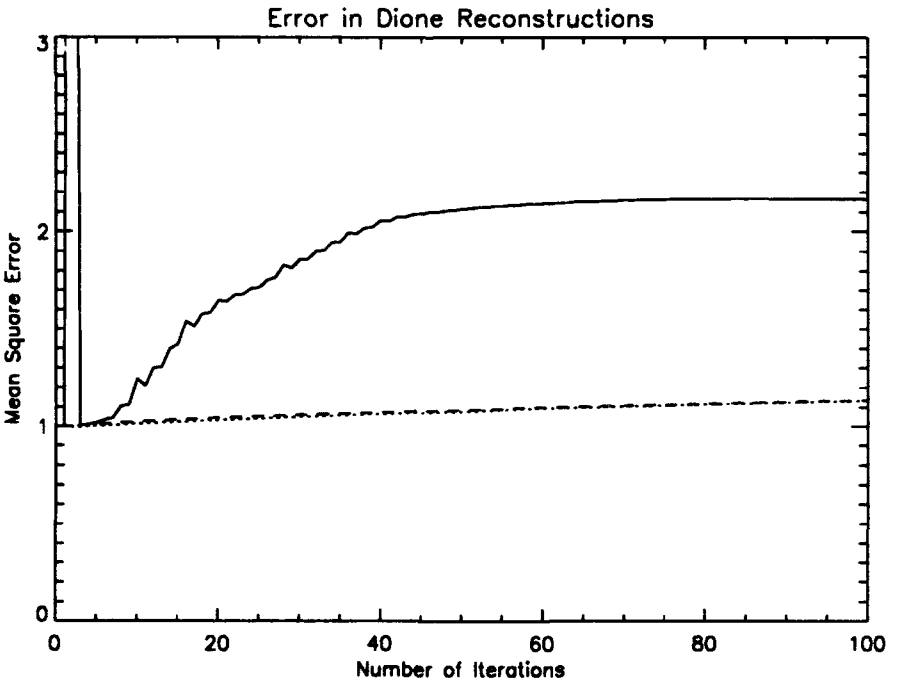

Figure 6. Mean square error in the Dione reconstructions for 10^4 photons/frame. The solid line is from the cost function minimization algorithm, the dashed line is from the convex projections algorithm with superresolution, and the dotted line is from the convex projections algorithm with no superresolution.

The next simulation results are for a satellite model. The first combination of telescope/AO was used for this simulation. The high light level case utilized 10^8 photons per frame. The errors in the reconstructions for the cost function algorithm and the two implementations of the convex projections algorithms are show in Figure 7. Notice that there is essentially no noise reduction with the convex projections algorithms. However, notice that the cost function algorithm indicates a large decrease in error in the image. This indication of error reduction is misleading, as can be seen in the image reconstruction in Figure 8. Notice that cost function algorithm reconstruction took dim parts of the object and obliterated them, concentrating the energy from these regions into smaller, higher intensity regions. Two important conclusions result from this observation. The first is that a mean square image error metric is only useful in as far as it reflects overall noise decrease in the image. It does not indicate the presence of artifacts. The second conclusion is about the concentration of energy from spread out dim regions of the image into smaller, brighter regions. For an extended object such as a satellite, the error this causes is plain. However, it is precisely this type of behavior that is used to claim superresolution in images which consist of a number of point sources! As a result, many claims of superresolution in the literature may reflect this sort of artifact generation, rather than true superresolution.

Fourier domain slices of the true blurred image and the reconstructions are shown in Figure 9. The point source used to deconvolve out the telescope/AO effects was modeled as slightly inaccurate, as is the case for most field data, so the noise is not zero mean. As a result, interpreting the error in the cost function reconstruction slice isn't as obvious as for the Dione case. However, it can be seen that the cost function reconstruction slice of the Fourier data is significantly different from the true object slice and the convex projections reconstruction slices.

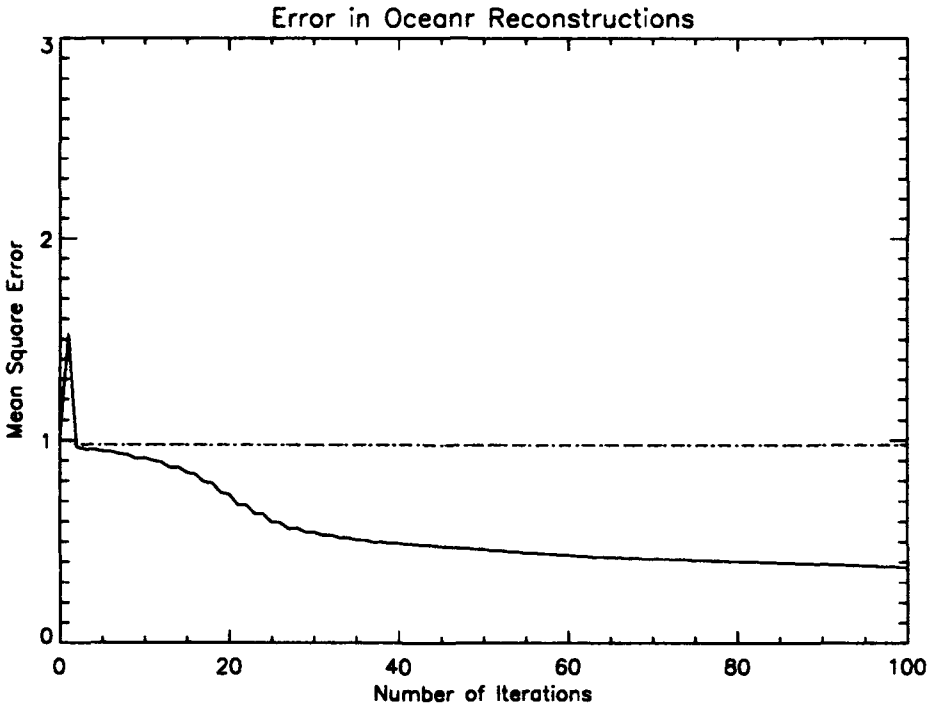

Figure 7. Mean square error in the satellite reconstructions for 10^8 photons/frame. The solid line is from the cost function minimization algorithm, the dashed line is from the convex projections algorithm with superresolution, and the dotted line is from the convex projections algorithm with no superresolution.

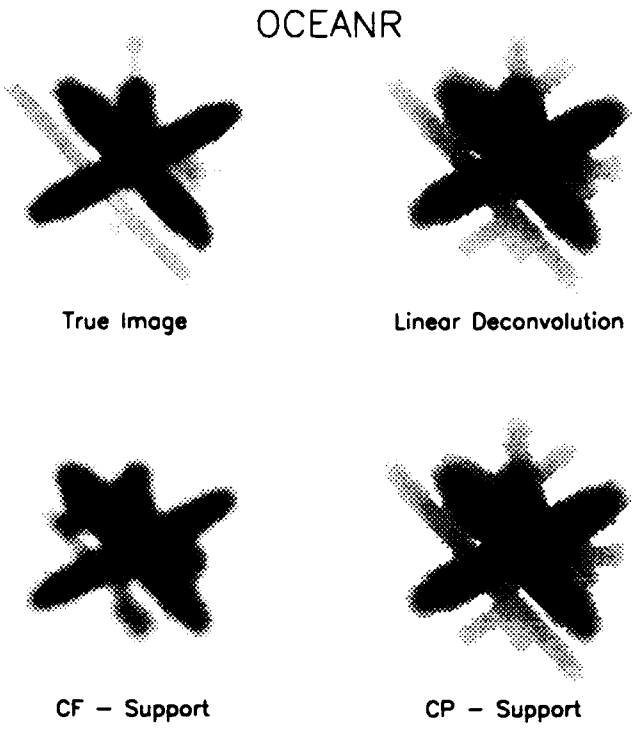

Figure 8. Satellite images: blurred true image, linear deconvolution reconstruction, and reconstructions using the cost function and convex projection algorithms.

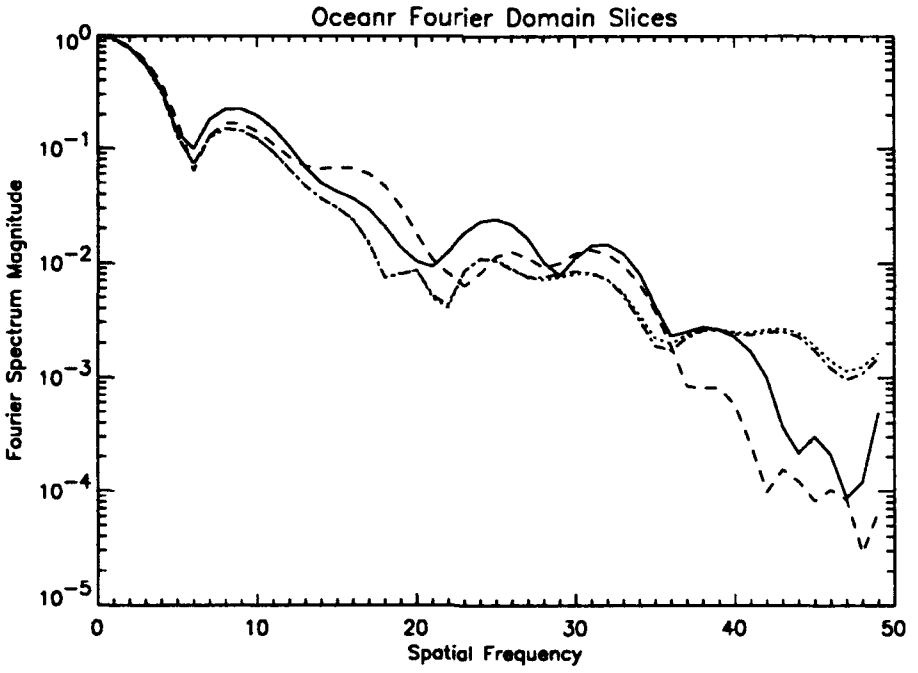

Figure 9. Normalized satellite Fourier domain slices: solid line is from the true blurred satellite spectrum, dashed line is from cost function reconstruction, dotted line is from the linear reconstruction, and the dot-dash line is from the convex projections reconstruction.

The low light level simulation run for this satellite model is the same as for the high light level case except that 10^4 photons per frame were utilized. The errors in the reconstructions are shown in Figure 10, and it can be seen that the convex projections algorithms again did not result in noise reduction, while the cost function algorithm indicates a small amount of decrease. The cost function algorithm terminated after 60+ iterations because the cost function had stopped decreasing.

Finally, the two algorithms were run using field data collected from the AMOS 1.6m telescope. The first image reduced was Ganymede. The reconstructions were in the low light level case since the SNR of the data approached one at approximately 20% of the diffraction limit. Thus large amounts of image improvement are not expected. The reconstructions are shown in Figure 11, where an additional convex projections algorithm was run using positivity as well as support as a constraint. The linear deconvolution result shows the presence of what is probably the region Galileo Regio in the right-central part of the image. The size of this feature is consistent with images obtained from the Voyager probes. The cost function reconstruction shows the same sort of artifacts as seen in the satellite reconstructions of Figure 8. The dim regions of the moon have energy taken away from them and added to the bright part of the moon. This results in the reconstruction of the region Galileo Regio increasing in size, and the overall moon diameter decreasing.

The convex projections reconstruction shows small differences between it and the linear reconstruction image. From the computer simulations, this may or may not be more accurate than the linear reconstruction since, in the low light level cases, noise levels both increased slightly and decreased slightly. In addition, a convex projections reconstruction was accomplished using both support and positivity. The differences between the reconstructions with positivity and without positivity are negligible.

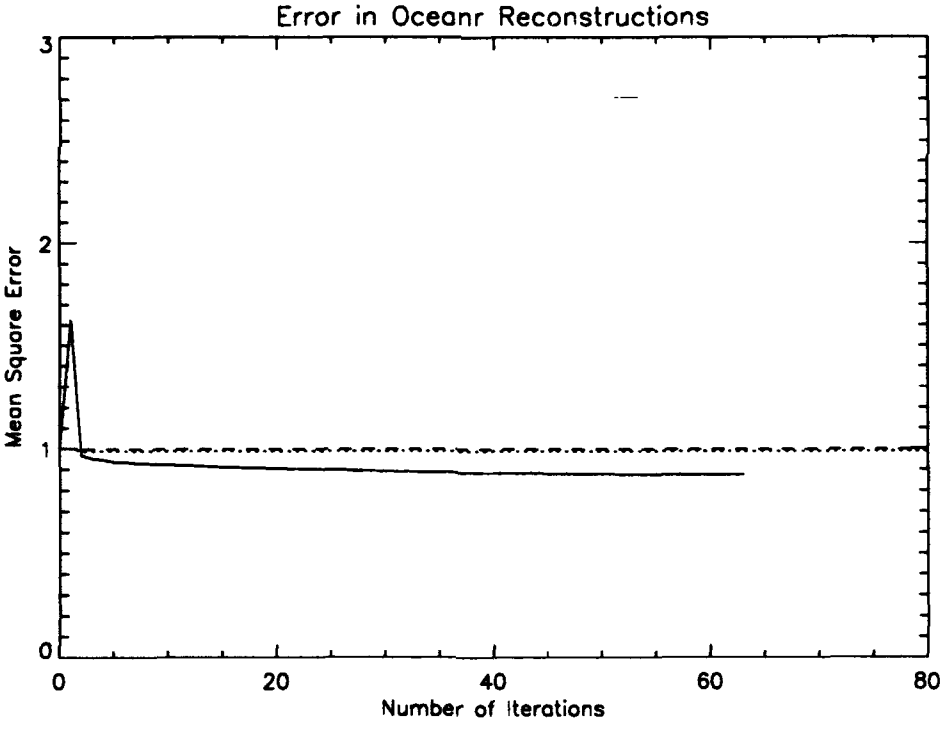

Figure 10. Mean square error in the satellite reconstructions for 10^8 photons/frame. The solid line is from the cost function minimization algorithm, the dashed line is from the convex projections algorithm with superresolution, and the dotted line is from the convex projections algorithm with no superresolution.

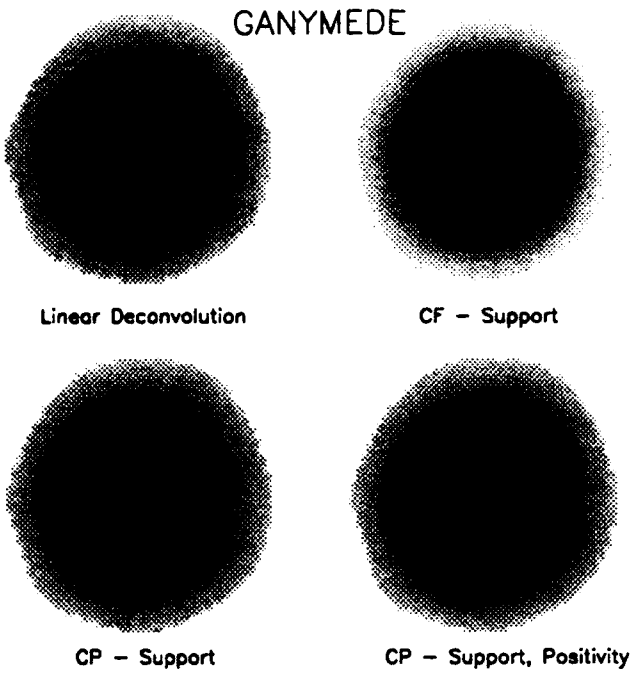

Figure 11. Image reconstructions of Ganymede: Linear deconvolution reconstruction, cost function reconstruction, and convex projections reconstructions with and without positivity.

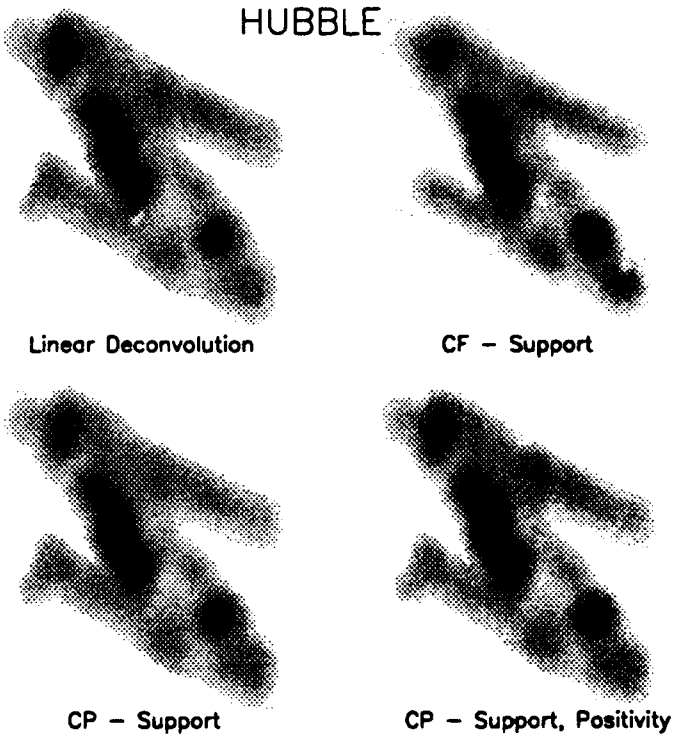

Figure 12. Image reconstructions of the Hubble space telescope: Linear deconvolution reconstruction, cost function reconstruction, and convex projections reconstructions with and without positivity.

The second field data image to be reduced is an image of the Hubble space telescope. The reconstructions are shown in Figure 12. As for Ganymede, both convex projections algorithms are very similar to the linear deconvolution image. The cost function reconstruction again shows energy being taken from the dim regions and moved towards the brighter regions. This is especially apparent on the solar panels. In addition, the brightly reflecting region on the upper solar panel where the support attaches the solar panel to the main body is diffused out in the cost function reconstruction. Since the size of the attachment is known to be smaller than the cost function reconstruction indicates, this shows more artifact generation.

5. Conclusions

Support constraints resulted in approximately 10% decreases in mean square error, on average, in the image domain for imagery collected on adaptive optically corrected telescopes for the two combinations considered here in the high light level situation for resolved images. For low light levels, on average no mean square error decreases were obtained. Since most astronomical and space objects will result in low light levels, this indicates that support constraints will provide only marginal improvement at best in adaptive optics data. A convex projections algorithm should be used to implement the support constraints if such constraints are applied since the cost function approach is more susceptible to artifact generation. This could be combated by excessively weighting the cost function for data points near the edge of the measured data region. However, the convex projections algorithm is quick and apparently not error-prone, so it appears to be the algorithm of choice for enforcing support constraints.

Acknowledgments

This research was funded by a grant from the U.S. Air Force Office of Scientific Research, Bolling Air Force Base, Washington, D.C. The authors wish to thank Marsha Fox and her field experiment team for providing the data used in the Ganymede and Hubble telescope reconstructions.

References

1. F. Roddier, "The effect of atmospheric turbulence in optical astronomy," in *Progess in Optics*, E. Wolf, ed. (North-Holland, Amsterdam, 1981), vol. 19.
2. J.W. Hardy, "Active optics: a new technology for the control of light," Proc. IEEE, vol. 66, pp.651-697 (1978)
3. M.C Roggemann, "Optical performance of fully and partially compensated adaptive optics systems using least-squares and minimum variance phase reconstructors," Computers Elect. Engng, vol.18, pp.451-466 (1992)
4. M.C. Roggemann, "Limited degree-of-freedom adaptive optics and image reconstruction," Applied Optics, vol.30, pp.4227-4233 (1991)
5. M.C. Roggemann, D.W. Tyler, and M.F. Bilmont, "Linear reconstruction of compensated images: theory and experimental results," Applied Optics, vol.31, pp.7429-7441 (1992)
6. G. Demoment, "Image reconstruction and restoration: overview of common estimation structures and problems," IEEE Trans.Acoust., Speech, Signal Processing, vol.37, pp.2024-2036 (1989)
7. M.I. Sezan and A.M. Tekalp, "Survey of recent developments in digital image restoration," Opt.Eng., vol.29, pp.393-404 (1990)
8. H. Stark, editor, *Image Recovery: Theory and Application*, Academic Press, Orlando, FL (1987)
9. C.K. Rushforth and R.L. Frost, "Comparison of some algorithms for reconstructing space-limited images," J.Opt.Soc.Am, vol.70, pp.1539-1544 (1980)
10. R.W. Schafer, et.al., "Constrained iterative restoration algorithms," Proc.IEEE, vol.69, pp.432-450 (1981)
11. C.K. Rushforth and R.W. Harris, "Restoration, resolution, and noise," J.Opt.Soc.Am, vol.58, pp.539-545 (1968)
12. D.L. Fried and D.T. Sherwood, "Final report on ONR contract No. N00014-88-C-0692: Phased array imaging," the Optical Sciences Company report no. DR-514 (1990)
13. C.L. Matson, "Fourier spectrum extrapolation and enhancement using support constraint," to appear in the IEEE Trans. Signal Proc., January 1994
14. C.L. Matson, "Variance reduction in Fourier spectra and their corresponding images with the use of support constraints," to appear in the J.Opt.Soc.Am.A., January 1994

15. M.C. Roggemann and C.L. Matson, "Power spectrum and Fourier phase spectrum estimation by using fully and partially compensating adaptive optics and bispectrum postprocessing," J.Opt.Soc.Am.A., vol.9, pp.1525-1535 (1992)
16. J.W. Goodman, *Statistical Optics*, Wiley, New York, (1985)
17. A. Papoulis; *Probability, Random Variables, and Stochastic Processes*, McGraw-Hill, New York (1965)
18. D.C. Youla, "Generalized image restoration by the method of alternating projections," IEEE Trans. Circuits Syst., vol. CAS-25, (1978)
19. D.C. Youla and H. Webb, "Image restoration by the method of convex projections: Part 1 - Theory," IEEE Trans. Medical Imaging, vol. M1-1, pp.81-94 (1982)
20. M.I. Sezan and H. Stark, "Image restoration by the method of convex projections: Part 2- Applications and numerical results," IEEE Trans. Medical Imaging, vol. M1-1, pp.95-101 (1982)
21. A. Lannes, S. Roques, and M.J. Casanove, "Stabilized reconstruction in signal and image processing I. Partial deconvolution and spectral extrapolation with limited field," J.Mod.Opt., vol.34, pp.161-226 (1987)